POLYTECHNIQUE MONTRÉAL
affiliée à l'Université de Montréal

Validation of a deterministic APOLLO3 scheme for accidental conditions on Sodium-cooled Fast Reactors

RAPHAËL GUASCH
Département de génie mécanique

Mémoire présenté en vue de l'obtention du diplôme de *Maîtrise ès sciences appliquées*
Génie nucléaire

Décembre 2023

POLYTECHNIQUE MONTRÉAL
affiliée à l'Université de Montréal

Ce mémoire intitulé :

Validation of a deterministic APOLLO3 scheme for accidental conditions on Sodium-cooled Fast Reactors

présenté par **Raphaël GUASCH**
en vue de l'obtention du diplôme de *Maîtrise ès sciences appliquées*
a été dûment accepté par le jury d'examen constitué de :

Cédric BÉGUIN, président
Alain HÉBERT, membre et directeur de recherche
Jean-François VIDAL, membre et codirecteur de recherche
Guy MARLEAU, membre
Richard CHAMBON, membre externe

DEDICATION

À ma soeur, Mathilde,
et mon frère, Gauthier

ACKNOWLEDGEMENTS

Je souhaite tout d'abord remercier le Professeur Alain Hébert pour son encadrement à Polytéchnique Montréal, pour sa disponibilité, ainsi que de m'avoir proposé de faire ce stage au CEA Cadarache. Je remercie chaudement Jean-François Vidal de m'avoir accueilli et encadré dans ce projet. Merci d'avoir été disponible pour répondre à mes questions, et d'avoir su me guider tout en me laissant des libertés pour mener ce projet "exploratoire". J'ai énormément apprécié travailler au LEPh et ce aussi grâce à toute l'équipe, je remercie Veronique qui a su m'accompagner et me mettre en confiance au laboratoire, à Giorgio pour le temps passé à m'aider et les discussions enrichissantes sur les modèles de fuites et sur le 2D1D. Merci à Laurent pour sa contribution à mes brefs travaux dans SNATCH, mais avant tout pour ses incontournables boutades et blagues en tout genre. Je souhaite aussi adresser un mot de remerciment à tous ceux qui ont su m'aider pour des questions pratiques de post traitement, Maciej et Dusan.

Merci aussi aux stagiaires et thésards du 230, j'ai passé six mois de stage mémorables grâce à vous. Je tiens à adresser une mention speciale à mes accolytes d'escalade, Dorian, Paul et Damien, avec qui j'ai passé d'innombrables heures au bloc.

Merci à mes amis de France comme de Montréal, et surtout à mes colocs successifs Milo, Ferdi, Florian, Marielle, Benoit et Thibault, qui ont toujours été là pour moi.

Finalement je tiens à remercier ma famille qui me soutient inconditionnellement depuis le début.

RÉSUMÉ

La connaissance précise du transport des neutrons dans le cœur d'un réacteur nucléaire est d'une importance cruciale. Celle-ci est nécessaire à la fois lors de l'exploitation industrielle des réacteurs mais aussi lors des phases de conception de ces derniers. Cette représentation est obtenue par le biais de simulations numériques modélisant les interactions entre la population de neutrons dans le cœur et les matériaux le constituant. Historiquement, différentes filières font intervenir des codes de calculs différents pour effectuer ces simulations. Par exemple, la filière industrielle des recteurs à eau pressurisée (REP) du parc français s'appuye sur les codes CEA APOLLO2/CRONOS2. En parallèle, les codes ECCO/ERANOS ont été développés afin de traiter les problématiques associées aux simulations de Réacteurs à Neutrons Rapides (RNR). Le développement de l'outil multi-filières APOLLO3 vient rompre cette logique en proposant un code de calcul neutronique regroupant des outils adaptés au traitement des Réacteurs à eau légère (REL) conventionnels du parc français, ainsi qu'aux études menées sur les RNR. Ces derniers ayant historiquement reçu une attention particulière en France avec Rapsodie, Phénix et Super-Phénix, et plus récemment le projet ASTRID, la filière des RNR refroidis au sodium (RNR-Na), apparaît comme un candidat intéressant pour le futur du parc nucléaire français, s'inscrivant dans une optique de fermeture du cycle du combustible. Le développement et la validation de méthodes numériques robustes apparaissent donc nécessaires aux études concernant ces derniers. La modélisation des configurations accidentelles est d'une importance particulière dans la phase de conception de cœurs. Un type d'accident particulièrement complexe à traiter lors des modélisations neutroniques d'un cœur de RNR-Na est la perte de caloporteur sodium. La prise en compte des zones vides, les effets axiaux associés à l'effet de vidange, ainsi que l'hétérogénéité axiale du cœur introduites dans les concepts RNR-Na, représentent un nouveau défi pour la simulation du transport neutronique. L'étude menée dans le présent ouvrage vise à comparer les différentes méthodes implémentées dans APOLLO3, dans le but de définir et valider un schéma de calcul neutronique à deux étapes. Celui-ci doit permettre la modélisation précise de conditions accidentelles en RNR-Na. Les schémas de calcul étudiés se décomposent de la manière suivante, premièrement un calcul de flux sur une géométrie d'assemblage est effectuée. Ce dernier est réalisé sur un maillage énergétique fin. Cette première étape permet d'obtenir des sections efficaces homogénéisées en espace et condensées en énergie, characterisant les milieux étudiés. Ces sections efficaces peuvent ensuite être utilisées afin d'effectuer un calcul de cœur entier sur un maillage énergétique à 33 groupes. Le cœur simulé est l'"ANTOINID", inspiré des versions 1 et 2 du "cœur faible vidange" (CFV) du projet ASTRID. Une attention partic-

ulière est portée à l'influence des hypothèses émises lors du calcul d'assemblage en réseau infini. Lors des calculs d'assemblages en 2D, l'hypothèse d'homogénéisation radiale directe à l'échelle de l'assemblage est testée et différentes combinaisons de solveurs et modèles de fuites sont introduites. Une représentation 2D+1D est adaptée aux assemblages ANTOINID et sa capacité de représentation des effets axiaux est évaluée. Dernièrement, les hypothèses introduites par trois solveurs cœur, MINARET, NYMO et MINOS sont testées. Une analyse des bias associés à la discrétisation de la variable angulaire est effectuée. Les méthodes S_N et P_N étant implementées dans MINARET et NYMO rspectivement, et les approximations de diffusion et de transport simplifié (SP_N) étant disponibles dans MINOS. Les biais introduits sur l'effet de vidange sodium ainsi que sur les taux de fission sont analysés. Ces derniers sont obtenus par comparaison avec le code stochastique TRIPOLI-4, aussi développé au CEA, qui servira de référence tout au long de l'étude.

Cette dernière révèle que l'hypothèse d'homogénéisation radiale directe des sous-assemblages testée n'est valide que dans le contexte d'un calcul en réseau infini, sans modèle de fuites. De plus, il apparaît que l'utilisation d'un modèle de fuite B1 homogène ne permet pas de capturer l'intégralité des effets axiaux en configuration vidangée. Ceci est révélé par l'étude des schémas "SCRAP" et "MOC2DHom" dont les limitations vis-à-vis du calcul de l'éffet de vidange sont mises en évidence dans le Chapitre 3. Parallèlement, il semble que l'utilisation d'un modèle de fuites hétérogènes en tandem avec une condensation des sections efficaces par les moments angulaires du flux soit à privilégier. En effet, les résultats obtenus grâce au schéma "MOC2DHet" indiquent une nette amélioration lors du calcul de l'effet de vidange sodium, ces résultats sont présentés au Chapitre 4. Ce dernier point apparaît aussi dans le cadre du modèle "2D1D Hybride" également présenté au Chapitre 4. Malheureusement, les résultats obtenus par l'intermédiaire du schéma réseau "2D1D complet" ne sont pas satisfaisants et une analyse fine du code est en cours pour en determiner l'origine. La comparaison est ensuite portée aux solveurs coeur entiers. Les résultats obtenus grâce à MINARET et NYMO sont très similaires, revelant ainsi l'efficacité de la méthode P_N de NYMO permettant une réduction du temps de calcul et de l'occupation mémoire. Les méthodes SP_3 et de diffusion de MINOS montrent aussi des résultats impressionant, allant même jusqu'à être plus précises que les méthodes S_N et P_N pour l'évaluation de l'effet de vidange sodium.

ABSTRACT

Reliable neutron transport calculations are of crucial importance for various branches of nuclear engineering. Although design and accidental transient studies require different types of performances in terms of time and precision, the quantifying of biases associated with numerical simulations remains a key aspect of a neutronics code validation study. Historically, different codes were developed at CEA to treat the various reactor designs. For example, the APOLLO2/CRONOS2 codes are used for industrial applications to the french park of Pressurized Water Reactors (PWR). On the other hands, codes such as ECCO/ERANOS were developed at CEA with the aim of treating difficulties associated with the simulation of Sodium Fast Reactors (SFRs). The development of the multi-purpose code APOLLO3 aims at combining methods and solvers involved in simulating both traditional water reactors and so called "Generation 4" designs. With SFR designs benefiting from a particularly dense experimental feedback in France, with the likes of Rapsodie, Phénix or Super-Phénix, they appear as interesting candidates for the future of the french nuclear industry. Maintaining, developing and validating robust methods in APOLLO3 to simulate such cores appears as a necessity for the future development of SFRs. With respect to numerical simulations, some of the most challenging situations occur in the event of accidental conditions, specifically in the presence of voided coolant channels. It goes without saying that the accurate representation of a loss of coolant accident (LOCA) is of prime importance for safety studies on advanced designs. The effect of a LOCA, along with axial heterogeneity of fuel assemblies such as ASTRID CFV's, represent a challenge for neutron transport simulation. This study's aim is to compare various methods implemented in the APOLLO3 framework, in order to define and validate a neutronic calculation scheme suited for the study of accidental conditions in SFRs. The core used as reference is the "ANTOINID", a simplified and adapted version of ASTRID CFV versions 1 and 2. In order to guarantee more flexibility, the scheme must follow a two steps architecture. The first step is the *lattice* calculation performed at the assembly level on a fine energy mesh and with a precise spatial representation. This step assumes the fuel assemblies to be in an infinite lattice of self-repeating geometries. The second step is a *full core* calculation, performed on a coarse 33 groups energy mesh with assemblies homogenized in space. Analysis of full core calculation results allow for the testing of various hypotheses made at the lattice step. For two dimensional lattice calculations, the spatial homogeneity of fuel assemblies is tested and different neutron leakage models are tested. A 2D+1D approach is implemented to represent axial heterogeneity in the assemblies. This representation's capabilities at predicting axial streaming effects is assessed. For each lattice

scheme, hypotheses introduced by three full core solvers available in APOLLO3 are tested. MINARET and NYMO solvers are used for exact transport calculations, using S_N and P_N angular representations respectively. MINOS solver's performances are also tested, both in diffusion and simplified transport (SP_N) treatments. Biases introduced by the lattice scheme and core solver choice are analyzed through comparison with reference Monte-Carlo TRIPOLI-4 results. Particular attention is paid to the biases on reactivity induced by sodium voiding, as well as those associated with fission rates in fuel assemblies.

Results show that the fuel assemblies' radial homogeneity hypothesis is valid in an infinite lattice, when neutron leakage is not considered. However, this description does not give satisfying results at the full core step, as the homogeneous flux calculation only allows for the use of a B1 homogeneous leakage model. Indeed, the homogeneous leakage model appears unsuited to represent important axial effects associated with the voided configurations. This is highlighted by results presented in Chapter 3 which show the limitations of the "SCRAP" and "MOC2DHom" lattice schemes. It appears that a B-heterogeneous leakage model combined with assembly homogenization and energy condensation by the flux's angular moments would be more suited to describe the anisotropic leakage through voided channels. This can be concluded from the analysis of results obtained from the "MOC2DHet" scheme presented in Chapter 4. The hybrid version of the 2D+1D model, also presented in Chapter 4, confirms this observation and shows the benefits of the 2D1D formalism when representing axial reflectors. However, the Full 2D1D scheme does not show satisfying results at the full core step, as it fails to predict the sodium void effect on reactivity. Additional work would be required to understand the biases introduced by the full 2D1D representation. full core solvers are also compared. The exact transport solvers MINARET and NYMO display highly similar results in terms of effects on reactivity and fission rates. This shows the efficiency of the P_N method implemented in NYMO as it greatly reduces memory requirements and computational time for the same full core problem. Additionally, MINOS diffusion and SP_3 results give surprisingly good results when it comes to estimating the sodium void effect on reactivity, even outperforming MINARET and NYMO in terms of precision.

TABLE OF CONTENTS

LIST OF TABLES

LIST OF FIGURES

LIST OF SYMBOLS AND ACRONYMS

DER	*Département d'Etudes des Réacteurs*
SPRC	*Service de Physique des Réacteurs et du Cycle*
LEPh	*Laboratoire d'Etudes de Physique*
LMAG	*Laboratoire de Modélisation des Accidents Graves*
SFR	Sodium Fast Reactor
RNR-Na	*Réacteur à Neutrons Rapides, refroidi au sodium*
UOX	Uranium Oxide
MOX	Mixed Oxides
BTE	Boltzmann Transport Equation
MC	Monte Carlo
MOC	Method of Characteristics
CP	Collision Probability
T4	TRIPOLI-4®
AP3	APOLLO3®
LOCA	Loss of Coolant Accident
SCRAP	Sodium Cooled Reactors with APOLLO3
FEM	Finite Elements Method
CFV	*Coeur Faible Vidange*
MPO	Multi-Parameter Output
SFRAG	Sodium Fast Reactors : *Accidents Graves*
ASTRID	Advanced Sodium Technological Reactor for Industrial Demonstration
SEASON	SEvere Accidents SimulatiON
INCA	*Interface Neutronique de Conception Avancée*

LIST OF APPENDICES

CHAPTER 1 INTRODUCTION

1.1 Context of the present research

This work has been sponsored by CEA®, Cadarache. It was performed during a six months internship at LEPh (Laboratory of Physical Studies), under Jean-François Vidal's supervision. All results stemming from APOLLO3® and TRIPOLI-4® codes remain the property of CEA®.

1.1.1 Foreword about CEA®

CEA® is a french research organization specialized in energy engineering. Historically, CEA® has been particularly invested in research backing up the french nuclear energy industry. The work presented in this dissertation has been done in the *Département d'Etudes des Réacteurs* (DER), in the *Service de Physique des Réacteurs et du Cycle* (SPRC) at the *Laboratoire d'Etudes de Physique* (LEPh) at CEA Cadarache.

1.1.2 Elements of context : reactor physics

Reactor physics is the branch of nuclear engineering that focuses on developing the necessary mathematical and numerical methods needed to perform nuclear reactor simulations. A panel of tools are at the engineer's disposal in order to provide precise and reliable simulations, relevant to contexts ranging from reactors' conceptual design, to analysis of accidental transients [1]. As it often goes, the benefits of a more precise calculation comes with the drawback of longer computation times. Indeed, the time constraints associated with operating an industrial reactor are not compatible with *stochastic* codes and rely on the ability of *deterministic* ones to perform simulations at a required precision, within a specific time constraint. In both cases, the complexity lies in the numerical simulation of neutron transport in a nuclear reactor. The stochastic approach relies on the Monte Carlo integration method. Each neutron's history is simulated and probabilities of events are drawn from randomly generated numbers. The deterministic way focuses on discretizing and solving the Boltzmann Transport Equation for neutrons. Reactor physicists therefore rely on the process of numerical verification and validation (V&V) through the comparison of deterministic solutions with a reference stochastic solution. Optimization of deterministic computational schemes for specific reactor designs thus appears to be a crucial part in the process of simulating advanced reactor concepts. This work focuses on the open Sodium-cooled Fast Reactor

(SFR) "ANTOINID" design and more particularly in the simulation of its accidental conditions. Three of the main hypotheses associated with *deterministic* calculations are tested in a static, uncoupled approximation.

This approach is driven by the development of a new generation deterministic code at CEA, APOLLO3® (AP3). Its aim is to regroup the collection of numerical methods and solvers required to simulate both "traditional" water moderated reactors, as well as new generation reactors [2]. AP3 capabilities and performances will there be investigated in a V&V approach with Monte Carlo (MC) code TRIPOLI-4® (T4) [3] as a reference.

1.1.3 GEN IV: Sodium Fast Reactors

The concept of SFRs has been explored throughout the second half of the XX^{th} century with various experimental reactors built, as well as reactors that saw industrial success, such as the french *Phénix* and *Super-Phénix*. As opposed to water-moderated *thermal* reactors which control neutron balance by slowing them down, through collision in water, the so called *fast* reactors precisely aim at limiting the neutron slowing down effect. This constrains the choices of possible coolants since it needs to be a good thermal conductor but also have limited probabilities of interacting with neutrons. These constraints have historically lead to considering Liquid Metal Fast reactors as good candidates. Indeed, SFRs have been selected as one of the six technologies envisioned for the future generation of nuclear fission reactors by the Generation IV International Forum [4]. The use of sodium as a moderator is justified by its excellent thermal conductivity [5], its relatively high critical temperature [6] as well as its low neutron absorbing properties.

International interest for SFRs lies in the fact that they open the possibilities to operate in *breeder* or *burner* mode, depending on the fuel optimization strategy. Indeed, a reactor operator could choose to favor the reaction of transmutation of Uranium 238 into Plutonium 239 by placing fertile fuel around an active fissile core. This could have the effect of generating more Pu than what the reactor uses, hence the *breeder* denomination. On the other hand, if no fertile fuel is involved, a SFR could be operated in *burner* mode, in which more fissile isotopes are burnt than produced [7]. This is a direct consequence of the choice of a *fast* neutron spectrum, since Uranium as well as Plutonium isotopes' have a higher probability of fission when interacting with high energy neutrons than capturing them. This can be seen by directly comparing fission and absorption cross sections of heavy isotopes such as U238, Pu239 or Pu240 for neutron energies greater than 1 MeV.

1.2 Scope of the present research

This project takes part in LEPh's contribution to the SEASON [8] platform, developed at CEA's Laboratoire de Modélisation des Accidents Graves (LMAG) which makes use of the SIMMER code [9] for coupled calculations between neutronics, thermo-hydraulics and thermo-mechanics. SEASON's neutronics simulations are still performed using the ECCO module of ERANOS [10]. With the advent of the new generation code APOLLO3 and the end of developments and contribution to the ECCO module, incorporating AP3 capabilities in the SEASON platform seems to be a relevant option. The present research aims at providing a variety of options to treat neutronics calculations in the context of accidental conditions. In order to guarantee some flexibility in the approach, the calculation schemes considered are based on a two-step architecture. The first is the so-called "lattice" step, corresponding to a fine spatial and energy representation of the neutron transport problem at the *assembly* level. The second step is the *full core* calculation which involves a coarser representation in both space and energy to solve the neutron transport problem over the whole reactor domain. This two-step architecture would allow for the full core calculation to be performed in one of SEASON's full core solvers, from assembly microscopic cross sections provided by AP3 lattice calculations. This work's main objective is to validate a APOLLO3® scheme for the simulation of accidental conditions on the open "ANTOINID" core. The first objective is to assess performances of existing solutions, such as the "SCRAP" scheme developed by J.F. Vidal and M. Zajaczkowski for LEPh. A particular emphasis is made on the representation of voided configurations which could happen in the event of a loss of coolant accident (LOCA) [1]. The second objective is to test alternative lattice schemes aiming at a better representation of sodium voiding effects. The latter include exploratory approaches such as the 2D1D architecture [11] as well as AP3's heterogeneous leakage model [12]. The schemes presented are designed for a wide range of applications, and could potentially provide a reliable replacement for the ECCO module in the SEASON platform. Additionally, preliminary work done to develop an interface between the AP3 lattice stage and SEASON is also briefly presented. This work is done as part of CEA's SFRAG (Sodium Fast Reactors : *Accidents Graves*) project, aiming at developing the capabilities of representing and simulating accidental conditions in Sodium Fast Reactor cores.

1.3 Thesis outline

Chapter 2 covers the basics of reactor physics and introduces standard mathematical notation. A review of the commonly used deterministic methods for solving the neutron transport

equation is presented and quantities of interest are introduced. Chapter 3 introduces the reference TRIPOLI-4 model along with a first comparison with the SCRAP scheme. The scheme's performances are assessed on four core configurations representing hypothetical accidental conditions. An extension of the SCRAP scheme to the MOC integration strategy is introduced. In Chapter 4, three lattice schemes are proposed. These are more complex alternatives aiming at a better description of voided configurations, specifically anisotropic effects due to neutron leakage along voided channels. The three schemes performances are compared at the full core's scale using the MINARET solver [13]. The study of voided configurations is extended to full core calculations in P_N formalism through the newly developed NYMO solver [14]. Lastly, diffusion and simplified transport calculations are performed in the MINOS solver [15]. All five schemes performances are compared for the three full core solvers evoked. Final recommendations and ideas for future research are presented. It is also worth mentioning that some work done towards using AP3 cross sections in the SEASON architecture is presented in Appendix B.

CHAPTER 2 A REVIEW OF REACTOR PHYSICS

Reactor physics is the discipline that aims at simulating nuclear reactors. For a nuclear engineer, it is of prime importance to be able to simulate operating conditions with desired accuracy. This can be motivated by isotopic evolution calculations in the industrial sector, which would for example assist the reactor operators' decision to change a fuel assembly. It could also be important to be able to simulate various geometric configurations from a conceptual design point of view for example. These first examples would not typically require precise "reference" calculations. On the other hand, accidental or transient analysis will require a lot more precise calculation of the main quantities of interest. Due to the reactor problem's scale and heterogeneity, calculations are generally performed in two steps. The first one is called a lattice calculation, its aim is primarily to calculate the materials' coarse groups cross sections, given the specifics imposed by the assembly geometry. The second step is a full core calculation that simulates the neutron's transport in the core's geometry. This chapter's first aim is to define the mathematical and theoretical background needed to approach reactor simulations. Secondly, numerical methods used in the computational schemes studied for the ANTOINID core will be presented. Lastly, the specific quantities of interest in the study of accidental configurations of the ANTOINID will be defined.

2.1 The neutron transport equation

2.1.1 Definitions

Neutron interactions with materials in a reactor's core is the phenomenon a reactor physicist wants to simulate. At the heart of these interactions is the neutrons' transport, which can be described by the Boltzmann equation. The latter represents the neutron population balance in a control volume. Neutron population will be mathematically attached to a quantity called the neutron flux. The formalism presented follows Hébert's presentation in "*Applied Reactor Physics*" [1]. This approach is based on statistical mechanics, making use of a six-dimensional phase space, in which :

1. A neutron's position is defined by three degrees of freedom as $\mathbf{r} = x\mathbf{i} + y\mathbf{k} + z\mathbf{k}$,
2. A neutrons' velocity, defined by three additional degrees of freedom, the velocity module $V_n = ||\mathbf{V}_n||$, where $\mathbf{V_n} = d\mathbf{r}/dt$ and its direction $\mathbf{\Omega} = \frac{\mathbf{V}_n}{V_n}$ which then encompasses two angular degrees of freedom.

Time dependence is introduced using the variable t, allowing for population density and velocity to change in time.

The *neutron flux* is the quantity of interest for the resolution of the transport equation, it is defined as :

$$\phi(\mathbf{r}, V_n, \mathbf{\Omega}, t) = V_n n(\mathbf{r}, V_n, \mathbf{\Omega}, t) \tag{2.1}$$

where $n(\mathbf{r}, V_n, \mathbf{\Omega}, t)$ is the neutron population density.

Integrating over the solid angle gives the *integrated flux* :

$$\phi(\mathbf{r}, V_n, t) = \int_\Omega d^2\Omega \phi(\mathbf{r}, V_n, \mathbf{\Omega}, t). \tag{2.2}$$

The neutron population in a control volume evolves through :

1. Neutron leakage out of the control volume
2. Neutron scattering by nuclei present in the control volume
3. Neutron capture by nuclei
4. Neutron generation through fission events

each of the reactions contributing to scattering, capture and fission events have a certain associated probability of occurring. This probability is expressed through a microscopic cross section, denoted $\sigma_{x,i}(\mathbf{r}, V_n)$, with units of barns (b) ($1\text{b} = 10^{-24} cm^2$). In this notation, index x corresponds to the reaction and i to a specific nuclei in the medium. For a macroscopic material which would be a homogeneous mixture of nuclei, the macroscopic cross section for reaction x will be defined as $\Sigma_x = \sum_i N_i \sigma_{x,i}$, where N_i represents the number density of nuclei i.

2.1.2 Derivation of the Boltzmann Transport Equation (BTE) for neutrons

Defining control volume C, with boundary surface ∂C, one can write the number of neutrons in such a control volume as

$$\int_C d^3r\, n(\mathbf{r}, V_n, \mathbf{\Omega}, t) dV_n d^2\Omega. \tag{2.3}$$

The differential form of the BTE is obtained by considering the change of the neutron population in an infinitesimal time Δt. The change in neutron population during Δt in C will be :

$$A = \int_C d^3r [n(\mathbf{r}, V_n, \mathbf{\Omega}, t + \Delta t) - n(\mathbf{r}, V_n, \mathbf{\Omega}, t)] dV_n d^2\Omega. \tag{2.4}$$

The neutrons streaming out of C during Δt will be accounted for by an integral of the neutron current over ∂C, combining this with the divergence theorem in volume C will give :

$$B = \int_C d^3r \nabla \cdot \mathbf{\Omega}\phi(\mathbf{r}, V_n, \mathbf{\Omega}, t) dV_n d^2\Omega \Delta t. \tag{2.5}$$

The number of neutrons lost to collisions will be accounted for through the term :

$$C = \int_C d^3r \Sigma(\mathbf{r}, V_n)[V_n n(\mathbf{r}, V_n, \mathbf{\Omega}, t)] dV_n d^2\Omega \Delta t. \tag{2.6}$$

Lastly, the new neutrons created in the control volume during Δt can be expressed by introducing the source density $Q(\mathbf{r}, V_n, \mathbf{\Omega}, t)$:

$$D = \int_C d^3r Q(\mathbf{r}, V_n, \mathbf{\Omega}, t) dV_n d^2\Omega \Delta t. \tag{2.7}$$

By conservation of particle balance, the BTE can be written as

$$A = -B - C + D \tag{2.8}$$

discarding the integral over control volume C and taking the limit as $\Delta t \to 0$ allows to write the differential form of Boltzmann's equation for neutron transport as :

$$\frac{1}{V_n}\frac{\partial}{\partial t}\phi(\mathbf{r}, E, \mathbf{\Omega}, t) + \nabla \cdot \mathbf{\Omega}\phi(\mathbf{r}, E, \mathbf{\Omega}, t) + \Sigma(\mathbf{r}, E)\phi(\mathbf{r}, E, \mathbf{\Omega}, t) = Q(\mathbf{r}, E, \mathbf{\Omega}, t). \tag{2.9}$$

where $Q(\mathbf{r}, V_n, \mathbf{\Omega}, t)$ is the neutron source term and $\Sigma(\mathbf{r}, E)$ is the material's total macroscopic cross section. For convenience, the dependence on neutron velocity V_n has been replaced by a dependence on the kinetic energy variable $E = \frac{m_n V_n^2}{2}$. In this work, when solving for neutron flux in assembly or full core calculations, the steady state hypothesis will be made. This allows us to remove the BTE's time dependence and equation (2.9) then becomes :

$$\nabla \cdot \mathbf{\Omega}\phi(\mathbf{r}, E, \mathbf{\Omega}) + \Sigma(\mathbf{r}, E)\phi(\mathbf{r}, E, \mathbf{\Omega}) = Q(\mathbf{r}, E, \mathbf{\Omega}) \tag{2.10}$$

2.1.3 The characteristic form of the BTE

The BTE can be written in its characteristic form. The latter is obtained by integrating the *streaming operator* $\mathbf{\Omega} \cdot \nabla\phi$ over a characteristic, a straight line whose direction is given by the unit vector $\mathbf{\Omega}$. A parametric notation is introduced using variable s, corresponding to the distance travelled along a characteristic from a reference point $\mathbf{r}$. The streaming operator

can also be parameterized introducing the s dependence, giving the characteristic form of the BTE.

$$\frac{d}{ds}\phi(\mathbf{r}+s\mathbf{\Omega},E,\Omega)+\Sigma(\mathbf{r}+s\mathbf{\Omega},E)\phi(\mathbf{r}+s\mathbf{\Omega},E,\Omega)=Q(\mathbf{r}+s\mathbf{\Omega},E,\Omega) \tag{2.11}$$

2.1.4 The integral form of the BTE

In other resolution techniques, such as the collision probability method (CP), the BTE is written in its integral form. This formulation is obtained by integrating the angular flux (2.1) along a characteristic. An integrating factor $e^{-\tau(s,V_n)}$ is introduced, expressed in terms of the optical path τ, defined as :

$$\tau(s,V_n)=\int_0^s ds'\Sigma(\mathbf{r}-s'\mathbf{\Omega}',V_n). \tag{2.12}$$

Using this integrating factor and re-writing equation (2.11) leads to the integral form of the transport equation expressed as :

$$\phi(\mathbf{r},E,\mathbf{\Omega})=\int_0^\infty ds\, e^{-\tau(s,V_n)}Q(\mathbf{r}-s\mathbf{\Omega},E,\mathbf{\Omega}) \tag{2.13}$$

This form of the BTE corresponds to the expression of the problem on an infinite domain. In the case where the integration domain is finite, one would have to integrate from 0 to the maximal value for s.

Equation 2.13 can be interpreted as the fact that a particle emitted from source Q, will travel with direction $\mathbf{\Omega}$ in a media with total macroscopic cross section Σ. Its contribution to the flux at a certain point away from the source will thus be exponentially attenuated due to its optical path τ (eq. (2.12)) through the medium.

2.1.5 Boundary Conditions

When modelling real configurations, the domain D in which the neutrons travel can be bounded by a surface ∂D. This section looks at different conditions that can be imposed on boundary ∂D depending on the model's needs. An outward normal vector $\mathbf{N}(\mathbf{r}_s)$ is defined $\forall \mathbf{r}_s \in \partial D$. Numerical solutions to the BTE will be interested in the angular flux, as defined by equation (2.1), in V, so for $\mathbf{\Omega}\cdot\mathbf{N}(\mathbf{r}_s)<0$.

An *albedo* boundary condition is written as :

$$\phi(\mathbf{r}_s,V_n,\mathbf{\Omega},t)=\beta\phi(\mathbf{r}_s,V_n,\mathbf{\Omega}',t),\forall\mathbf{\Omega}\cdot\mathbf{N}(\mathbf{r}_s)<0 \tag{2.14}$$

this type of boundary condition relates the incoming flux with a known outgoing flux, where $\mathbf{\Omega}'$ is the outgoing particle's direction. For a *vacuum* boundary condition, the albedo β is set to 0. For a *reflective* boundary condition, $\beta = 1$.
A *specular* reflection condition is imposed as :

$$\mathbf{\Omega} \cdot \mathbf{N}(\mathbf{r}_s) = -\mathbf{\Omega}' \cdot \mathbf{N}(\mathbf{r}_s) \tag{2.15}$$

where $(\mathbf{\Omega} \times \mathbf{\Omega}') \cdot \mathbf{N}(\mathbf{r}_s) = 0$.

Additional boundary conditions such as the *white* and *periodic* conditions are defined in Hebert's book [1] but will not be used in this text.

2.1.6 Steady-State Source density

When the quantities involved in the BTE do not vary significantly in time, the steady-state hypothesis is valid. The fission reactions are assumed to be *isotropic* in the LAB frame. This allows to express the neutron source term Q from equation 2.10, as a sum of two terms.

$$\begin{aligned} Q(\mathbf{r}, E, \mathbf{\Omega}) = \int_{4\pi} d^2\Omega' \int_0^\infty dE' \Sigma_s(\mathbf{r}, E \leftarrow E', \mathbf{\Omega} \leftarrow \mathbf{\Omega}') \phi(\mathbf{r}, E', \mathbf{\Omega}') \\ + \frac{1}{4\pi K_{eff}} Q^{fiss}(\mathbf{r}, E) \end{aligned} \tag{2.16}$$

The first integral term corresponds to the neutron sources contributing from the diffusion and (n,xn) reaction. Σ_s is the total macroscopic scattering differential cross section, grouping diffusion and (n,xn) reactions.

The second term corresponds to the neutrons originating from fission sources. The $Q^{fiss}(\mathbf{r}, E)$ factor amounts for the isotropic fission sources and can be explicitly written as shown in equation 2.17. In this formulation, J_{fiss} is the total number of fissionable isotopes, χ_j is the *fission spectrum* for isotope j. It is a probability density, normalized to 1. Moreover, ν represents the average number of neutrons emitted per fission event. Lastly, $\Sigma_{f,j}$ is the macroscopic fission cross section for isotope j.

$$Q^{fiss}(\mathbf{r}, E) = \sum_{j=1}^{J^{fiss}} \chi_j(E) \int_0^\infty dE' \nu \Sigma_{f,j}(\mathbf{r}, E') \phi(\mathbf{r}, E') \tag{2.17}$$

The K_{eff} factor is the *effective multiplication factor*, it is an artificial factor, introduced in order to maintain the steady-state condition. It plays a crucial role in analyzing a configu-

ration's *criticality*, defined as $\rho = \frac{K_{eff}-1}{K_{eff}}$. For $K_{eff} > 1$, $\rho > 0$, a configuration is said to be over-critical, meaning that the neutron production terms dominate and neutron population increases exponentially. For $K_{eff} < 1$, $\rho < 0$, a configuration is said to be sub-critical, implying that the neutron absorption terms dominate so that the neutron population will decrease.

It will therefore be important to aim for $K_{eff} \to 1$ so that an optimal critical state is reached at the full core scale. In real life applications, this can be achieved by operating the control mechanisms such as control rods or boron concentration for example.

2.1.7 The Multi-group Formalism

When solving the BTE, the energy variable is treated by discretizing the continuous neutron energy domain in a set of G groups. Within these groups, neutrons are considered as one-speed particles and all energy dependent quantities are condensed into these groups. Generally, the lethargy variable $u = \ln(\frac{E_0}{E})$ is introduced, where E_0 is a reference energy. It is generally taken to be the maximal energy of fission produced neutrons ($10MeV$ or $20MeV$ depending on the cross section library used) , however the convention of $E_0 = 10MeV$ has been kept in the APOLLO3 code.

Groups can then be represented as

$$W_g = \{E; E_g \leq E \leq E_{g-1}\} = \{u; u_{g-1} \leq u < u_g\}; g = 1, G \tag{2.18}$$

One can then write the multi-group steady-state BTE for a group g as :

$$\mathbf{\Omega} \cdot \nabla \phi_g(\mathbf{r}, \mathbf{\Omega}) + \Sigma_g(\mathbf{r}) \phi_g(\mathbf{r}, \mathbf{\Omega}) = Q_g(\mathbf{r}, \mathbf{\Omega}) \tag{2.19}$$

where the multi-group source density as given by equation 2.16 takes into account neutrons from a group h coming into group g, as contributions to the group's source density. In a similar way, the fission sources are treated through the averaging of the fission spectrum over group g.

2.2 Solving the BTE

2.2.1 The Collision Probability method (CP)

The Collision Probability method (CP) makes use of the BTE's integral formulation. Spatially discretizing equation 2.13's multi-group formulation and hypothesizing all particle

sources to be isotropic leads to the CP formulation. The domain of integration of equation 2.13 is partitioned into a set of regions V_i.

The CP formulation is written as such :

$$V_j \Sigma_{j,g} \phi_{j,g} = \sum_i Q_{i,g} V_i P_{ij,g} \tag{2.20}$$

where :

1. $\phi_{j,g}$ is the average integrated flux in region j for group g
2. $\Sigma_{j,g}$ is the average macroscopic cross section of region j for group g, weighted by the integrated flux.
3. $P_{ij,g}$ is the probability for a neutron born in group g and in any region V_i, to undergo its first collision in region V_j.

Reduced CPs are introduced as $p_{ij,g} = \frac{P_{ij,g}}{\Sigma_{j,g}}$, which insures correct numerical behavior in the case where V_j is a voided region as both Σ_j and P_{ij} will tend to zero.

The *reciprocity* and *conservation* properties are used to solve for the reduced CPs through numerical integration. This is done through a *tracking* of the domain, allowing for the computation of neutron optical paths along a sufficiently large number of trajectories. Once the CPs are known, the source term $Q_{j,g}$ is computed and the integrated flux in all regions V_i can be solved for using the following equation :

$$\phi_{i,g} = \sum_j Q_{j,g} p_{ij,g}. \tag{2.21}$$

In this work, the CP method is used as part of Tone's method for self-shielding, which will be introduced later.

2.2.2 The Method of Characteristics

The Method Of Characteristics (MOC) makes use of the backward characteristic form of the BTE as shown in equation 2.11. It is generally considered as one of the most precise methods for computing neutron flux and its capabilities can be extended to unstructured 2D or 3D geometries [16]. Due to its capabilities of providing a precise description, it comes at a great computational cost. In order to optimize the method with respect to computational time, it is subject to ongoing research focusing on acceleration techniques. In this work it is

used at the lattice stage of the calculation, for 2D flux calculations on unstructured assembly geometries. The following aims at presenting the necessary mathematical background to understand the MOC technique. The integration domain is partitioned in V_i regions and a *tracking* is produced similarly as in the CP method. The MOC integration strategy is based on the discretization of equation 2.11 along each particle path in the domain's tracking. For a region V_i, it takes into account contributions to the flux from all paths in the tracking domain. By introducing the assumption that $\phi(\mathbf{r}, E, \mathbf{\Omega}) \approx \phi_g(\mathbf{r}, \mathbf{\Omega})$, the multi-group is applied and the subscript g will be implied in the rest of this paragraph in an effort to clarify the notation.

Mathematically the MOC integration strategy can be expressed as :

$$V_i\phi_i = \int_{V_i} d^3r \int_{4\pi} d^2\Omega\phi(\mathbf{r}, \mathbf{\Omega}) = \int_{\Gamma} d^4T \int_{-\infty}^{\infty} ds\chi_{v_i}(\mathbf{T}, s)\phi(\mathbf{p} + s\,\mathbf{\Omega}, \mathbf{\Omega}) \tag{2.22}$$

where, $\Gamma = \{\mathbf{T}\}$ represents the tracking domain, ie the collection of single characteristics $\mathbf{T}$, defined by their orientation $\mathbf{\Omega}$ and starting point $\mathbf{p}$. Starting points are selected on a *reference* plane $\mathbf{\Pi_\Omega}$, perpendicular to $\mathbf{T}$. $\chi_{v_i}(\mathbf{T}, s)$ is a characteristic function equal to 1 if the current point $\mathbf{p} + s\mathbf{\Omega}$ is inside region V_i and zero otherwise. It must be noted that the flux given in equation 2.22 is a *scalar* flux that has been integrated over the whole domain, with respect to both the angular and spatial variables. Due to the anisotropic nature of the neutron flux studied in this work, the angular dependence must be kept into consideration. For this reason, one must solve for the angular flux. A detailed description of the procedure used in the TDT code included in APOLLO3 can be found in Santandrea et al. [16]. In order to keep this discussion concise, elements of notation from R. Le Tellier's thesis [17] are introduced :

Considering a tracking Γ, with a characteristic going through K regions. The lengths of each *chord*, $L_k(\mathbf{T})$, along with the index $N_k(\mathbf{T})$ of the corresponding region are computed and stored. These form a set of pairs $(N_k, L_k)_{k\in[1,K]}$. Thanks to these parameters it is possible to express the points where the characteristic intersects with interfaces between regions, as well as the *angular* flux at these intersection points. This can be written as :

$$\begin{aligned} &\mathbf{r}_{k+1} = \mathbf{r}_k + L_k\mathbf{\Omega} \\ &\phi_k(\mathbf{T}) = \phi(\mathbf{r}_k, \mathbf{\Omega}), k \in [1, K] \end{aligned} \tag{2.23}$$

it can be noted that for a *cyclic* tracking, as used in this work, the relation $\mathbf{r}_1 = \mathbf{r}_{K+1}$ must be obeyed.

In the MOC, the average *moments* of the angular flux are computed in each region i. This is done by projecting the angular flux on the spherical harmonics basis, whose Ferrer definition

can be found in Hébert's book [1]. This allows Le Tellier to write an equation similar to 2.22, expressing the angular flux moments :

$$V_i \Phi_{l,i}^m = \int_{V_i} d^3r \int_{4\pi} d^2\Omega \, R_l^m(\mathbf{\Omega}) \phi(\mathbf{r}, \mathbf{\Omega}) \tag{2.24}$$

using the MOC formalism to treat integration over the tracking of the domain, equation 2.24 can be re-written as :

$$V_i \Phi_{l,i}^m = \int_{\Gamma} d^4T \sum_{k=1}^{K} \delta_{i,N_k} L_k(\mathbf{T}) \bar{\phi}_k(\mathbf{T}) R_l^m(\mathbf{\Omega}), \tag{2.25}$$

where δ_{k,N_k} is the Kroneker delta, ensuring the fact that only contributions of chords in region i are considered.

The notation in equation 2.23 allows to write the definition of the average angular flux on a chord as :

$$L_k \bar{\phi}_k(\mathbf{T}) = \int_0^{L_k} ds \, \phi(\mathbf{r}_k + s\mathbf{\Omega}, \mathbf{\Omega}). \tag{2.26}$$

This allows to solve the backward characteristic form of the BTE restricted to the tracking. Integrating equation 2.11 over $s \in [0, L_k]$, the transmission equation is obtained :

$$\phi_{k+1}(\mathbf{T}) - \phi_k(\mathbf{T}) + \Sigma_{t,N_k} L_k \bar{\phi}_k(\mathbf{T}) = L_k \bar{Q}_k(\mathbf{T}), \tag{2.27}$$

where $\bar{Q}_k(\mathbf{T})$ is the average source over the k^{th} chord. Estimating this average requires an assumption about the spatial dependence of the source. The most commonly used approximation is the "flat source approximation" $\forall s \in [0, L_k], Q_k(\mathbf{r}_k + s\mathbf{\Omega}, \Omega) = Q_{N_k}(\mathbf{\Omega})$ leading to the Step-Characteristic (SC) integration scheme for MOC. The flat source approximation leads to considering constant angular fluxes in each region. The SC approach is kept in this work since all MOC calculations are performed on two-dimensional geometries. Furthermore, it is worth mentioning that higher-order MOC approaches are available in TDT. The latter rely on expanding the source term and angular fluxes using a higher order polynomial representations to treat their spatial dependence. This approach is used by Santandrea et al. in their 3D MOC in order to treat the axial variations on the flux [16].

2.2.3 The discrete ordinates (S_n) method

The discrete ordinates method abbreviated S_n method, is a discretization technique used to solve the BTE. It is based on the differential form of the transport equation 2.9, for which the angular flux is discretized for specific angular values [1]. This leads to solving for the

particle flux for each discrete angle.

$$\mathbf{\Omega}_n \cdot \nabla\phi(\mathbf{r}, \mathbf{\Omega}_n) + \Sigma(\mathbf{r})\phi(\mathbf{r}, \mathbf{\Omega}_n) = Q(\mathbf{r}, \mathbf{\Omega}_n), n = 1, ..., N \tag{2.28}$$

This approach is based on an angular quadrature set $\{\mathbf{\Omega}_n,\ W_n,\ \text{n=1,N}\}$, where W_n is the weight associated to each direction.

MINARET In the formalism used in MINARET, the one speed transport equation is solved in each group, for each specific angle. The multi-group nature of the problem is taken into account by considering the scattering cross sections' standard expansion on Legendre polynomials [13], in the source term for the one speed equation 2.28. The angular quadrature set is used to compute the source term $Q(\mathbf{r}, \mathbf{\Omega}_n)$ in 2.28. More particularly, it is used when treating the angular dependence from the diffusion source, shown in equation 2.16.

Typical angular quadrature sets such as *level-symmetric* and *product* quadratures are available in MINARET [13]. In this work, the 3D core calculations performed using MINARET make use of an hexagonal product quadrature. According to R. Le Tellier et. al. in [18], standard level symmetric S_N quadratures are not sufficient to properly calculate local effects on neutron transport, such as the effects of the voiding of coolant zones in fuel assemblies.

IDT The S_N method in one dimension is also used in SCRAP lattice calculations on a homogenized plane geometry through APOLLO3's IDT solver (see Chapter 3).

SNATCH Lastly, the S_N method also comes into play in the SNATCH transport solver in which an hexagonal product quadrature is also used [18]. Preliminary results are presented in Appendix B.

MOC Angular treatment used in the MOC integration technique is also an S_N based method [19] [16], allowing for integration of the angular variable :

$$\oint \frac{d\mathbf{\Omega}}{4\pi}[*], \tag{2.29}$$

to be approximated by a discrete sum over a finite number (N) of directions $\mathbf{\Omega}_k$:

$$\sum_{k=0}^{N} w(\mathbf{\Omega}_k)[*], \tag{2.30}$$

where the weights w_k are obtained using an appropriate quadrature formula. In this work, these weights are obtained through a cyclic Gauss-Tchebytchev product quadrature adapted to hexagonal geometries.

2.2.4 The P_N method

The P_N method is based on the differential form of the BTE (eq. (2.9)) in which the angular treatment relies on an expansion on the real spherical harmonics basis. More precisely, the angular flux and source density are expressed by a truncated spherical harmonic expansion, in this work to order $N = 3$. For the angular flux, this expansion can be written as :

$$\phi(\mathbf{r}, \mathbf{\Omega}) = \sum_{l=0}^{N=3} \frac{2l+1}{4\pi} \sum_{m=-l}^{m=l} \phi_l^m(\mathbf{r}) R_l^m(\mathbf{\Omega}) \tag{2.31}$$

where ϕ_l^m's are the angular flux's moments, which carry the spatial dependence. R_l^m are the real spherical harmonics defined through the Ferrer definition of Legendre polynomials, as presented in Chapter 2 of Hébert's book [1].

2.2.5 The Simplified P_N (SP_N) method

In the 1960's, E.M. Gelabrd [20] introduced the SP_N method based on the the expansion of the angular flux on an incomplete development at order 2N+1, where only one moment is kept for even orders, and three for odd orders. This of course introduces biases in the numerical result since the angular fluxes do not converge to the exact solution when N is increasing. On the other hand, the SP_N method produces a linear system of equation involving less coupling and a simplified structure, compared to its P_N counterpart.

In this work, the performances of solver MINOS [15] are studied applying the SP_3 formalism to the "ANTOINID" full core calculations. The SP_N equations will be presented in a subsequent section when treating the Finite Elements Method (FEM) solution to the SP_N full core problem.

2.3 Resonance self-shielding

Resonance self-shielding is a phenomenon affecting absorption reaction rates, its primary causes are the resonant absorption reactions as well as spatial "neutron shielding" effects. As microscopic cross sections heavily depend on energy, this means that neutrons with energy close to a resonance are more likely to interact with a given nucleus. This has the impact

of reducing neutron flux in the energy domain where resonances are present. On the other hand, spatial self-shielding effects are generally felt at the interface between coolant and fuel regions. Considering a neutron traveling in the coolant, it will have a higher probability of being absorbed in the outer radial region of the fuel rod, causing a decrease in neutron flux in the fuel rod's inner radial regions, thus decreasing its associated reaction rate. It must be noted that this type of radial discretization of the fuel rods is only necessary when dealing with assembly calculations for water moderated designs. In SFRs, the coolants slowing down effect are less important which leads neutrons to have an average greater energy and optical path. This means that rim effects on fuel rods can be neglected and that for a given fuel assembly, only outermost fuel rods and outer coolant has to be treated separately. This will be described in more details in Chapter 3.

The energy and spatial self-shielding effects are accounted for by the self-shielding step in lattice calculations. Depending on the neutron slowing down energy range, different methods are available in APOLLO3®. In fast reactor applications, the subgroup [21] method and more particularly the Tone [22] method are the most commonly used.

In their paper [23], Vidal and Raynaud show that Tone's method can completely replace the method of subgroups for energies greater than 3 keV, in more demanding Light Water Reactor calculations. The ANTOINID core's fast spectrum justifies using Tone's method, thus allowing for a consequent Central Processing Unit (CPU) time reduction [23], [24].

Tone's method In Tone's method, the first assumption is that the neutron source is uniform in each group g. The second more fundamental assumption is that the flux in the j^{th} region due to neutrons emitted from the i^{th} region $\phi_{ij}(u)$ is proportional to the energy discrete flux ϕ^g_{ij}. The proportionality coefficient $\alpha_j(u)$ is assumed to depend only on the arrival region j [1] [23]. It must be noted that the variable u represents the *lethargy* as defined earlier in subsection 2.1.7. Using the CP formalism presented earlier (Eqs. 2.20, 2.21), this is written mathematically :

$$\phi_{ij}(u) \approx \alpha_j(u) \frac{V_i}{V_j} \frac{P^g_{ij}}{\Sigma^g_{t,j}} Q^g_i = \alpha_j(u) \phi^g_{ij} \tag{2.32}$$

The implementation of Tone's method in APOLLO3® is based on the utilization of mathematical probability tables in order to calculate effective cross-sections. It makes the approximation of a narrow resonance model as the slowing-down source [24]. Using Tone's method greatly reduces the CPU time as it considers group CP matrices [24] without needing a finer discretization of the fuel rods. This saves the computation of the CP matrices for each base

point in the group's probability table [23] as it is done in the subgroup method.

2.4 Homogenization and Condensation

In two steps schemes such as the ones presented in this work, the homogenization/condensation step is crucial. Indeed, the aim of performing reactor calculations in two steps is to be able to first treat lattice calculations on a refined spatial and energy mesh, for a reduced geometry. At the second step, the geometry is representative of the full core, but the energy mesh is coarser as well as the geometric description of each assembly. The process of computing equivalent cross sections for a homogenized assembly geometry from the ones on the exact spatial representation will be referred to as *homogenization*. Similarly, the process of switching from the fine energy representation (several hundreds of groups), to the coarser 33 groups used in SFR's full core calculations is called *condensation*.

One of the traditional approaches is the *superhomogenisation* (SPH) technique presented by Kavenoky [25] and greatly developed by Hébert [26], is based on equivalence principles. It imposes the conservation of the reaction rates obtained from the reference lattice calculation. According to Jacquet [27] the SPH technique does not provide satisfying results for realistic SFR cores involving steel reflectors. Indeed, it appears that the SPH technique does not take angular effects on total and transfer cross sections into account. For this reason, Vidal suggests the angular flux-moments weighting technique [28] for calculating condensed/fully homogenized cross sections to be used in full core calculations. In order to do so, the flux-moments technique does not impose the strict conservation of reaction rates but focuses on preserving the angular dependencies of calculated cross sections. In practice, this is done by modifying the transfer cross sections. The technique has been shown to be efficient in SFR calculations in [29] and more recently in [28].

It is worth noting that in this work, condensation is performed from a 1760 (or 383) groups fine energy mesh used at the lattice stage to a 33 groups mesh used for solving the problem on the full core geometry. The 33 groups mesh used is a modified version of the "historical" 33 groups mesh used in ECCO/ERANOS. Some of its energy bounds have been modified in order to be compatible with the finer 383 and 1760 groups energy meshes used in lattice calculations. Spatial homogenization is performed from the exact assembly geometry to the equivalent completely homogenized region.

Results obtained using the flux-volume weighting technique will be presented in Chapter 3. On the other hand, those from the flux-moments method will be introduced in subsections 4.2.1 and 4.2.3. The impact of *leakage models* combined to these homogeniza-

tion/condensation techniques will also be studied.

2.5 Neutron Leakage Models

It would be possible to treat the full core geometry in a single calculation step (with the MOC 3D capabilities of APOLLO3 for example) but this would come to a tremendous cost in CPU time. For this reason, the approach considered in this work is to perform an initial flux calculation assuming an infinite lattice of assemblies. However, this representation does not provide a satisfying description of neutron leakage effects in a realistic, finite domain. To correctly represent the assembly in a realistic environment, leakage models are required in order to take into account neutrons leaving the assembly, thus impacting the energy spectrum and potentially acting as a source term for neighboring assemblies in the core. In the next subsections, the B1 homogeneous and B heterogeneous models are briefly presented, as well as their hypotheses and approximations.

2.5.1 The fundamental mode

The *fundamental mode* is assumed and applied to the infinite lattice of assemblies with specular boundary conditions. The neutron flux is assumed to be the product of a *macroscopic* distribution in space $\psi(\mathbf{r})$ with a *fundamental flux* denoted $\varphi(\mathbf{r}, E, \mathbf{\Omega})$, so that :

$$\phi(\mathbf{r}, E, \mathbf{\Omega}) = \psi(\mathbf{r})\varphi(\mathbf{r}, E, \mathbf{\Omega}) \tag{2.33}$$

Moreover, the macroscopic flux distribution is assumed to be periodic and solution to the *Laplace equation* :

$$\nabla^2\psi(\mathbf{r}) + B^2\psi(\mathbf{r}) = 0 \tag{2.34}$$

where B^2 is the *buckling* used to adjust the distribution's curvature.

Choosing vector $\mathbf{B}$ such that $B^2 = \mathbf{B} \cdot \mathbf{B}$, it is then possible to factor the neutron flux as :

$$\phi(\mathbf{r}, E, \mathbf{\Omega}) = \varphi(\mathbf{r}, E, \mathbf{\Omega})e^{i\mathbf{B}\cdot\mathbf{r}} \tag{2.35}$$

2.5.2 The B1 Homogeneous Model

The B1 Homogeneous Model is based on the assumption that the neutron leakage out of the assembly geometry can be properly described by a homogeneous equivalent geometry. This

implies that the periodic fundamental flux from equation 2.35 becomes independent of the spatial variable, thus becoming :

$$\phi(\mathbf{r}, E, \mathbf{\Omega}) = \varphi(E, \mathbf{\Omega}) e^{i\mathbf{B}\cdot\mathbf{r}} \tag{2.36}$$

This assumption is introduced in the transport equation which is weighted and integrated as required by the B1 model in order to get a set of two coupled equations that form the B1 equations. A detailed derivation can be found in A. Hébert's book [1].

2.5.3 The B-Heterogeneous Model

The limitations of the homogeneous B1 leakage model are reached in the case of loss of coolant accidents (LOCA) studied in this work. In these types of problems, the heterogeneous and axial streaming effects through voided channels are not represented by the homogeneous model. The B heterogeneous model also assumes the existence of the *fundamental mode* but makes no assumption about the spatial dependence of the fundamental flux in equation 2.35.

J. Tommasi shows in his paper [12] that the assembly geometry's central symmetry is a sufficient condition to guarantee the eigenvalue K_{eff} to be real. This model is thus applicable to the ANTOINID's assembly calculations since their hexagonal properties guarantee a $\pi/6$ symmetry which translates to a rotational invariance of the problem about the assembly's center. This symmetry also implies that the real part of the complex flux should be symmetric with respect to rotations about the center. On the other hand, the complex part of the flux will be anti-symmetric with respect to such rotations. These properties are used extensively in the Flux-Moments homogenization/condensation method [28].

2.6 Lattice calculation schemes

This section aims at presenting the existing lattice schemes prior to this work. They allow for the treatment of SFR assembly calculations. Chapters 3 deals with evaluating the performances of SCRAP and its extended version, later referred to as "MOC2DHom". Chapter 4 presents results from more "advanced" schemes, two of which are based on the 2D1D architecture.

2.6.1 "SCRAP-based" lattice schemes

The SCRAP scheme was developed and validated by Jean-François Vidal and Maciej Zajaczkowski on the the 3600 MW variant of the Japanese Sodium Fast Reactor (JSFR) [30].

SCRAP's aim is to be a robust and efficient candidate for design studies of SFR assembly calculations. Its specifics and choices of parameters were accessed from confidential internal notes. The SCRAP lattice scheme makes use of a 383 groups energy mesh and consists of five keys steps. First, Tone's method [22] [24] is used to perform the self-shielding on the exact two dimensional fissile sub-assembly geometry. Then, the 2D geometry is homogenized to a single media, through the Flux-Volume homogenization technique [31]. This allows for a quick S_N one dimensional flux calculation on the homogenized geometry, performed through AP3's Integro-Differential Transport (IDT) solver [2] [32]. This initial flux calculation is performed in the context of an infinite lattice of fissile sub-assemblies. A B1 homogeneous leakage model is then applied and the leakage term is in turn used as a source for sub-critical assembly calculations. The obtained cross sections are condensed to a 33 groups energy mesh and kept to a single homogenized medium (one per sub-assembly type). This last condensation step is performed using the Flux-Volume method once again.

It is worth noting that before starting this project, the python script defining the SCRAP scheme was provided by Vidal. The "MOC2DHom" and "MOC2DHet" schemes were extended from SCRAP by replacing the initial flux calculation by a call to the TDT solver [2]. This allows to perform a MOC integration step on the exact 2D unstructured geometry. The choice of tracking parameters for the TDT solver is taken according to those recommended by P. Archier et. al. in [21]. The MOC2DHet scheme was also extended to make use of APOLLO3's B1 heterogeneous leakage model [12] [33]. The latter also makes use of the Flux-Moments homogenization/condensation technique whose efficiency was shown by Vidal et. al. in [28]. These amendments to the original SCRAP architecture were done to support the present work, thanks to the help of JF. Vidal.

2.6.2 2D1D schemes

The 2D1D approach is based on the MOC integration technique. It was originally developed by B. Faure as part of his thesis [11] in order to treat the axially heterogeneous ASTRID core [34]. The 2D1D formalism is based on the assumption that a three dimensional assembly geometry can be taken to be equivalent to a collection of 2D slices representing each media. The 2D1D solver thus performs a coupled calculation between 2D unstructured representations of each slice, treated by the TDT solver, and a 1D column calculation. The latter is performed thanks to the homogenization of each axial slice, allowing to create an equivalent 1D geometry. An illustration of this principle can be seen in figure 2.1 taken from B. Faure's work [11].

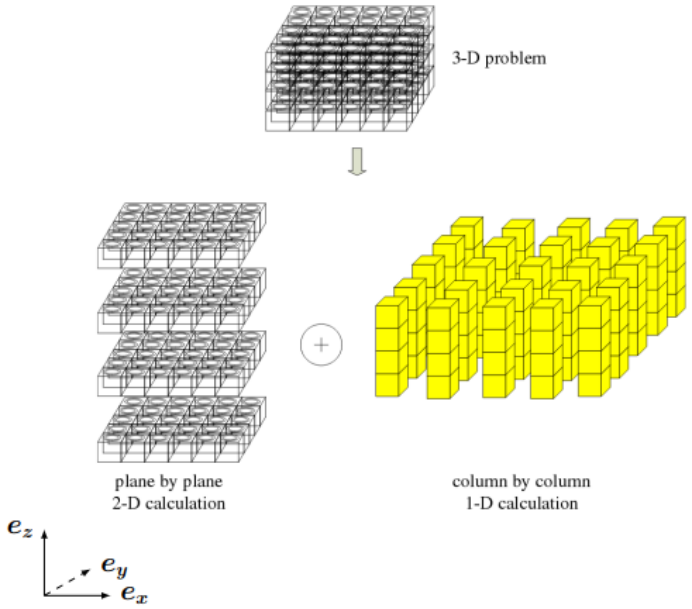

Figure 2.1 Example of 2D1D discretization of a 3D problem.

The full 2D1D scheme In the first iteration, flat fluxes are initialized on each of the 2D geometries. Obtained cross sections are homogenized to the corresponding 1D axial geometry, using the Flux-Moments method. The IDT solver is called to perform a flux calculation on the homogeneous slices composing a column (or assembly). Leakage out of each slice is computed as the difference between fluxes at the z_{min} and z_{max} interfaces. The leakage terms obtained are then used as sources for TDT-MOC calculations on the exact 2D geometries. The process is repeated iteratively until a convergence criteria is reached on the IDT eigenvalue. This full 2D1D scheme is described in "Algorithm 6" of B. Faure's thesis [11].

The hybrid 2D1D scheme The hybrid version of the 2D1D scheme was also implemented by B. Faure and described as "Algorithm 7" in [11]. It differs from the full 2D1D scheme in its treatment of fissile sub-assemblies. Indeed, their cross sections are computed from a 2D MOC eigenvalue calculation, combined with a B-heterogeneous leakage model. The rest of the algorithm is similar to the full 2D1D, except that fissile slices' cross sections are not iterated over. This allows for an alternative axial description of each assembly.

Implementation of 2D1D in this project The exploratory nature of this project lead to considering the 2D1D formalism as an alternative to the "SCRAP-based" schemes. The implementation was made possible thanks to the help of G. Vallochi and JF. Vidal, whose

python script was adapted to the configurations presented in this work. It must be kept in mind that although the 2D1D solver architecture is part of APOLLO3, it is not part of the non-regression tests. This could imply that developments made since Faure's implementation might have altered its behavior. The 2D1D study is presented in more details, along with its associated "full core" results, in Chapter 4.

2.7 Finite Elements Methods (FEM) : treatment of the full core problem

The solvers used to treat the full core problem : MINOS, MINARET and NYMO are all based on Finite Elements Methods (FEM) for treating the spatial variable ([13], [15], [14]). This section aims at introducing the basic formalism necessary to understand the principles behind full core calculations.

2.7.1 MINARET (S_N)

The exact transport approach is implemented in MINARET as described in Moller and Lautard's work [13]. In this approach, the angular discretization relies on the discrete ordinates method. Its formulation leads to re-writing the mono kinetic, one group BTE as :

$$\mathbf{\Omega}_n \cdot \nabla \psi_n(\mathbf{r}) + \Sigma_t(\mathbf{r})\psi_n(\mathbf{r}) = q_n(\mathbf{r}) \tag{2.37}$$

as presented by Calloo et. al. [35]. Σ_t represents the macroscopic total cross section and q_n is the neutron source associated with direction $\mathbf{\Omega}_n$ which considers external and scattering sources from other directions. The multi-group equation is solved through the scattering cross sections expansion in Legendre polynomials [13]. In this work's context, the Legendre expansion's order will be set to 1 or 3 in S_N calculations, depending on the lattice scheme used. For each energy group, equation 2.37 is solved using a Discontinuous Galerkin Finite Elements Method (DGFEM). The core's domain C is meshed into 3D triangular prisms. The treatment of the solution's spatial dependence is assured by the DGFEM method, on the other hand the angular variable is treated through an S_N quadrature set. In a 2D projected geometry, hexagons are decomposed into triangular elements. Equation 2.37 is multiplied by a test function, integrated by parts to obtain the variational formulation of the transport problem. It is then discretized on each element, restricting the test functions' space to be the space of discontinuous piece-wise polynomials of order $p \geq 0$ [36]. In a DGFEM, the function space used to approximate the solution is the same as the one used to express the test functions. The main advantage of the Discontinuous technique is that no strong condition on continuity is set at the interface between elements, allowing for a

more independent, parallel treatment of the numerical solution on each subdomain. The exact details and derivation of the discretized variational form as well as the treatment of interfaces between elements can be found in Gastaldo et. al.'s work [36].

2.7.2 NYMO (P_N) approach

The NYMO solver is also based on a Discontinuous Galerkin FEM approach, like MINARET. It was extended by Assogba et. al. to support three dimensional meshes made from non-conforming unstructured 2D meshes, extruded along the third dimension [14]. In particular, the treatment of 3D prismatic meshes was made possible. In this work, the calculation mesh used in NYMO P_N calculations is exactly the same as the one generated for MINARET.

In [37], Bourhrara presents the numerical method implemented based on the the P_N variational formulation they proposed in an earlier paper [38]. Their solution is based on a discretization of the angular flux, in which they express each group's angular flux as a linear combination of spherical harmonics (eq. 2.31). The angular flux's moments are then discretized by projection on a chosen basis of linear independent polynomials [37]. The linear system which follows from this discretization is decomposed and re-written in terms of sparse matrices which are stored in Compressed Sparse Row format. The non-symmetric linear system can then be solved using the GMRES solver, suited for such matrix-vector operations [37].

It should be noted that voided configurations can be particularly hard to describe as Assogba claims that only "almost voided" regions with $\sigma \geq 10^{-6}b$ are supported [14].

2.7.3 MINOS

Diffusion Diffusion theory is based on Fick's Law of Diffusion, it is a convenient way to relate the neutron current to the flux's gradient. Mathematically, it is written :

$$\mathbf{J}_g(\mathbf{r}) = -\mathbb{D}_g(\mathbf{r})\nabla\phi_g(\mathbf{r}). \tag{2.38}$$

In equation 2.38, $\mathbb{D}_g$ is a 3×3 diagonal tensor, containing each group's directional diffusion coefficient. This law can be interpreted as expressing the tendency for neutrons in highly populated regions to diffuse towards regions where they are less numerous. This method is only acceptable at the full core scale and is not suited to treat assembly calculations.

In MINOS [2], a P1 approximation of the transport equation is used, limiting the flux's development of the spherical harmonics basis to order 1. The hypothesis of micro-reversibility

is used to treat anisotropic transfer cross sections. This leads to mixed dual FEM formulation corresponding to a coupled system between :

1. a balance equation: a modified version of the transport equation involving the current's divergence, modified total macroscopic cross section and neutron source term.

2. a vector equation, modified version of Fick's Law, involving the flux's gradient and the current.

This system of coupled equations is projected on a set of test functions $(\Psi, \mathbf{q})$. This is done multiplying the scalar balance equation with a test function Ψ. On the other hand, the vector equation is multiplied by the vector test function $\mathbf{q}$. Both equations are then integrated over the whole spatial domain. This is written as :

$$\begin{cases} \int_C \nabla \cdot \mathbf{J}\Psi + \Sigma_r \phi \Psi = \int_C S\Psi \\ \int_C \frac{\mathbf{J}\cdot\mathbf{q}}{D} + \nabla\Phi \cdot \mathbf{q} = \int_C \mathbf{Q} \cdot \mathbf{q} \end{cases} \tag{2.39}$$

where, C is the core's spatial domain, $\Sigma_r = \Sigma_t - \Sigma_{s0}$ is the modified total cross section, D is the P1 corrected diffusion coefficient $D = \frac{1}{3(\Sigma_t - \Sigma_{s1})}$. Applying Green's theorem and relevant boundary conditions to the first equation in 2.39 leads to the primal form of the diffusion problem. On the other hand, applying Green's theorem and boundary conditions to the reformulation of Fick's law in 2.39 leads to the dual form. The latter is the functional that needs to be optimized in order to solve for the neutron currents and Flux over the core's domain. In order to do so, the functional is discretized over Raviart-Thomas-Nedelec (RTN) elements [15]. Details about the mathematical definition of such elements can be found in Raviart and Thomas' work [39] and in Nedelec's work [40]. The elements used in MINOS are quadrilaterals K, they are obtained through a bi-linear mapping from a reference element $\hat{K} = [-1, 1] \times [-1, 1] \times [-1, 1]$. For this reason, the hexagons forming the ANTOINID core have to be subdivided into quadrilaterals. In this work, the hexagons are split into 4 trapezes.

Simplified Transport The treatment of the full core problem with MINOS can also be done in the SP_N approximation as it is an asymptotic limit of the exact transport equation [15]. In three dimensions, it is assumed that even components in the flux's expansion are scalar functions (ϕ_{2l}), and that odd components are vector functions (ϕ_{2l+1}) [20]. The differential operator then becomes the gradient for even scalar terms, and a divergence operator

for odd vector components. The SP_N equations can then be written as :

$$\begin{aligned}(2l)\boldsymbol{\nabla}\cdot\boldsymbol{\phi}^g_{2l-1}+\sigma^g_{2l}\phi^g_{2l}+(2l+1)\boldsymbol{\nabla}\cdot\boldsymbol{\phi}^g_{2l+1}&=S^g_{2l}\\(2l+1)\boldsymbol{\nabla}\boldsymbol{\phi}^g_{2l}+\sigma^g_{2l+1}\boldsymbol{\phi}^g_{2l+1}+(2l+2)\boldsymbol{\nabla}\phi^g_{2l+2}&=\mathbf{S}^g_{2l+1}\end{aligned}\tag{2.40}$$

where l is the order in the expansion so $l = 0, 1, 2, 3, ..., N$, in this work N will be set to 3. $\mathbf{S}_{2l+1}$ is the source term corresponding to scattering from groups $g' \neq g$ to group g. $\sigma^g_l = (2l+1)(\sigma^g_t - \sigma^{g\rightarrow g}_{sl})$ in which σ^g_{sl} is the l^{th} order of the scattering cross section for group g, and σ^g_t is the total cross section in group g. The even source components include contributions from the even terms of the scattering cross section expansion, as well as fissile sources contributions, through the term $\frac{1}{K_{eff}}\chi^g \sum_{g'} \nu\sigma^{g'}_{fiss}\phi^{g'}_0$.

To get the dual variational form of the SP_N equations, equations 2.40 are multiplied by odd and even test functions $\boldsymbol{\psi}_{2l+1}$ and ψ_{2l} and integrated over the physical domain. Green's theorem is applied to the odd equation, and vacuum boundary conditions are imposed. This required $\phi_{2l} \in L^2(C)$ and $\boldsymbol{\phi}_{2l+1} \in H(div, C)$, ie that $\nabla\cdot\boldsymbol{\phi}_{2l+1} \in L^2(C)$ and $\boldsymbol{\phi}_{2l+1} \in L^2(C)^3$ [15] [39]. Similarly as for diffusion, the mixed dual variational form is discretized on RTN elements using their associated interpolation functions basis. The discretization of test and solution functions is done using the Discontinuous Galerkin method.

2.8 Quantities of interest in SFR accidents

In a loss of coolant accident, the core's reactivity will change according to the neutron's balance evolution. The reactivity is defined in terms of the effective multiplication factor K_{eff} as

$$\rho = \frac{K_{eff} - 1}{K_{eff}}.\tag{2.41}$$

This quantity can thus also be interpreted as the tendency for a medium, given a specific geometry and composition, to be over-critical, $\rho > 0$ ($K_{eff} > 1$) or sub-critical $\rho < 0$ ($K_{eff} < 1$). Reactivity is related to the balance of neutrons produced over neutrons lost. Production of neutrons comes from the fission events, diffusion or (n,xn) reactions. Neutrons are lost when they are absorbed or when they escape through leakage.

Changes in reactivity will therefore be reflected in the neutron flux calculations, which in turns impacts the computed reaction rates.

2.8.1 Sodium voiding effect on reactivity

During a loss of coolant accident (LOCA), sodium can begin to boil so that a *void fraction* is introduced in the core. Alternatively, this voiding of sodium could be due to a leak in the cooling system. The void fraction in itself, as well as the location where the event takes place greatly impacts the effects on reactivity. These effects can be broken down into the following contributions :

1. Neutron absorption by sodium goes down, more neutrons are available for fission : positive effect on reactivity.
2. Loss of neutron moderation by sodium, the spectrum hardens : positive effect on reactivity.
3. Neutron leakage increases : negative effect on reactivity.

Sun et. al. [41] show that these effects on reactivity can be broken down in the following way:

$$\rho = 1 - \frac{L + C + F}{P} \tag{2.42}$$

in equation (2.42), C represents the capture term, F, represents the fission contribution, and their sum to the absorption term A as defined by Sciora et. al. [42], L represents the leakage term and P represents the production term, due to neutrons emitted during fission events as well as (n,xn) reactions.

State of the art SFR safety relies on designs that maximize the negative *leakage* contribution, ideally reaching a net negative voiding effect on reactivity, acting as a passive security system in the event of LOCA [42].

In order to evaluate the sodium voiding effect on reactivity, two static configurations are studied. The nominal configuration (NOM), where sodium density is normal, it will be compared to the voided configuration (VOID), in which all the coolant in the voided regions has been replaced by a simulated "void" (Na23 at $1.00 \times 10^{-15} b^{-1} cm^{-1}$).

The effect on reactivity is computed in the following way :

$$\Delta\rho_V = \rho_{VOID} - \rho_{NOM} = \left(\frac{1}{K_{eff,NOM}} - \frac{1}{K_{eff,VOID}}\right) \times 10^5. \tag{2.43}$$

In equation 2.43, reactivity is expressed in *pcm*; this convention is used in the rest of this text.

In 2013, C. Bay worked on comparing full core solvers performances on estimating the "void effect" as part of their Master's thesis [43]. Their work includes sodium void effect on reactivity calculations in MINOS (SP_3, SP_5) and MINARET (S_4, S_8) solvers. These full core calculations were performed on the Takeda SFR benchmark presented in [44]. It is interesting to note that full core calculations presented in Bay's work all consider the same 4 groups cross sections defined in Takeda's work [44], except for those corresponding to the added plenum medium. The latter were taken from the CFV calculations with 90% sodium and 10% steel in the nominal configuration, and 10% steel diluted in "void" for the voided configuration. Comparisons with presented lattice schemes can be hard to interpret as the origin of Takeda's sections was not found. Results from the present study will still be compared to those presented in Bay's work at the end of Chapter 4.

2.8.2 Doppler effect on reactivity

The temperature of a material will have a direct impact on the thermal agitation of the nuclides included in the composition of the material. This causes a broadening of resonant cross sections of the agitated nuclides. Indeed, a Doppler effect will be observed due to a change in the relative velocity between incident neutrons and thermally agitated nuclides.

The Doppler effect affecting the cross sections of reactions induced by neutrons will have a macroscopic effect on reactivity. Since the resonant absorption cross sections are broadened by the Doppler effect, increasing the temperature will have an overall negative effect on reactivity.

As for the voiding effect on reactivity, the Doppler effect will be evaluated in terms of its impact on reactivity (in *pcm*), according to the following equation :

$$\Delta\rho_D = \rho_{DOP} - \rho_{NOM} = (\frac{1}{K_{eff,NOM}} - \frac{1}{K_{eff,DOP}}) \times 10^5. \tag{2.44}$$

2.8.3 Reaction Rates

Reaction rates are of course not specific to the study of accidents in SFR. Nonetheless, they will be used as a finer comparison ground as their accurate computation is of prime importance for deterministic codes. Focus will be made on fission rates. Indeed, their accurate representation amounts for the greater part to determining the power distribution in the core, which is an essential part in its neutronic characterization. The voiding and Doppler effects on fission rates will therefore be studied and used to compare the different deterministic computational schemes considered. Fission rates are defined as the product of the fission

cross section with the neutron flux, as shown in equation 2.45. It can be noted that the flux being defined up to a multiplicative constant, it will thus be normalized such that the power dissipated in the core is 1 MW.

$$\tau_{fiss,i} = \sigma_{fiss,i}(E) N_i \phi(\mathbf{r}, E, \mathbf{\Omega}) = \Sigma_{fiss,i} \phi(\mathbf{r}, E, \mathbf{\Omega}) \tag{2.45}$$

where i represents a fissile isotope, $\sigma_{fiss,i}(E)$ is the energy dependent microscopic fission cross section of isotope i, N_i is isotope i's density and $\phi(\mathbf{r}, E, \mathbf{\Omega})$ is the neutron flux. The quantities of interest in this work will be the fission rates given by equation 2.45, integrated in energy and angle and summed over fissile isotopes. This reduces the fission rates field as a three dimensional scalar field, associating a fission rate value to each point in the three dimensional core model. In practice, fission rates are extracted by integrating fission rates fields over "cells" corresponding to mesh sub-volume elements. The normalisation used to treat the fission rates before the APOLLO3-TRIPOLI4 comparison is specified in Chapter 3.

CHAPTER 3 VALIDATION STUDY OF SCRAP SCHEME

3.1 The ANTOINID benchmark

The ANTOINID is an open core defined by Antoine Martini during his internship at LEPh in the summer of 2022. It is a simplified ASTRID-like SFR core. The ANTOINID core consists of 3 radial zones, the first being the C1 fuel zone, consisting of six rings of hexagonal fuel assemblies. The inner fissile C1 zone is surrounded by two rings of hexagonal C2 fuel assemblies, differing from C1 only in isotopic composition, with C1 having a lower Pu enrichment ($\sim 15.8\%$) than C2 ($\sim 17.9\%$). Lastly, the fissile zone is surrounded by three rings of hexagonal reflector assemblies. Axially, lower reflectors and sodium plenums are located under and above the fissile zone. Its properties are close to those of the CFV (low voiding effect core) version of ASTRID [42] [34] in terms of sodium voiding effects. Indeed, both were conceived in order to have a negative sodium voiding effect on reactivity, providing them with a passive safety system in case of accidental conditions. In order to achieve this negative sodium voiding coefficient, axial neutron leakage is maximized by introducing a ten centimeter height difference between C1 and C2 fuel assemblies. The open concept ANTOINID is a simplified core inspired from CFV version 2, described in Chenaud's paper [45]. CFV version 2 is itself adapted from version 1, presented at ICAP2012 by Varaine et. al. [34]. The ANTOINID geometry was made smaller and assemblies were slightly modified to reach criticality at the beginning of the fuel cycle. The aim of this academic core is to be used as a testing tool for the APOLLO3® code as well as the SEASON platform, under development at LMAG.

The SEASON platform couples neutronics codes capabilities with a thermo-physics code in order to analyze accidental transients. Historically, it had been developed using the ECCO/ERANOS calculation route traditionally used for SFR calculations.

With the aim of replacing ERANOS simulations with those of APOLLO3®, Martini's work using ECCO/ERANOS was adapted to APOLLO3® with the objective to validate both lattice and full core calculations for the ANTOINID core. Different hypotheses about the direct radial homogenisation of fuel sub-assemblies, neutron leakage and reflector models are tested.

First, the TRIPOLI-4 benchmark is defined along with the main quantities of interest. Secondly, the "Sodium Cooled Reactors with APOLLO3®" (SCRAP) approach is presented. Results for both lattice and full core MINOS calculations are presented and compared with TRIPOLI4 reference results. SCRAP results are analyzed, the scheme's performances and

drawbacks are discussed. An extension of the SCRAP scheme is then presented and used to test the hypothesis associated with the geometry used for the lattice flux calculation. Conclusions about the radial homogeneity and leakage model assumptions formulated by SCRAP are drawn.

3.2 Tripoli-4 benchmark definition

Definition of studied configurations The configurations studied are the nominal (NOM), voided (VOID), Doppler affected (DOP) and both voided and Doppler (DOP+VOID) cases. In the VOID configuration, all sodium coolant densities are replaced with a density approaching zero ($N = 1.00 \times 10^{-15}[b^{-1}cm^{-1}]$). In the DOP configuration, fuel temperature is increased from 1474 K to 2974 K. In the DOP+VOID configuration, both effects are taken into consideration.

On the full core scale, the voiding effect is taken to affect all assemblies in the C1/C2 radial zone. By that it is meant that plenums and lower reflectors are voided along with C1 and C2 fuel assemblies. Their sodium concentrations are set to $N = 1.00 \times 10^{-15}[b^{-1}cm^{-1}]$, and the radial reflector zone remains untouched.

It is worth noting that all temperatures in structures are set to 774 K, as well as in constituents of fuel assemblies that are not the fuel pellets themselves.

Definition of the nomenclature The ANTOINID core can be radially described by three distinct zone. As previously explained, the fissile zone is broken down into two C1 and C2 zones, surrounded by a radial reflector. The axial distributions in C1 and C2 zones are referred to as "assemblies", these are a collection of different materials including reflector and fuel zones. Each assembly can thus be broken down into a lower reflector ("SREFLLOW1/2"), a fissile zone ("C1/2") and an upper plenum ("SPLN1/2"). For the rest of this work, the C1/C2 "assembly" will refer to the collection of "sub-assemblies" ("SREFLLOW1/2, "C1/2" and "SPLN1/2"). This choice is done so that a "C1/2 assembly" refers to the complete axial distribution of materials, following the convention set by P. Archier et al. in [21].

The axial distribution of a C1 assembly modeled in Tripoli-4 is shown in figure 3.1. The lower part (gray) corresponds to the steel lower reflector, the second part (in red) is the C1 fuel sub-assembly and above that is the upper plenum, filled with sodium (yellow). The gray color represents steel structures, the yellow and orange zones correspond to sodium coolant. The red color represents the fuel rods, with a central voided zone shown in white. The C2 assembly is similar, with longer fuel rods, a different fuel composition, and a smaller plenum.

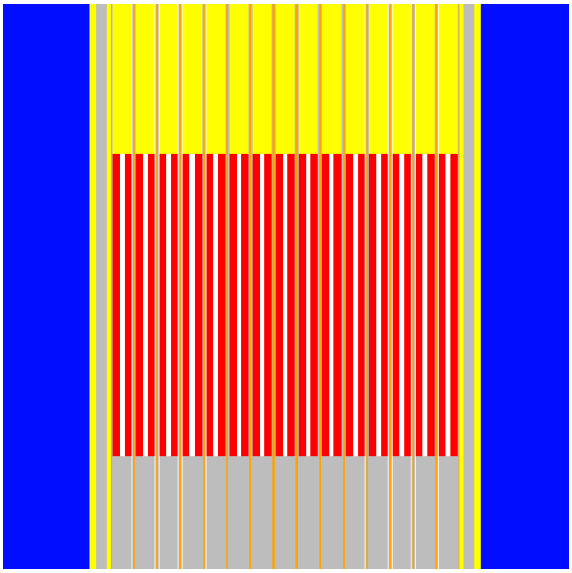

Figure 3.1 Graphical representation of the ANTOINID's assembly structure, from Tripoli-4 visualization tool.

The ANTOINID fuel sub-assembly model The ANTOINID fuel sub-assembly mainly consists of a hexagonal steel tube filled with 169 fuel rods. Each sub-assembly is cooled by sodium, inside and around the tube. A visual representation of the Tripoli-4 model can be found in figure 3.2. Monte-Carlo calculations are performed in the infinite lattice hypothesis by imposing specular reflective boundary conditions on a single sub-assembly. C1 and C2 fissile sub-assemblies only differ in fuel compositions. K_{inf}, void effect at constant temperature and Doppler effects at constant sodium concentration are presented in tables 3.1 and 3.2. In order to perform these calculations, three normalized punctual neutron sources are initialized at different heights $z = 50, 75, 100$ cm, at the sub-assembly's symmetry center $(x, y) = (0, 0)$. These only come into play at $t = 0$, initializing the neutron population. The subsequent neutrons are simulated using subsequent histories produced. A total of 40 000 batches of 10 000 neutrons are simulated for each configuration. In the case of voided configurations, calculation times can increase from time scale of a day to more than

C1 sub-assembly	K_{inf} T4±5 pcm	Fuel Temp. (K)	$\Delta\rho_V$ (pcm)	Void	$\Delta\rho_D$ (pcm)
NOM	1.20746	1474	2663 ± 6	Yes	-665 ± 6
VOID	1.24757	2974	2854 ± 6	No	-474 ± 6
DOP	1.19784				
DOP+VOID	1.24024				

Table 3.1 Tripoli-4 results for C1 fuel sub-assembly : K_{inf} different conditions, voiding and Doppler effects on reactivity.

C2 sub-assembly	K_{inf} T4 ± 5 pcm	Fuel Temp. (K)	$\Delta\rho_V$ (pcm)	Void	$\Delta\rho_D$ (pcm)
NOM	1.28890	1474	2517 ± 5	Yes	-520 ± 6
VOID	1.33211	2974	2654 ± 5	No	-382 ± 6
DOP	1.28032				
DOPVOID	1.32536				

Table 3.2 Tripoli-4 results for C2 fuel sub-assembly : K_{inf} different conditions, voiding and Doppler effects on reactivity.

a week. Given the time constraints associated with this project, it was attempted to cut down calculation times for voided configurations. In order to optimize the simulation times, the "$TIME\_SUP$ NEUTRON" option was introduced. This parameter allows to specify an upper bound for the simulated neutrons' life time. It was observed that limiting each neutron's life time to 10^{-5}, 10^{-4}, 10^{-2} or 1 seconds didn't have any significant statistical impact on the K_{inf} values calculated. Indeed, all discrepancies in the K_{inf}'s were of the order of ~ 10 pcm, which was well within the 1 standard deviation range used to conduct this quick survey. Since using this restriction on a larger number of neutron histories greatly cut down the MC simulation time, it was decided to proceed with setting the parameter to 10^{-5}, keeping in mind that it could introduce biases of the order of ~ 10 pcm. This should be kept in mind when comparing AP3 results with those presented in tables 3.1 and 3.2. Additional work could be done in further assessing this parameter's influence, however since the main focus of this project was to study the deterministic AP3 approaches in more detail, it appeared outside of this work's scope.

The ANTOINID core model The full ANTOINID core Monte Carlo simulation was implemented in Tripoli-4. The geometry was defined by Antoine Martini in the native T4 language using a combinatorial volumic approach. In order to obtain more detailed scores for fission rates, the model includes an axial discretization of the fuel sub-assemblies in 10 cm high sub-volumes. This amounts to a total of eight and nine sub-volumes for C1 and C2 fuel sub-assemblies respectively. Fission scores in each of the sub-volumes are used as a reference when comparing with deterministic calculations.

Results for full core calculations in the four configurations are presented in table 3.3. Voiding and Doppler effects on reactivity are calculated. Normalized fission rate maps are presented in figure 3.4. Nominal (a), voided (b), Doppler (c) and Doppler+voided (d) configurations are shown. In the rest of this work, fission rates are normalized so that their sum over all fissile regions considered, is equal to the total number of fissile regions. This can be expressed

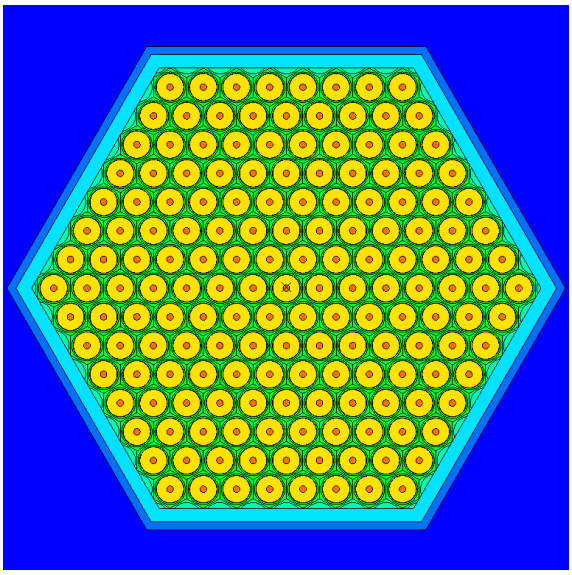

Figure 3.2 Graphical representation of the ANTOINID's 2D fuel sub-assembly structure, from Tripoli-4 visualization tool.

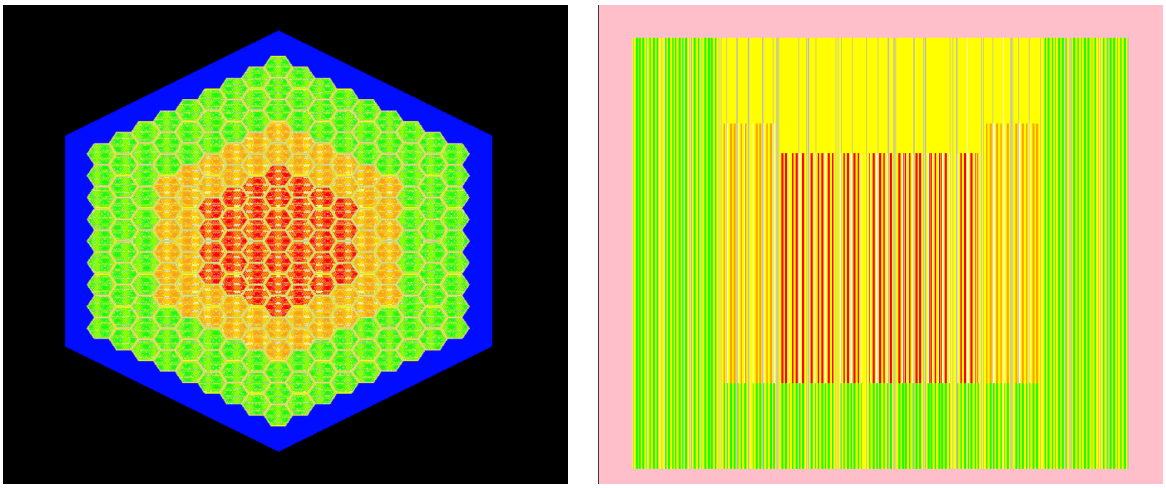

(a) *Top view of the ANTOINID core.*

(b) *Axial distribution of materials in the core, view on the y=0 axis.*

Figure 3.3 Radial (left) and axial (right) distribution of materials in the ANTOINID core. To the left, C1 fuel assemblies (red), C2 fuel assemblies (orange) and radial reflectors (green). To the right, lower reflector (green), C1 (red) and C2 (orange) fuel sub-assemblies and their height difference, covered by sodium plenum (yellow).

mathematically as :

$$\sum_{i}^{N=782} \tilde{\tau_i} = N = \sum_{i}^{N=782} \frac{N\tau_i}{\sum_i^N \tau_i} \tag{3.1}$$

where $N = 782$ is the total number of fissile volumes considered: 728 from the eight 10 cm slices of C1 and C2 sub-assemblies, and 54 from C2 sub-assemblies on the last 10 cm slice, $\tilde{\tau_i}$ are the normalized rates and τ_i are the rates before normalization. In the 2D maps presented, fission rates have been summed over all fissile isotopes, and have been axially integrated over the fissile part of the core. It is worth mentioning that this type of normalization is necessary in order to allow for a code to code comparison as a critical flux solution is only defined up to a normalization constant. A breakdown of axial dependence of fission rates can be seen in figure 3.5. Only fission rate scores from the "bottom-left" to "top-right" traverse are considered. Additional T4 calculations are performed in order to try to isolate contributions of voiding effects on reactivity. Only the sodium plenum is voided, then only the sodium in fuel regions. Lastly, both are voided, leaving the lower reflector intact.

Analysis of fission maps shown in 3.4 reveals that voiding sodium coolant leads to an overall decrease of fission rates in the central part of the core, correlated with an increase in the outer assemblies' fission rates. This could be attributed to a "flattened" flux distribution in the voided configurations. This is due to the fact that neutrons travel greater distances in voided configurations, thus leaving more possibilities for neutrons from high flux zones to migrate to other zones. On the other hand, it can be seen that the Doppler effect on fission rates increases the variation in fission rates from outer to inner fuel assemblies. This effect is due to the broadening of resonant absorption cross section due to thermal agitation of fissile nuclides [1]. Since the absorption cross section is the sum of the fission and capture cross sections, it is hypothesized that the broadening of fission cross sections is the main source for this difference between NOM/DOP and VOID/DOP+VOID configurations. The Doppler broadening of capture cross sections of isotopes present in the fuel pellets would then be responsible for the negative Doppler effect on reactivity presented in table 3.3.

Config.	K_{eff} TRIPOLI4	σ (pcm)	Fuel Temp. (K)	$\Delta\rho_V$ (pcm)	Void	$\Delta\rho_D$ (pcm)
NOM	1.01518	4	1474	-749±9	No	-639±6
VOID	1.00752	8	2974	-573±9	Yes	-463±11
DOP	1.00864	5	Combined DOP+VOID	$\Delta\rho_{D+V}$ (pcm)		
DOP+VOID	1.00284	8		-1212±9		

Table 3.3 Tripoli-4 results for full core simulations, K_{eff} in different conditions, voiding effects at both temperatures and Doppler effects in both non-voided and voided configurations.

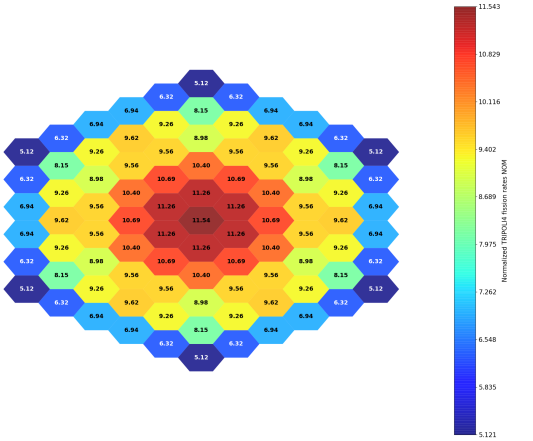

(a) *Axially integrated reference T4 fission rates, NOM configuration.*

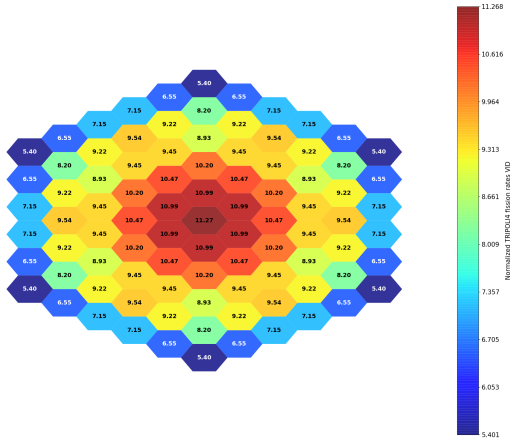

(b) *Axially integrated reference fission rates, VOID configuration.*

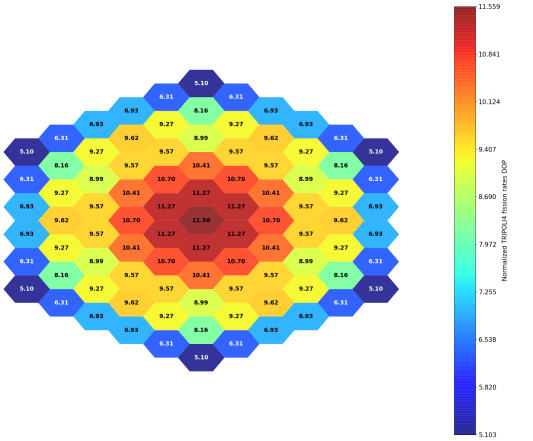

(c) *Axially integrated reference T4 fission rates, DOP configuration.*

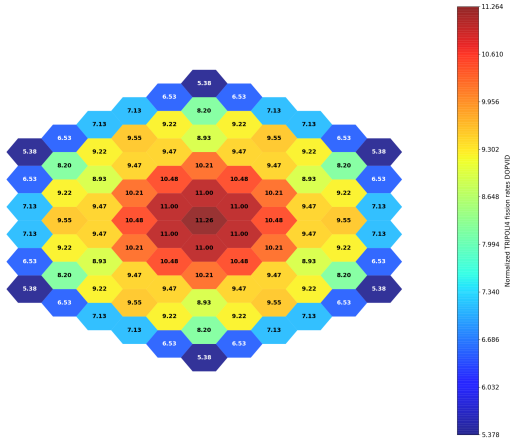

(d) *Axially integrated reference T4 fission rates, DOP+VOID configuration.*

Figure 3.4 Reference fission rates for Nominal (a), voided (b), Doppler (c) and Doppler+voided (d) configurations, axially integrated and symmetrized.

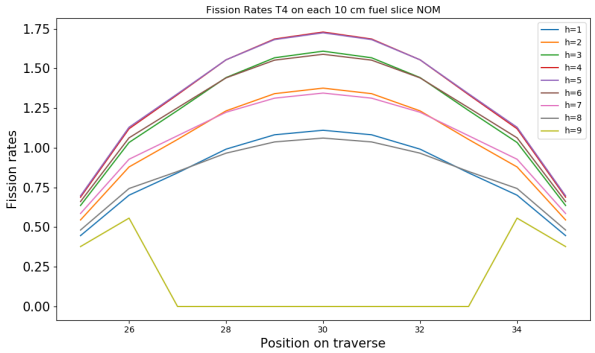

(a) *Fission rates at each 10 cm fuel height, NOM configuration.*

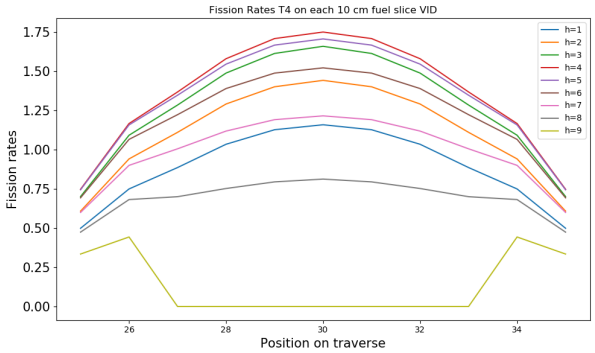

(b) *Fission rates at each 10 cm fuel height, VOID configuration.*

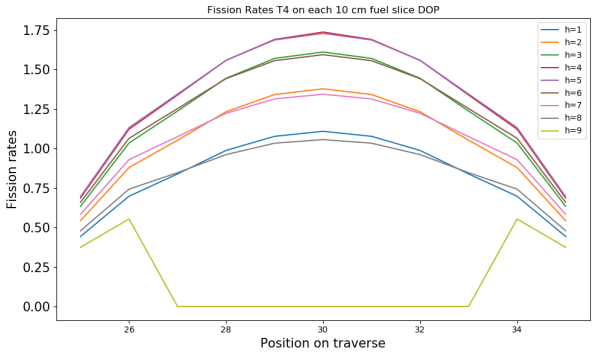

(c) *Fission rates at each 10 cm fuel height, DOP configuration.*

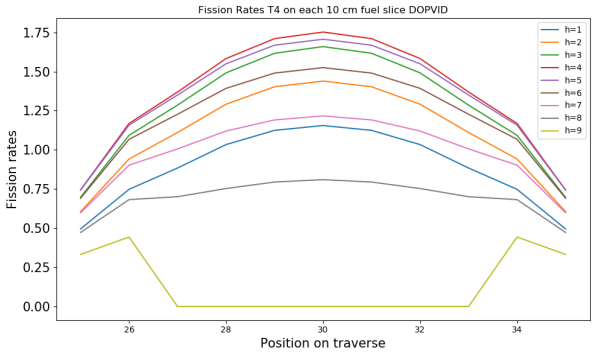

(d) *Fission rates at each 10 cm fuel height, DOP+VOID configuration.*

Figure 3.5 Fission rates on radial traverse, integrated on each 10 cm fuel slice.

Figure 3.5 helps comparing the axial effects on fission rates. Indeed, a comparison from left to right (non-voided to voided) reveals that the fuel slices most impacted by the voiding are, $h = 8$ (grey), $h = 9$ (yellow) and $h = 7$ (pink). These correspond to the fuel slices closest to the voided sodium plenum, with $h = 8$ and $h = 9$ slices directly sharing interfaces with the plenum. It is hypothesized that most of the decrease of fission rates in these slices is due to the voided regions in the sodium plenum acting as preferred leakage channels for neutrons to escape the core. This leaves less possibility for outbound neutrons to be reflected back to fuel sub-assemblies and thus leads to a strong decrease of reaction rates in these regions. On the other hand, slices $h = 2$, $h = 1$ and $h = 3$ experience a slight increase in fission rates, due to the loss of slightly moderating effects of sodium, the neutron energy spectrum hardens leading to a slight increase in these regions. This could be due to the fact that lower reflectors are primarily made of steel, leaving comparatively less neutron leakage channels than the upper plenum. This effect could also potentially be due to the chosen normalization as the decrease of fission rates in the upper slices would tend to increase rates in other zones as the sum of rates is imposed to be constant.

Spatial dependence of voiding effects on reactivity The sodium void effect on reactivity being highly dependent on the spatial distribution of voided regions, some tests were performed varying the voided zone to quantify the compensating effects on reactivity. First, only the upper plenum zones above the C1 and C2 zones were voided (VOID = SPLN), then only the C1 and C2 fuel regions were voided (VOID = C) and lastly, both plenum and fuel regions are voided. The resulting eigenvalues and effects on reactivity are presented in table 3.4

It is interesting to note that the total reactivity loss due to the voiding of the upper plenum is -1161 pcm. This negative effect in reactivity is understood to be due to the leakage of neutrons through axial void channels. On the other hand, the reactivity increase due to

Configuration	K_{eff} T4	σ (standard deviation)	$\Delta\rho_V$ pcm
NOM	1,01518	4.11×10^{-5}	0
VOID = SPLN	1,00335	1.11×10^{-4}	-1161
VOID = C	1.02410	1.15×10^{-4}	858
VOID = C+SPLN	1.01033	1.39×10^{-4}	-473
VOID=ALL	1.00752	7.84×10^{-5}	-749

Table 3.4 K_{eff} and sodium void effects obtained for T4 simulations, spatial dependence on sodium void effect.

voided fuel regions is +858 pcm, which is taken to be due to the decrease in neutron moderation/absorption by sodium leading to a higher energy neutron spectrum which increases the chances of witnessing higher energy fission events. These two effects' opposing behaviors are displayed here as it can be seen that voiding both C and SPLN zones results in a net -473 pcm effect. It can be noted that independently, both effects do not add up to the combined effect. The difference is taken to be due to the additional leakage introduced by a greater production in the upper fissile zones in the voided case. In order to get to the total -749 pcm effect, an additional -276 pcm is required, this is taken to be due to the lower reflector's voiding which would participate to the negative neutron leakage contributions.

These results will be used as a reference when considering the ANTOINID's neutronic behavior. APOLLO3 deterministic scheme's performances will be assessed by considering :

1. Errors on reactivity (pcm) : $\Delta\rho = (\frac{1}{K_{eff,AP3}} - \frac{1}{K_{eff,T4}}) \times 10^5$
2. Errors on void and Doppler effects on reactivity (pcm) : $\Delta\Delta\rho = \Delta\rho_{AP3} - \Delta\rho_{T4}$
3. Relative errors on fission rates : $\Delta\tau_f = (\tau_{f,AP3} - \tau_{f,T4}) \times 100/\tau_{T4}$

3.3 SCRAP project scheme approach

The SCRAP (Sodium Cooled Reactors with APPOLLO 3) project scheme was developed by Jean-François Vidal and Maciej Zajaczkowski in order to access the needs of LEPh and LE2C for a fast and robust APOLLO3 SFR scheme. SCRAP was previously validated by comparison with TRIPOLI4 on the larger JF-36 benchmark core, the 3600 MW variant of the Japanese Sodium Fast Reactor (JSFR) [30].

The first goal of this project is to validate and analyze performances obtained by SCRAP on the ANTOINID benchmark. The scheme is performed in the classical two computational steps. In the first step, assembly calculations are performed in order to generate sets of microscopic cross sections, as a function of local parameters. In this work, the parameters used are the fuel temperature and the sodium density. These are stored in the MPO format, specific to APOLLO3. In the second step, the full core calculation is performed using the MINOS solver [15].

3.3.1 SCRAP lattice calculations

The lattice geometries are described and generated using the INCA tool, currently in development at DER/SPRC. Three types of geometries are generated corresponding to fissile,

reflector and plenum sub-assemblies. All three consist of a primary hexagonal structure filled with 169 cylinders. In fissile sub-assemblies, the cylinders harbour solid fuel pellets (MOX). In the reflectors, these cylinders are made of steel and in plenum, they are filled with sodium. The three $1/12^{th}$ of geometries are shown in figure 3.6. The latter are used for zone and physical properties assignments, in figure 3.6, each color represent a different zone. Most notably, the outermost fuel pins are treated separately, allowing for different self-shielding properties. The coolant is also treated differently, depending on whether it is located inside or outside the hexagonal tube. This allows for a different treatment of each zone during the self-shielding step. The tracking parameters for Tone's method involve twelve horizontal and three vertical angles. The integration step is set to 0.1 cm. These are parameters that were recommended in the reference AP3 scheme for SFRs presented in P. Archier et al. [21].

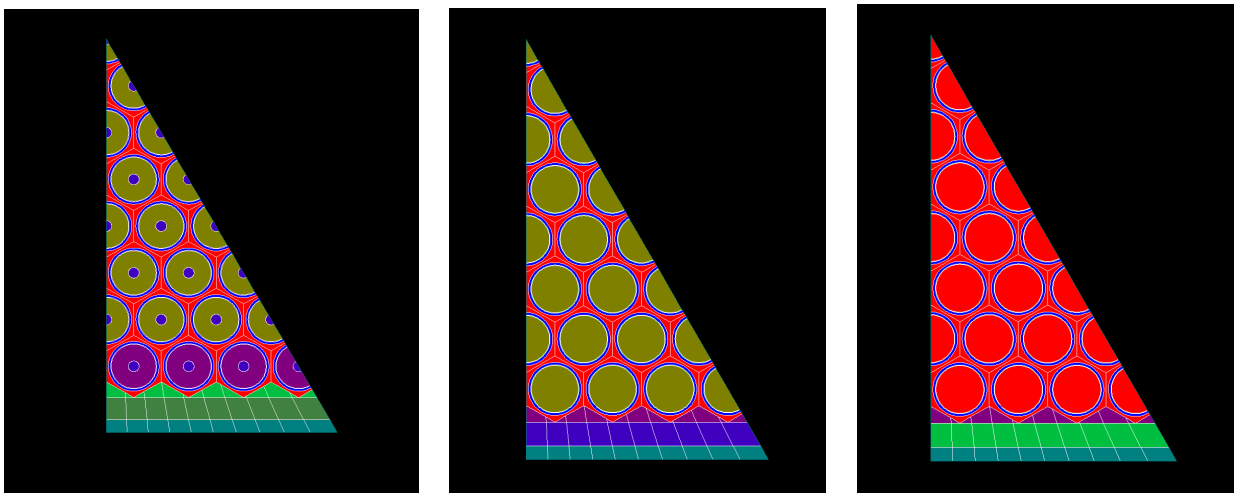

(a) *Fissile sub-assembly geometry* $(1/12^{th})$.

(b) *Reflector sub-assembly geometry* $(1/12^{th})$.

(c) *Plenum sub-assembly geometry* $(1/12^{th})$.

Figure 3.6 INCA generated unstructured geometries for Fissile (a), Reflector (b) and Plenum (c) sub-assemblies. Colors show associated zones, allowing for the assignment of different physical properties.

First, the fissile sub-assemblies are treated; Tone's method for resonance self-shielding [22] [24] is performed on the exact 2D geometry (fig. 3.6(a)), on a 383 groups fine energy mesh. Once the self-shielding is performed, the exact 2D geometry is turned into a homogeneous 1D equivalent geometry, using the Flux-Volume homogenization method. In order to do so, a single node, one dimensional mesh is generated. Specular reflection conditions are applied, implying that the considered geometry is effectively an infinite homogeneous "paste". It must be noted that this flux calculation geometry thus becomes equivalent to an homogeneous 0D calculation. Since the homogenized geometry is rotationally invariant, the integration

direction for the IDT plane flux calculation is arbitrarily chosen to be the x-axis. The homogenized cross sections are computed by summing the self-shielded cross sections over the regions in the exact mesh, weighting them by the product of the flux and the volume of the corresponding region. This requires the initialisation of a flat flux on the exact 2D geometry. APOLLO3's IDT solver is called to perform a S_N flux calculation on the 1D homogenized geometry, using the same 383 groups energy mesh. The angular treatment is performed through a (8,8) double Gauss-Legendre quadrature. For fissile sub-assemblies, the B1 homogeneous model is used and a search for the critical B^2 is performed. The treatment of sub-critical assemblies is also performed in two step. First, Tone's self-shielding method is used on the exact two dimensional geometries (fig. 3.6 (b) and (c)). Then, the latter are homogenized, similarly as for fissile sub-assemblies. A S_N source calculation is performed on the homogenized geometry, using the neutron leakage rate obtained from fissile sub-assemblies as the source term.

The neutron leakage out of C1 fuel sub-assemblies is taken to act as a source for the plenum located directly on top of the inner fuel part of the core as well as for the lower reflectors located just underneath C1. The leakage calculated for C2 are taken as a source for the radial reflectors, the lower reflectors under C2 fuel as well as for the plenum above C2 fuel sub-assemblies.

Condensation of cross sections from the 383 groups energy mesh to 33 groups outputs is performed using the Flux-Volume technique.

The main hypotheses made in this approach are the following :

1. *Homogeneity* : A homogeneous 1D sub-assembly geometry is valid for a flux calculation on fissile zones. This flux calculation can be performed on a 383 energy groups mesh.

2. *Leakage* : Neutron leakage terms can be computed using the B1-homogeneous model.

3. *Reflector models* : Reflectors can be represented by a homogeneous 1D geometry. The cross sections can be obtained through an independent source calculation on 383 energy groups. The leakage out of the fissile sub-assemblies acts as the external source.

These three primary hypotheses will be tested throughout the rest of this work.

Intermediate results : lattice calculations K_{inf} results for the SCRAP scheme in an infinite lattice with no leakage model are presented in table 3.5. As the infinite lattice case with no leakage is equivalent to a single fuel sub-assembly with reflective specular boundary conditions, these results are compared with Tripoli-4 benchmark values, for both C1 and C2,

while voiding and Doppler effects on reactivity are calculated and presented in tables 3.6 and 3.7.

It is important to note that the times indicated in table 3.5 correspond to the "No Leakage" case. For cross section library production with a homogeneous leakage model and source calculations for sub-critical sub-assemblies, the total time required is around 330 seconds and the calculation requires about 4.10 GiB of RAM. Most of the computation time (∼200 seconds) is spent in the module handling isotopes, materials and geometries while the self-shielding step takes about 15s. The time spent in the IDT flux solver to compute the 383g flat spatial flux is 5 seconds (∼2.5s per fuel sub-assembly) and each of the source calculations for the reflector and plenum takes from 10 to 20 seconds. The times recorded correspond to cases executed on 16 threads in parallel, CPU type is Intel(R) Xeon(R) Silver 4210R, clocked at 2.40GHz. Unless specified, all lattice and full core calculations presented in the rest of this work are performed as such.

3.3.2 SCRAP full core calculations

The solver chosen for SCRAP full core calculations is MINOS in the simplified diffusion approach to neutron transport. The ANTOINID's geometry is defined in a "hexagonal-z" structured mesh : first the 2D zones are defined, involving the innermost C1 zone composed of six rings of hexagons, then the C2 zone is defined, consisting of two rings. Lastly, three rings are added to constitute the radial reflector zone. The 2D mesh composed of hexagons is then extruded along the z axis, the chosen axial discretization is to add 1 node every 2.5 cm. In each of the 2D radial zones, an axial composition is specified, attributing physical properties along the axial dimension.

The MINOS solver relies on a Raviart-Thomas Nedelec finite element discretization [15]. For this reason, each 2D hexagonal sub-assembly is subdivided into quadrilateral sub-cells. A

		SCRAP No Leakage				T4	
t (s)	Config.	K_{inf} IDT		$\Delta\rho$ AP3 / T4 (pcm)		$K_{inf} \pm 5$ pcm	
		C1	C2	C1	C2	C1	C2
45	NOM	1,20411	1,28524	-230	-221	1,20746	1,28890
59	VOID	1,24416	1,32821	-220	-220	1,24757	1,33211
58	DOP	1,19456	1,27654	-230	-231	1,19784	1,28032
58	DOP+VOID	1,23670	1,32142	-231	-225	1,24024	1,32536

Table 3.5 Calculated K_{inf} for C1 and C2 fuel, difference in reactivity between AP3 SCRAP/T4

	T=1474K		T=2974K	
	$\Delta\rho_{VOID}$ SCRAP (pcm)	AP3-T4 (pcm)	$\Delta\rho_{VOID}$ SCRAP (pcm)	AP3-T4 (pcm)
C1	2673	11	2852	2
C2	2517	0	2661	7

Table 3.6 Comparison of voiding effects on reactivity between SCRAP calculations and T4 reference.

	VOID = No		VOID = Yes	
	$\Delta\rho_{DOP}$ SCRAP (pcm)	AP3-T4	$\Delta\rho_{DOP}$ SCRAP (pcm)	AP3-T4
C1	-664	1	-485	-11
C2	-530	-10	-387	-5

Table 3.7 Comparison of Doppler effects on reactivity between SCRAP calculations and T4 reference.

trapeze splitting is used, introducing four sub-cells per hexagon. The choice of finite element order is 1 for both radial and axial elements. The calculation mesh used for the 2D radial discretization can be seen in figure 3.7.

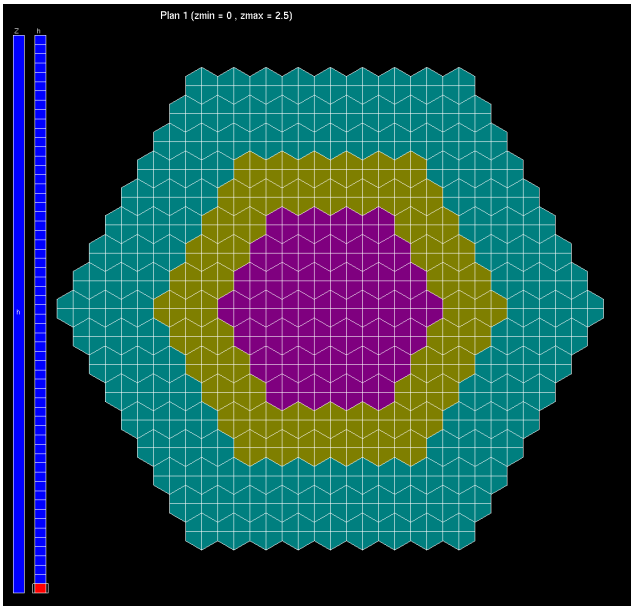

Figure 3.7 "Trapezoid splitting" calculation mesh used in MINOS.

The obtained K_{eff} are reported in the first column of table 3.8. The differences in reactivity between un-voided and voided calculations are computed, as well as Doppler effects on reactivity. These effects are compared to the reference T4 results previously shown in table 3.3.

SCRAP cross sections were also used to solve the full core problem in the simplified transport approximation. Similar mesh and finite elements methods as the ones presented for the diffusion approximation are used to solve the SP_3 equations on the full core geometry. Calculated $K_{eff}s$ and corresponding effects on reactivity are presented in the second column of table 3.8

For both Diffusion and SP_3 approximate transport operators, three dimensional fission rates fields are computed from the obtained neutron flux. Rates are normalized during post treatment and compared to normalized TRIPOLI-4 rates. The three dimensional rates are integrated along the axial dimension, enabling an assessment of the solver's performances through analysis of the associated 2D error distribution.

The Root Mean Squared error (RMS) associated with each error distribution is computed using the following formula :

$$RMS = \sqrt{\frac{1}{N}\sum_{i=1}^{N}(\Delta\tau_i^{\%})^2} \tag{3.2}$$

where N is the number of axially integrated fission rates and $\Delta\tau_i^{\%}$ is defined as the relative error between normalized SCRAP and T4 fission rates, expressed in %.

Diffusion Results on spatial fission distribution obtained from SCRAP cross sections using the MINOS diffusion formalism are now presented. Relative errors on normalized, axially integrated fission rates obtained from SCRAP/ MINOS Diffusion calculations are presented in figures 3.8 (a), (b), (c) and (d). It is worth mentioning that diffusion calculations with the MINOS solver involving cross sections from the SCRAP lattice step require around 100 seconds and 3.80 GiB of RAM for nominal and Doppler affected calculations. In the case of voided configurations, the RAM usage is unchanged, however calculations take about 150 seconds. This is due to a slower convergence of the fission source.

The RMS error associated with the four configurations are $RMS_{NOM} = 0.89\%$, $RMS_{VOID} = 0.98\%$, $RMS_{DOP} = 0.86\%$ and $RMS_{DOP+VOID} = 0.99\%$.

These quadratic errors are rather satisfying judging by the fuel sub-assembly homogeneity hypothesis introduced at the SCRAP lattice stage.

In order to get a better understanding of the radial and axial effects on the biases introduced on fission rates, the relative error on normalized rates (AP3-T4 (%)) is plotted in figure 3.9. The radial traverse is taken across the ANTOINID core, from a vertex of the hexagonal shape to its symmetric. Each 10 cm height in fuel sub-assemblies is represented by a different color. Additionally, figure 3.10 shows the evolution of the relative error on fission rates with respect

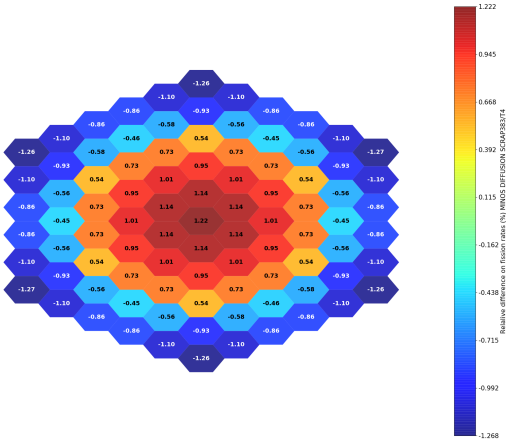

(a) *Relative error on fission rates, NOM configuration.*

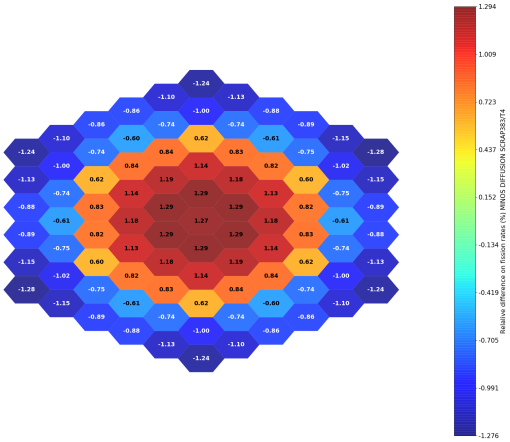

(b) *Relative error on fission rates, VOID configuration.*

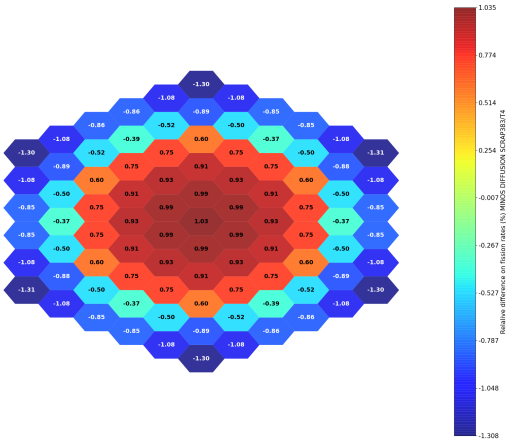

(c) *Relative error on fission rates, DOP configuration.*

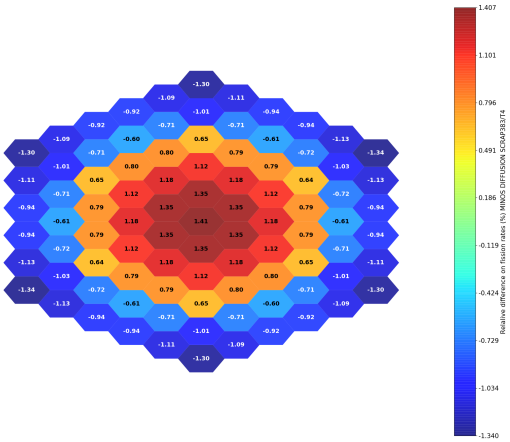

(d) *Relative error on fission rates, DOP+VOID configuration.*

Figure 3.8 Relative difference (%) AP3-T4 on fission rates obtained from SCRAP in diffusion calculations in MINOS. Nominal (a), voided (b), Doppler (c) and Doppler + voided (d) configurations.

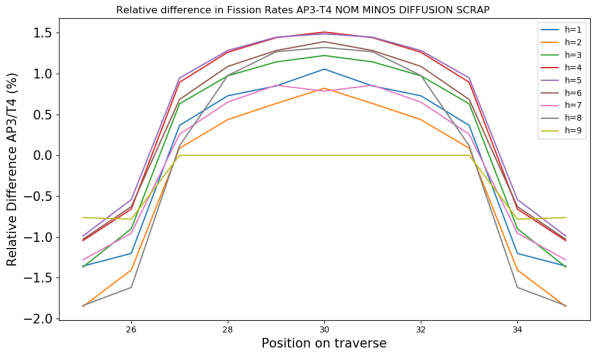

(a) *Relative error on fission rates, NOM configuration.*

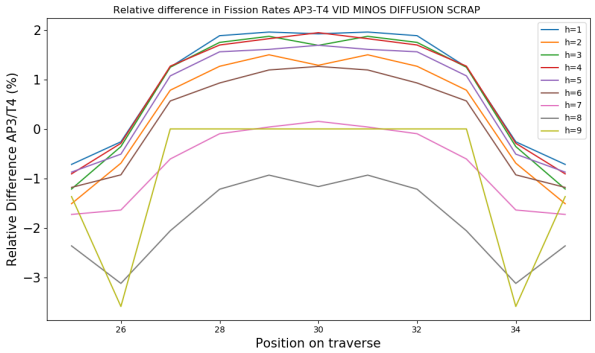

(b) *Relative error on fission rates, VOID configuration.*

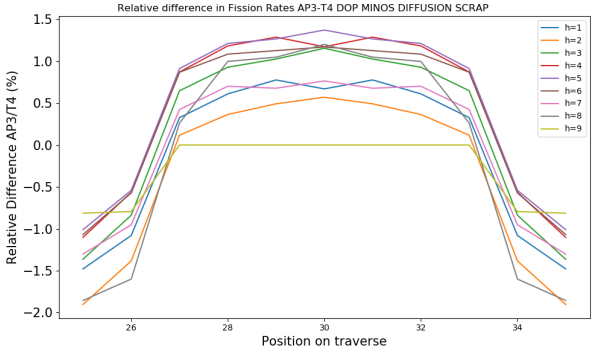

(c) *Relative error on fission rates, DOP configuration.*

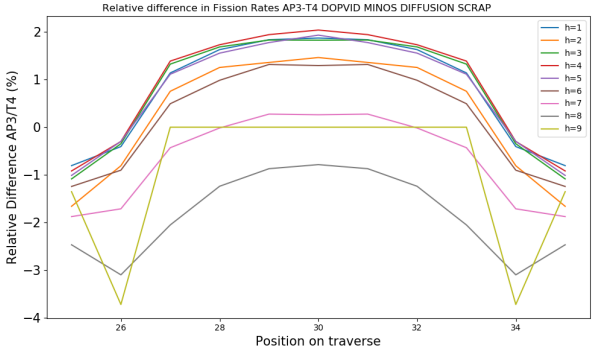

(d) *Relative error on fission rates, DOP+VOID configuration.*

Figure 3.9 Relative difference (%) AP3-T4 on fission rates obtained from SCRAP diffusion vs radial position (ERANOS hexagon numbering). Nominal (a), voided (b), Doppler (c) and Doppler+voided (s) configurations. Radial traverse across the core.

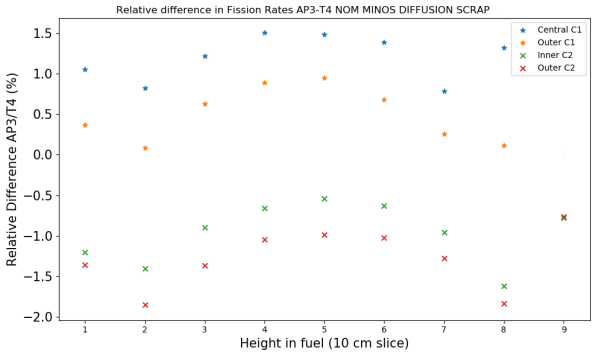

(a) *Relative error on fission rates, NOM configuration.*

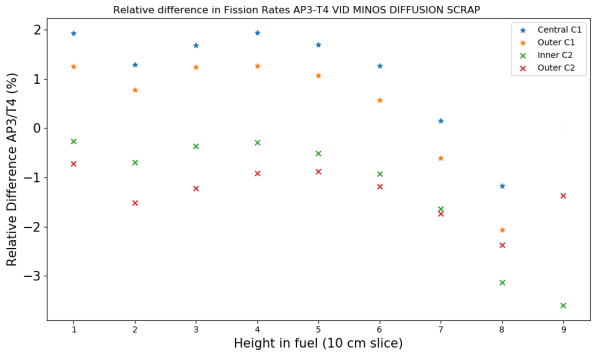

(b) *Relative error on fission rates, VOID configuration.*

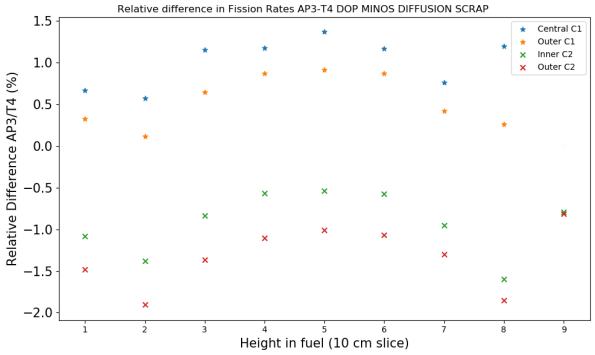

(c) *Relative error on fission rates, DOP configuration.*

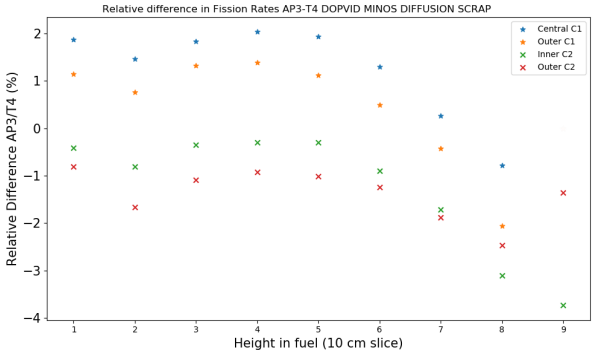

(d) *Relative error on fission rates, DOP+VOID configuration.*

Figure 3.10 Relative difference (%) AP3-T4 on fission rates obtained from SCRAP diffusion vs axial position (10 cm slice). Nominal (a), voided (b), Doppler (c) and Doppler+voided (d) configurations. Axial traverse on C1 central and outer assemblies, C2 inner and outer assemblies.

SCRAP $t_{lattice}$ = 330 s RAM $\sim$ 4.1 GiB	TRIPOLI-4 $K_{eff}\pm$8 pcm	$\Delta\rho$ MINOS Diffusion	$\Delta\rho$ MINOS SP_3
NOM VOID DOP DOP+VOID	1.01518 1.00752 1.00864 1.00284	-118 pcm 122 pcm -171 pcm 86 pcm	63 pcm 377 pcm 13 pcm 343 pcm
$\Delta\rho_V$ (pcm) T=1474K/2974K	-749/-573	-509/-316	-436/-244
Error $\Delta\rho_V$ (pcm) T=1474K/2974K	0/0	240/258	313/330
$\Delta\rho_D$ (pcm) Void = No/Yes	-638/-463	-692/-500	-689/-497
Error $\Delta\rho_D$ (pcm) Void = No/Yes	0/0	-53/-36	-50/-34
Time (s)	403 670	174	592
RAM, core calculation	Not recorded	3.80 GiB	14.89 GiB

Table 3.8 Comparison of MINOS Diffusion and SP_3 calculation. For all four configurations, error on the eigenvalue, calculated void and Doppler effects and their associated errors are displayed.

to the discrete 10 cm height in fuel. The assemblies represented are central and outer C1 as well as inner and outer C2 assemblies, all located on the same radial traverse as previously described. An illustration of the radial and axial traverses used can be found in figure A.1 of Appendix A.

It should be noted that in figure 3.9, the error associated with $h = 9$ (fuel sub-assemblies in $110cm \leq z \leq 120cm$) is zero for radial positions from 27 to 33. This is simply because fuel in C1 assemblies stops at a $110cm$ height. For similar reasons, no relative error is associated with $h = 9$ for C1 assemblies in figure 3.10.

Simplified Transport The results from SCRAP cross section used in full core MINOS SP_3 are now presented. The relative errors on fission rates calculated from MINOS SP_3 using the cross sections generated by the SCRAP lattice scheme are presented in figures 3.11 (a)(b)(c) and (d) The associated root mean squared errors are $RMS_{NOM} = 0.63\%$ in the nominal configuration, $RMS_{VOID} = 0.64\%$, $RMS_{DOP} = 0.60\%$, and $RMS_{DOP+VOID} = 0.65\%$.

Additionally, errors on fission rates along the axial traverses in central and outer C1 assemblies, as well as inner and outer C2 assemblies are presented in figure 3.12.

The simplified transport calculations performed take around 220 seconds for NOM and DOP

configurations, while the voided VOID and DOP+VOID configurations require around 580 seconds. It is also worth taking into account that the SP3 solution required considerably more RAM than the diffusion approach, using almost 15 GiB per configuration.

3.4 SCRAP Results Analysis

The SCRAP scheme appears to provide acceptable results at the lattice step. Indeed, despite the apparent important bias on reactivity ($\sim -230pcm$), the void and Doppler effects on reactivity given by equations 2.43 and 2.44 are correctly captured, despite the strong hypothesis made for the lattice calculation. The results hint at the fact that spatial homogenization of the ANTOINID's fuel sub-assemblies seems to be a valid assumption. This is not a totally surprising since SFR fuel sub-assembly designs are generally radially "homogeneous" from a neutronic point of view. This is mostly due to the fact that no strong neutron thermalizers are present. This wouldn't be the case when using water as a moderator for example. Since neutrons are not thermalized, their mean free paths are more important, making them less sensible to radial heterogeneity. This property allowing for fast IDT 1D S_N calculations on the homogenized geometry appears as the scheme's greatest strength, enabling fast and accurate representations of NOM and DOP configurations at the full core scale. Indeed, for both SP3 and Diffusion calculations, Doppler effects on reactivity seem correctly captured. Relatively small biases are introduced with the negative Doppler effect on reactivity being over estimated by about 50 pcm. However, both Diffusion and SP_3 cases fail at correctly capturing the effect of sodium voiding in plenum, fuel and lower reflector regions. Indeed, in the diffusion approximation, the calculated void effect at $T_{fuel} = 1474K$ represents $\sim 68\%$ of the total effect at this temperature. At $T_{fuel} = 2974K$, only 55% of the total effect is captured. The results for voiding effects on reactivity are even less satisfying with the SP3 transport description as only 61% and 46% of the total effects of on reactivity are captured at $T_{fuel} = 1474K$ and $T_{fuel} = 2974K$ respectively. Figure 3.8 reveals a systematic over estimation of fission rates in the C1 fuel area and an under estimation of fission rates in the C2 fuel area. It can also be noticed that relative errors on fission rates increase in the presence of voided regions. This is made more apparent when looking at figure 3.9 in which the relative difference between SCRAP and T4 rates is plotted as a function of a traverse radial position, on each 10 cm fuel slice. This effect can be assumed to be due to a misrepresentation of the radial reflectors. Indeed, it seems that the latter do not reflect enough neutrons towards the fissile part of the core. This view also reveals that in the voided configurations, the fission rates in the lower part of the core, slices $h = 1, 2, 3, 4$ (blue, orange, green and red) are even more overestimated than for the NOM and DOP configurations, reaching up to almost $\sim 2\%$

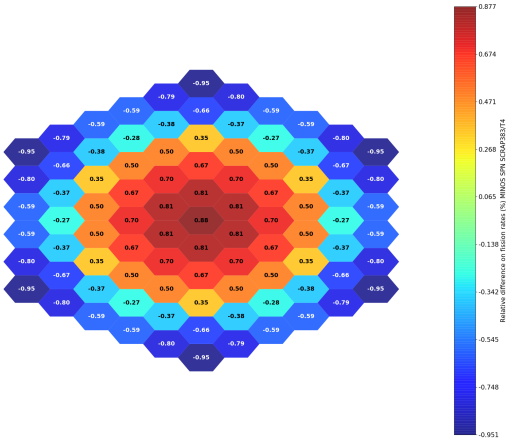

(a) *Relative error on fission rates, NOM configuration.*

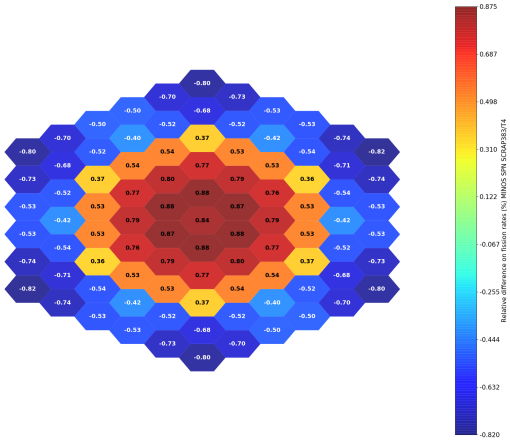

(b) *Relative error on fission rates, VOID configuration.*

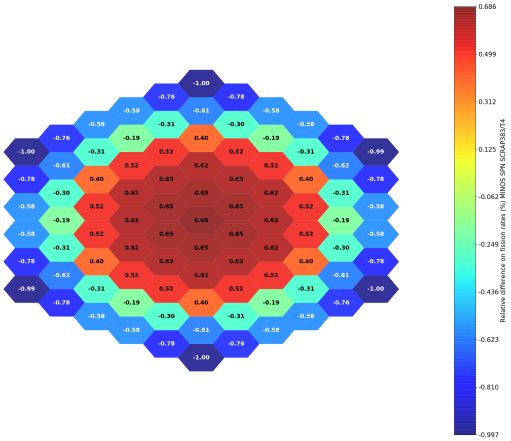

(c) *Relative error on fission rates, DOP configuration.*

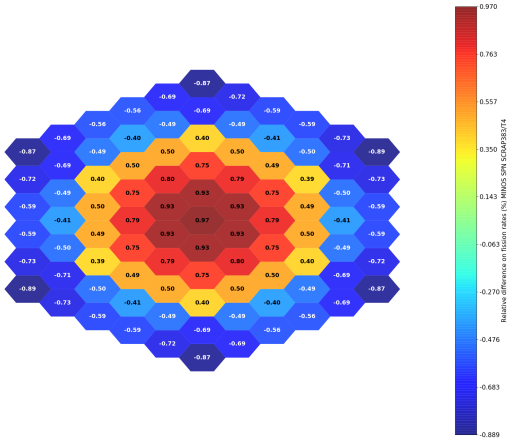

(d) *Relative error on fission rates, DOP+VOID configuration.*

Figure 3.11 Relative difference (%) AP3-T4 on fission rates obtained from SCRAP in SP_3 MINOS calculations. Nominal (a), voided (b), Doppler (c) and Doppler + voided (d) configurations.

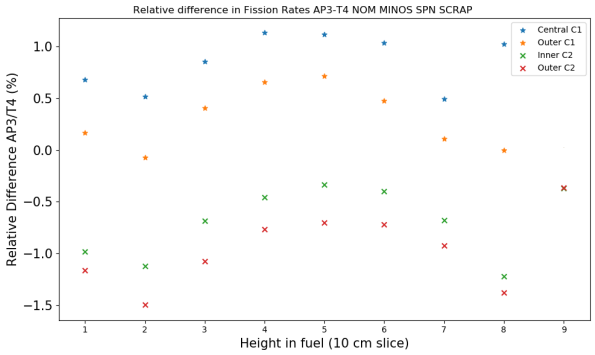

(a) *Relative error on fission rates, NOM configuration.*

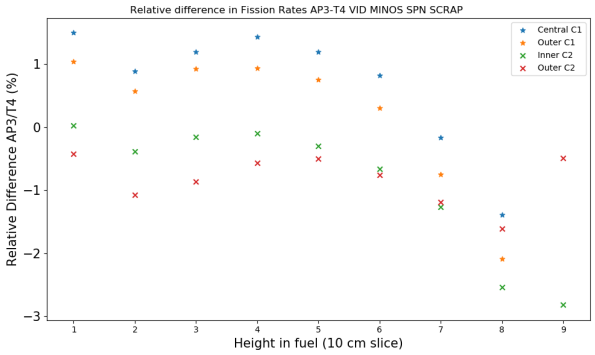

(b) *Relative error on fission rates, VOID configuration.*

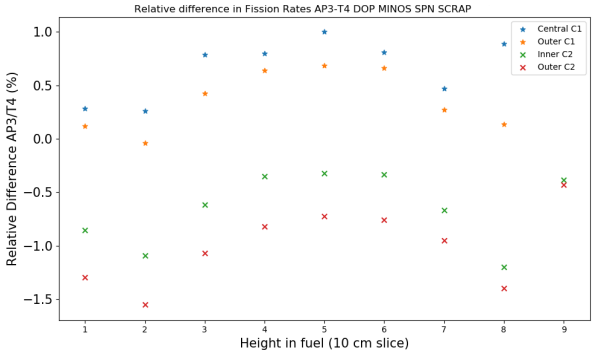

(c) *Relative error on fission rates, DOP configuration.*

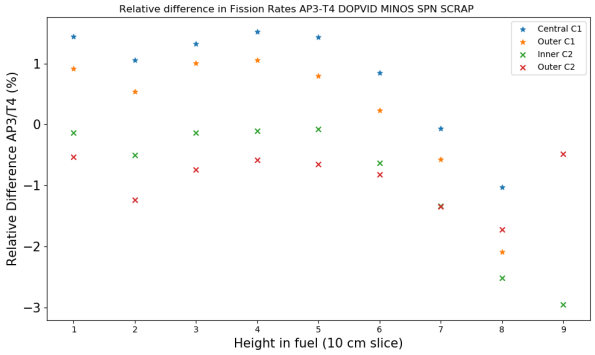

(d) *Relative error on fission rates, DOP+VOID configuration.*

Figure 3.12 Relative difference (%) AP3-T4 on fission rates obtained from SCRAP SP_3 vs axial position (10 cm slice). Nominal (a), voided (b), Doppler (c) and Doppler+voided (d) configurations. Axial traverse on C1 central and outer assemblies, C2 inner and outer assemblies.

over estimation in the core's central part. On the other hand, in the upper part of the core, the fission rates in slice $h = 7, 8, 9$ (yellow, gray and pink) tend to now be under estimated by about 2%, with minimal values reaching up to almost 4% underestimation.

These effects can be further illustrated by figure 3.10 which show the relative error's evolution for four selected assemblies, as a function of the height in fuel sub-assembly. The consistent overestimation of the fission rates in inner C1 fuel regions can be seen looking at the blue and orange data points. On the other hand green and red data points show the underestimation of rates in C2 assemblies. Furthermore, figure 3.10 suggests the need for a better representation of axial reflectors. Indeed, in all four configurations, the lower reflectors' impact on fission rates can be seen as all four graphs display a consistent increase in the relative error's value between slices 2 and 1, breaking the apparent trend of error evolution in the core's inner part. Comparable behavior can also be witnessed between slice 7 and 8 in C1 fuel as well as slices 8 and 9 for the C2 region, in NOM and DOP configurations. In the presence of a voided plenum, it can be seen that all of the fission rates tend to be underestimated for regions at the interface. The inner C2 fuel sub-assembly at $h = 9$ is where the maximal underestimation (almost -4%) is reached. This is assumed to be because this inner C2 sub-assembly shares more interfaces with the voided sodium plenum than any of the other fuel sub-assemblies. Indeed, C1 fuel and outer C2 only share their upper face with plenum, whereas the top inner C2 sub-assembly also shares interfaces with sodium plenum located above C1 fuel. This type of bias could be due to the axial reflector model used.

The results obtained from SP_3 calculations tend to confirm the biases picked up from the diffusion approximation. Despite providing a better description at the fission rates scale, as revealed in figures 3.11, SP_3 calculations with SCRAP cross sections do not provide a satisfying estimation of the void effect on reactivity. Indeed, as seen in table 3.8, MINOS SP_3 gives a worse prediction of the void effect on reactivity than the diffusion approximation. This is assumed to be due to compensating effects introduced via the diffusion approximations. This tends to confirm that the SCRAP scheme's axial leakage representation is not sufficient to properly represent the voided configuration. This can be further seen in as the evolution of biases associated with fission rates along the axial traverses presented in figure 3.12 appears to display similar behaviors in terms of biases associated with radial and axial representations.

This analysis reveals that SCRAP results are satisfying when it comes to the description of the Doppler effect on reactivity. However, the misrepresentation of voided configurations should be investigated. In order to explore possible biases associated with the SCRAP scheme's hypotheses, a MOC based scheme is presented in the following section.

3.5 A SCRAP extension : MOC2DHom

As presented in the previous sections, SCRAP performances are limited in the presence of voided regions in the case of a LOCA. In order to test hypotheses associated with SCRAP, a MOC scheme using the exact 2D sub-assembly geometries is implemented. The main hypotheses associated with the SCRAP approach to over-critical sub-assemblies' computations were the following :

1. Flux in fuel sub-assemblies can be computed directly on a homogenized geometry : radial homogeneity is assumed.
2. Neutron leakage can be computed form the *homogeneous* B1 leakage model.
3. Flux calculations in sub-critical zones can be performed through a source calculation using leakage terms.

In order to test the first hypothesis, a more standard scheme was adapted from SCRAP. This new scheme will be referred to as MOC2DHom. The differences between MOC2DHom and SCRAP are that the main flux calculation is performed on the exact 2D assembly geometry, using the TDT/MOC solver. The order of anisotropy considered is set to 3 and the fine 1760 groups energy mesh is used. The rest of the scheme's architecture remains the same : the leakage model used is the B1 homogeneous model and the homogenization/condensation step is performed with the Flux-Volume method. The treatment of the sub-critical sub-assemblies is similar, the leakage terms obtained are used as sources for MOC flux calculations.

The tracking parameters used for the collision probability method involved in the Tone self-shielding step are the same as in SCRAP. The TDT/MOC tracking consists of twenty-four horizontal and three vertical angles. An integration step of 0.04 cm is chosen. Since the Doppler effect on reactivity seems properly captured by SCRAP, even between misrepresented VOID and DOP+VOID configurations, the MOC2DHom scheme will be presented only for NOM and VOID core configuration.

The MOC calculation step is performed on the unstructured mesh obtained from the same INCA generated geometries. Specular reflection conditions are applied as an infinite lattice of fuel assemblies is considered for the initial flux calculation. Making use of the symmetries, $\frac{1}{12}^{th}$ geometries are used to perform these calculations. The latter can be found represented in figure 3.6.

The K_{inf} are obtained through the TDT/MOC solver without a leakage model, they are presented in table 3.9. The corresponding $\Delta\rho_V$ and $\Delta\rho_D$ are computed and compared to

the reference T4 void and Doppler effects in tables 3.10 and 3.11. It is worth noting that the times presented in table 3.9 are those required to treat both C1 and C2 assemblies in an infinite lattice, without applying a leakage model. Time to run the MOC2DHom scheme for the 7 sub-assemblies is shown in table 3.12.

		AP3 No Leakage				T4	
t (s)	Config.	K_{inf} TDT		$\Delta\rho$ AP3 / T4 (pcm)		$K_{inf} \pm 5$ pcm	
		C1	C2	C1	C2	C1	C2
208	NOM	1,20796	1,28952	34	37	1,20746	1,28890
140	VOID	1,24768	1,33219	7	5	1,24757	1,33211
206	DOP	1,19840	1,28081	39	30	1,19784	1,28032
200	DOPVOID	1,24026	1,32544	1	5	1,24024	1,32536

Table 3.9 Calculated K_{inf} for C1 and C2 fuel assemblies, difference in reactivity between AP3 TDT/MOC and T4, 1760 energy groups mesh.

	T=1474K		T=2974K	
	$\Delta\rho_V$ MOC (pcm)	AP3-T4 (pcm)	$\Delta\rho_V$ MOC (pcm)	AP3-T4 (pcm)
C1	2635	-28	2816	-38
C2	2484	-33	2629	-25

Table 3.10 Comparison of voiding effects on reactivity between TDT/MOC calculations and T4 reference.

	VOID = No		VOID = Yes	
	$\Delta\rho_{DOP}$ MOC (pcm)	AP3-T4	$\Delta\rho_{DOP}$ MOC (pcm)	AP3-T4
C1	-660	5	-479	-5
C2	-527	-7	-382	0

Table 3.11 Comparison of Doppler effects on reactivity between TDT/MOC calculations and T4 reference.

Full core calculations using the MINOS solver are performed. Table 3.12 shows a comparison between MINOS diffusion and SP_3, using cross sections generated from the MOC2DHom scheme. The errors on nominal and voided eigenvalues are presented along with the calculated void effect on reactivity ($\Delta\rho_V$) and its associated bias with respect to the T4 reference. The mesh used, along with finite elements orders are the same as for the SCRAP scheme; it is shown in figure 3.7. Times and RAM usage presented for MINOS full core calculations represent the most penalizing case,

Fission rates are recovered for both NOM and VOID configuration for the diffusion transport operator. Figures 3.13 (a) and (b). Root mean squared error on rates (RMS) is computed.

MOC2DHom $t_{lattice} = 450$s RAM ~ 5.70 GiB	TRIPOLI-4 $K_{eff}\pm 8$pcm	$\Delta\rho$ (pcm) MINOS Diffusion	$\Delta\rho$ (pcm) MINOS SP3
NOM VID	1.01518 1.00752	244 478	528 875
$\Delta\rho_V$ (pcm)	-749	-514	-403
Error $\Delta\rho_V$ (pcm)	0	235	346
t_{core} (s)	403 670	212	1318
RAM, core calculation	Not recorded	3.82 GiB	21.55 GiB

Table 3.12 MINOS results, cross sections from the MOC2DHom scheme. Error on reactivity along with void effect and its associated error are shown.

For the nominal configuration, the associated error $RMS_{NOM} = 0.67\%$ whereas for the voided case, it increases to $RMS_{VOID} = 0.78\%$. Looking at biases on the void effects, 235 pcm for diffusion, and 346 pcm for SP_3, it can be said that the switch to a MOC scheme was not conclusive to improve the voided configuration's representation.

It can be noted that the MOC's addition improved errors on fission rates, as seen comparing the RMS and relative errors on fission rates from SCRAP (fig. 3.8 and 3.11) with those obtained with the MOC2DHom scheme.

Figure 3.14 shows the evolution of the relative error on fission rates as a function of height in the fuel assemblies. A similar evolution as in the SCRAP case can be seen. In the VOID case, a tendency of over estimating rates close to the lower reflector/fuel interface can be seen, and a consistent under estimation of rates close to the upper plenum/fuel interface can also be observed. This is assumed to be related to a misrepresentation of axial effects, which could be due to a combinations of the *leakage* and axial *reflector models* hypotheses.

It can be concluded from the MOC2DHom study that the homogeneity of fissile assemblies hypothesis made in SCRAP is not the limiting hypothesis. Indeed, surprisingly good results for effects on reactivity are obtained at the SCRAP lattice step, as well as a satisfying description of NOM and DOP configurations, especially in terms of the Doppler effect on reactivity. However, SCRAP does not seem suited for treating the ANTOINID's voided configurations since consistent biases on the sodium void effect seem to indicate a misrepresentation of the axial effects associated in the ANTOINID's voided configurations. This is supported by the fact that similar tendencies are observed in the MOC2DHom study. It is hypothesized that the homogeneous leakage model, with a Flux-Volume condensation, used in both schemes is not sufficient to represent such effects. It can be concluded from the SCRAP and MOC2DHom studies that both schemes are reliable in terms of their implementation, as seen

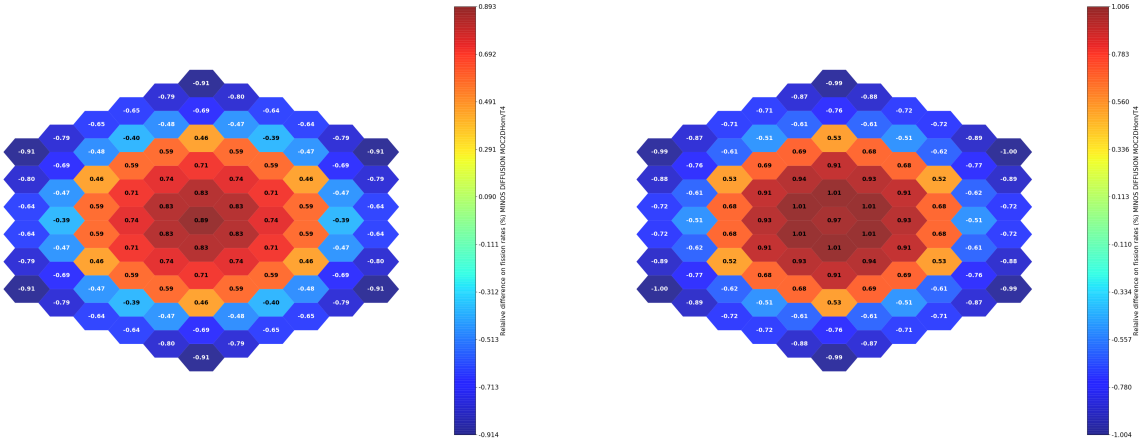

(a) *Relative error on fission rates, NOM configuration.*

(b) *Relative error on fission rates, VOID configuration.*

Figure 3.13 Relative difference (%) AP3-T4 on fission rates obtained from diffusion calculations in MINOS, from MOC2DHom cross sections. Nominal (left) and voided (right) configurations.

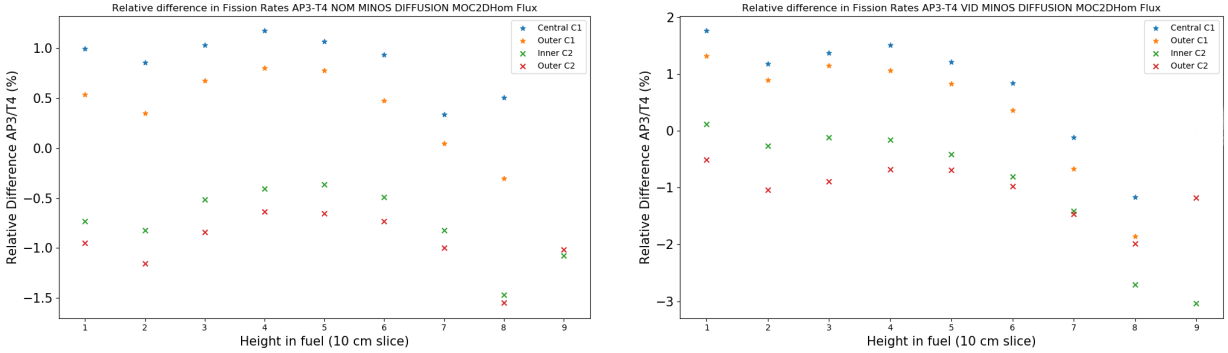

(a) *Relative error on fission rates, NOM configuration.*

(b) *Relative error on fission rates, VOID configuration.*

Figure 3.14 Relative error on fission rates on axial traverse, rates integrated over 10cm fuel slices, MINOS diffusion with XS from MOC2Hom - T4. Axial traverse on central and outer C1, inner and outer C2.

from infinite lattice calculations, and satisfactory fission rates. However, the biases due to the use of the homogeneous leakage model dominate as the desired precision on the sodium void effect is not reached.

In order to tackle this problem, important modifications to the lattice scheme are required. Three schemes aiming at a better description of axial streaming effects in voided regions are presented in the next Chapter. These are aimed at testing the two remaining *leakage* and *reflector model* hypotheses. It can be noted that, although it has been concluded that the *homogeneity* hypothesis is not the limiting factor, a MOC calculation will become necessary when introducing *heterogeneous* leakage in more advanced schemes.

CHAPTER 4 TREATMENT OF VOIDED CONFIGURATIONS: EXPLORING DIFFERENT SOLUTIONS

This chapter aims at presenting some of APOLLO3's possibilities for advanced schemes. The techniques presented were developed in order to simulate voiding and axial effects, which appeared dominant in Chapter 3. Different possible solutions are explored and their performances in terms of cost/precision are compared. Possible drawbacks are identified and ideas for improvement are presented.

4.1 Attempt at defining a "best estimate" lattice scheme

SCRAP's homogeneous assumptions seem to be valid at the assembly scale in a context where neutron leakage is not considered. Indeed, its results at the lattice stage are impressive judging by the void and Doppler effects on reactivity comparison with T4. However, as seen previously in Chapter 3, full core calculation results are not satisfying when it comes to estimating the void effect on reactivity. This underestimation of the voiding effect was hypothesized to originate from an inaccurate representation of neutron leakage out of the core. Looking back at equation 2.42, underestimating the leakage term L could indeed be one of the causes for this inaccuracy. In an attempt to better describe the axial leakage and streaming effects, three new lattice schemes are proposed. Firstly, a scheme based on a B-*heterogeneous* method implemented in the 2D TDT-MOC solver is implemented. Its vocation is to test the hypothesis associated with the *leakage* model used for lattice calculations. This first scheme will be referred to as the "MOC2DHet" scheme. Secondly, a full 2D1D scheme is presented, aiming at a more accurate calculation of cross sections for the axial reflectors. This would allow to test the hypothesis made to represent reflectors in the SCRAP scheme. Thirdly, a hybrid 2D1D scheme is presented, which combines the 2D1D axial representation with a similar fissile sub-assembly treatment as in the MOC2DHet scheme. It is worth noting that the 2D1D approach is "exploratory", its use in this work will serve as an assessment of its current capabilities. Sources of errors may vary from the lack of experience on optimized solver parameters, to potentially unstable implementations as 2D1D is not part of the non-regression tests for APOLLO3. All results related to the 2D1D method will thus have to be analyzed carefully. The three additional schemes introduced will be tested for cross section generation through their use in core calculations.

In a "best estimate" approach, the MINARET [13] solver is selected to treat the full core problem. MINARET results are presented for the three lattice schemes. The transport operator's

influence is then considered : for a given lattice scheme, MINARET, NYMO and MINOS (diffusion and SP_3) solvers are confronted. Performances in terms of computational time and RAM usage are assessed. Conclusions about the hypotheses associated with *leakage* and *reflector* models are formulated. Lastly, a brief analysis of the full core solvers' performances in a precision/cost approach is presented.

4.1.1 The "MOC2DHet" lattice scheme

The proposed 2D MOC lattice scheme keeps the SCRAP philosophy in the sense that fissile sub-assemblies are treated first, a leakage model is applied, and source calculations are performed for plenum and reflector sub-assemblies. The leakage term from C1 assembly is used as a source for the lower reflector under C1 as well as the plenum above C1. On the other hand, the leakage term from C2 assembly is taken as the source for the radial and lower reflectors as well as plenum above C2. The assembly flux calculations are performed using the MOC on a 1760 groups energy mesh. MOC calculations are performed on the exact unstructured heterogeneous geometry. This allows for the introduction of a B-heterogeneous leakage model and homogenization/condensation of fissile sub-assemblies by the Flux-Moments method implemented in APOLLO3 [28]. It is worth noting that the Flux-Moments homogenization was attempted for sub-critical assemblies. However, in this case where sub-critical motifs are treated separately through a source calculation, a Flux-Volume condensation seems to be preferable. Indeed, when the Flux-Moments method was tested for homogenizing sub-critical assemblies' cross sections, it was observed that full core MINARET calculations did not converge in voided configurations. This is assumed to be due to the fact that the current vector, whose components are the flux moments with odd orders, tends to go to zero over the totally homogenized sub-critical assemblies [31]. This is due to the fact that the Flux-Moments method requires a complex expression for the flux, as obtained when using the B-heterogeneous model [29]. However, the source calculations performed to treat the sub-critical assemblies only provide a purely real flux solution, the homogenization is then attempted using the (real) moments of the flux. This leads the current to cancel out after the complete homogenization of the sub-assembly.

The B-heterogeneous leakage model allows taking into account preferred leakage directions. In the ANTOINID case, it appears that the main direction for neutron leakage is along the axially voided regions. For this reason the buckling vector is taken to have a single component, in the $\hat{z}$ direction. In order to further capture the anisotropic behavior in the case of voided conditions, the anisotropy order considered for scattering events is set to 3. In an effort to reduce the computational cost, the hexagonal symmetries of assemblies is used. This

allows for the treatment of $1/12^{th}$ of each assembly. Specular reflection boundary conditions are applied in order to work on an equivalent infinite lattice. Three types of unstructured geometries are considered. Indeed, C1 and C2 share the same geometry, the three types of reflectors are also described by the same 2D mesh, and the two types of plenums as well. The geometries, and zone assignment properties are the same as the ones presented in Chapter 3, they can be seen in figures 3.6.

Two types of *tracking* are generated over the geometries, the first is associated with the TDT/CPM solver [16] and used to perform a quick P_{ij} calculation as part of Tone's self-shielding method [24]. It involves twelve horizontal angles, three vertical angles as well as a transversal integration step set to 0.1 cm. The second one is associated with the TDT/MOC solver, it uses twenty-four horizontal angles, four vertical angles and a transversal integration step of 0.04 cm. These tracking parameters were selected as they were recommended by P. Archier et. al. [21] defining the AP3 reference scheme for SFRs.

The times required to run the entire MOC2DHet scheme (also applying the B-heterogeneous model to fissile assemblies and performing source calculations for sub-critical assemblies) are 1740s and 2228s for the NOM and VOID configurations respectively. Each of which requires a bit more than 8 GiB of RAM. During these ∼2000s, 100 are taken to perform the zone assignment step on the three geometries treated (fuel, reflector, plenum). 10s are spent in the self-shielding module, 800s are spend in the TDT/MOC flux solver. About 25 seconds are necessary to perform the homogenization/condensation step and around 50 to 60 seconds are necessary for each of the five source calculations used to describe the plenum and the reflectors.

4.1.2 The "full 2D1D" lattice scheme

The "full 2D1D" scheme is based on 2D calculations performed on the exact 2D geometries on the x-y plane, coupled with an IDT/Sn 1D calculation on an equivalent homogenized geometry. The exact (1/12th) unstructured geometries for lower reflector, fuel and plenum sub-assemblies are used and specular boundary conditions are applied at the limits on the xy plane. Axial distributions are specified, for the C1 assembly case : 30, 80 and 40 cm for the lower reflector ("SREFLLOW1"), fuel ("C1") and plenum ("SPLN1"). When treating C2 assembly, the axial distribution is modified to 30, 90 and 30 cm for lower reflector ("SREFLLOW2"), C2 fuel ("C2") and plenum ("SPLN2") sub-assemblies respectively. An approached geometry involving three homogeneous slices is generated and meshed, refining the axial steps at the interfaces between materials, as well as close to the $z = 0$ and $z = 150cm$ boundaries. A vacuum boundary condition is applied at these planes. The scheme loops between the

2D MOC and 1D calculations. A flat flux is initialized on the 2D geometries, cross sections are homogenized by the Flux-Moments method to a corresponding 1D homogeneous axial traverse geometry. A 1D flux calculation is performed by the IDT solver along the three homogenized axial slices. The leakage terms out of each homogenized media are obtained by taking the difference between incoming and outgoing fluxes, giving the net current through the $z = z_{min}$ and $z = z_{max}$ interfaces. The leakage terms from the 1D calculations are then used as sources for the 2D MOC step. The cross sections for each of the media making up the exact geometries are thus updated and homogenized to perform a new axial calculation. The process is repeated until convergence is reached, setting a 10^{-5} criteria on the eigenvalue computed by the IDT solver on the 1D homogeneous geometry.

The 1760 groups cross sections on each of the three slices heterogeneous geometries are at the end homogenized to a single medium (1 per slice) and condensed to 33 energy groups. The homogenization/condensation method used is the Flux-Moments technique as it was observed to be the only available in the 2D1D approach. Table 4.1 shows the assemblies' eigenvalues obtained from the IDT 1D calculation on the equivalent homogenized geometry. The voiding effects computed at the assembly level are 275 pcm and 762 pcm for C1 and C2 assemblies respectively. This suggests a possible discrepancy from possible reference results since a reactivity loss would be expected in the voided configurations, due to the maximization of axial neutron leakage.

In order to validate these assembly calculations, setting up the equivalent TRIPOLI4 model appears necessary. C1 assembly's geometry was implemented in native TRIPOLI4, reflection conditions were applied in the radial direction, while void boundary conditions are used for the $z = 0$ and $z = 150$ cm planes. The model was tested at the very end of the internship period. Since not much time was left to make sure it was completely operational, it will not be presented here. This model is only mentioned in this work as a potential tool for future work. Hopefully, analysis of full assembly T4 models results can contribute to validate the 2D1D methods. This could be done through comparison with IDT 1D homogeneous calculations.

full 2D1D: Flux-Moments	K_{eff} NOM	# 2D↔1D iterations	K_{eff} VOID	# 2D↔1D iterations	$\Delta\rho_V$ (pcm)
C1 Assembly	1.07228	4	1.07545	7	275
C2 Assembly	1.16292	4	1.17332	10	762

Table 4.1 C1 and C2 assemblies' eigenvalues from equivalent 1D IDT calculation : full 2D1D with Flux-Moments condensation.

Details about the algorithmic implementation can be found in B. Faure's PhD thesis [11], in which the full 2D1D scheme is described extensively. The corresponding pseudo-code algorithm is "Algorithm 6" (page 95).

The full 2D1D scheme for a single assembly is completed in about 45 minutes for nominal configurations and up to 70 minutes in the voided cases. The time greatly varies depending on the choice of the tracking parameters and convergence criteria on the IDT-1D eigenvalue. In order to get the results presented, the tracking used in the MOC2DHet scheme was applied. It could be interesting to further optimize the method as this choice of tracking leads to consequent computational times. This implementation uses a maximum of about 5 GiB of RAM. The time recorded is one that was obtained by running the full 2D1D scheme on 20 CPU threads in parallel, as opposed to the 16 CPU threads used for previous SCRAP, MOC2DHom and MOC2DHet calculations.

In his thesis [11], B. Faure presents some of the issues associated with this technique. Indeed, the potential presence of negative source terms which could be introduced when axial effects take over scattering and fission contributions need to be dealt with. In order to avoid such numerical instabilities, two "fix-up" strategies were made available in APOLLO3. The "zero source fix-up" which replaces sources' negative isotropic components by zero, and leaves the higher order terms untouched. This approach is efficient at tackling the problem of negative source components, however it does not preserve neutron balance. On the other hand, the "Transverse Leakage Splitting" (TLS) technique, replaces the negative isotropic source components by equivalent corrections to the total macroscopic cross sections, thus allowing to preserve the neutron balance.

The results presented from the full 2D1D lattice step all rely on the "zero source" fix-up option. Using the TLS technique was attempted. However, it appears that this option is not available in the APOLLO3 versions used due to the code's evolutions since 2019.

Keeping in mind the fact that the full 2D1D *lattice* step has not been validated numerically by a T4 comparison, full core calculations will still be attempted and conclusions about the lattice scheme will be drawn from MINARET results analysis.

4.1.3 The "hybrid 2D1D" lattice scheme

The "hybrid 2D1D" scheme is similar to the "full 2D1D" in the sense that it is based on the same principle of performing an axial IDT calculation on equivalent homogenized axial slices. The difference is that the fissile zone is treated in the same way as it was in the "MOC2DHet" scheme. A 2D MOC calculation is thus performed and a heterogeneous B1

leakage model is applied. This differs from the full 2D1D scheme as the eigenvalue problem is now considered for the fissile sub-assembly, instead of the iterative approach using source calculations described in the previous sub-section. The cross sections for C1 and C2 sub-assemblies are computed once, homogenized using the Flux-Moments method and used as such in the 1D axial geometry. Only lower reflector and plenum sub-assemblies are then iterated over in a similar fashion as described in the full 2D1D scheme. Leakage from the 1D calculation is used as a source for 2D MOC computation of the cross sections of the sub-critical sub-assemblies.

The 1760g cross sections on the exact geometries are homogenized and condensed to 33 groups using the Flux-Moments technique, leading once again to the creation of 3 corresponding homogeneous media. The hybrid version of the 2D1D scheme is described in pseudo-code in B.Faure's thesis and referred to as "Algorithm 7" (p. 102) [11].

This hybrid version of the 2D1D MOC scheme runs in about 20 minutes, on 20 threads and uses a total of around 5 GiB of RAM. The time and memory occupation values presented correspond to the treatment of a single assembly. Similarly as in the full 2D1D case, the time indicated corresponds to the one obtained on a 20 CPU threads parallel computation.

The results obtained from the hybrid 2D1D implementation at the lattice stage are presented in table 4.2 which show the eigenvalues obtained from the IDT 1D calculations performed on the full assembly.

hybrid 2D1D: Flux-Moments	K_{eff} NOM	# 2D↔1D iterations	K_{eff} VOID	# 2D↔1D iterations	$\Delta\rho_V$ (pcm)
C1 Assembly	1.07102	2	1.07287	2	161
C2 Assembly	1.16176	2	1.17071	2	658

Table 4.2 C1 and C2 assemblies' eigenvalues from equivalent 1D IDT calculation : hybrid 2D1D with Flux-Moments condensation.

Looking at eigenvalues presented in table 4.2 reveals that positive contributions to the sodium void effect on reactivity dominate for both assemblies. This would tend to hint at the fact that these calculations could not be valid since a negative effect on reactivity is to be expected due to the maximization of leakage through the voided channels. However, it is worth noting that similar results are obtained in the "full 2D1D" case. Once again, reference Monte-Carlo simulations would be required to fully interpret these results.

4.2 Full core calculations with MINARET

Radial discretization The MINARET exact transport solver was chosen to treat full core nominal and voided configurations. In the x-y plane, hexagonal assemblies are meshed directly through the built-in mesher and are subdivided into triangular elements. Originally, the triangular elements' characteristic size was specified to 8 cm. Choosing Discontinuous Galerkin Adaptative (DGA) finite elements, the triangles' size is automatically adjusted such that each hexagon is paved by fourteen triangles. The corresponding 2D radial calculation mesh originally used is shown in figure 4.1. The choice of finite element order is increased to two for radial elements, in the hope of obtaining a finer description.

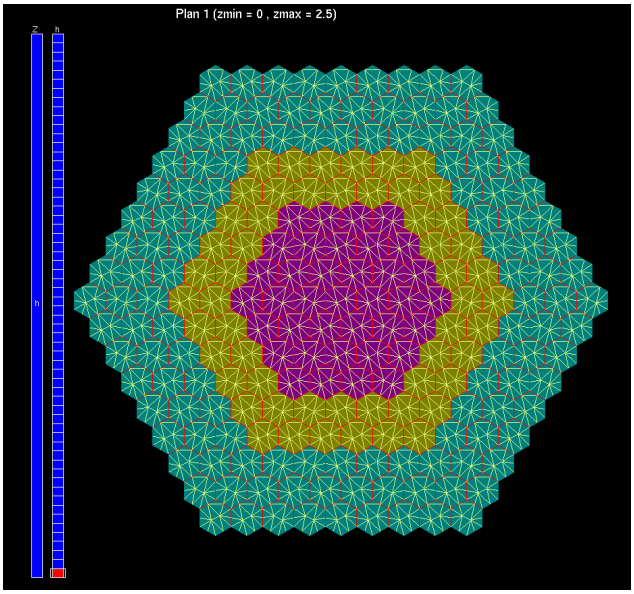

Figure 4.1 Original calculation mesh used in MINARET.

Angular quadrature choice The angular discretization is performed using a (403) hexagonal product quadrature as recommended by Fournier et al. in [18], involving 4 positive polar directions and 3 azimuthal directions per $\pi/3$ angle. This amounts for a total of 8 times 18, so 144 distinct directions on the unit sphere. The criteria for convergence are set to a precision of 2×10^{-5} on the eigenvalue, 10^{-4} on the flux and 10^{-3} on internal iterations over fission sources. The flux calculation is performed on the adapted 33 energy groups mesh used for fast spectra. The anisotropy order for scattering cross sections is set to 3, leading to a total of four scattering matrices per medium.

Axial mesh choice The axial variations of the flux are of prime importance when estimating the streaming effects in voided configurations. A sensitivity analysis is thus performed over the size and orders of axial elements. The first axial mesh considered is the same as the one used for the SCRAP scheme. Sixty 2.5 cm increments are considered along the axial direction. This mesh is tested for axial elements of orders one and two. Since initial results using the "MOC2DHet" cross sections along with the "SCRAP" axial mesh were not entirely satisfying, a finer axial mesh consisting of 120 elements with height 1.25 cm was implemented. The results are presented in table 4.3 where eigenvalues for nominal and voided calculations are presented. Voiding effects on reactivity, along with the error with respect to T4 results are displayed. Computation times and necessary RAM resources are also shown. The choice of $\Delta z = 2.5$ cm with finite elements order of 2 both radially and axially amounts to a total of 1,458,240 spatial unknowns. Switching to the fine $\Delta z = 1.25$ cm mesh with axial element order 1 takes the total number of spatial unknowns to 2,551,920. The impact of using finite elements of order 2 along with $\Delta z = 1.25$ was considered but not tested since refining the mesh or adding extra degrees of freedom did not improve the precision on the loss of coolant effect on reactivity.

Mesh Type	K_{eff} NOM	K_{eff} VOID	$\Delta\rho_V$ MINARET (pcm)	$\Delta\Delta\rho_V$ AP3-T4 (pcm)	Time(s) NOM/VOID	RAM (GiB)
$\Delta z = 2.5$ cm order 1	1.017403	1.011209	-602	147	8897/12479	18.102
$\Delta z = 2.5$ cm order 2	1.017404	1.011212	-602	147	14108/13893	20.518
$\Delta z = 1.25$ cm order 1	1.017433	1.011235	-602	147	26859/22799	35.949

Table 4.3 MOC2DHet-MINARET results for sodium void effects on reactivity : sensitivity to axial meshing and finite element order analysis.

Mesh optimization, reducing MINARET time and RAM usage The original choice for the triangular finite elements used to discretize the spatial variable on the the x-y plane was reconsidered, in an aim of optimizing the computational cost. Indeed, looking at table 4.3, it can be seen that no precision is gained by refining the axial mesh to a finer one, while the computational times and RAM usage increase drastically. A similar reasoning is applied for the radial mesh : since homogenization is performed at the assembly level, it is not necessary to describe each hexagon by 14 triangular elements. The study of results dependence on the axial meshing reveals that no real gain is made from a finer/higher order

representation. The eigenvalues change slightly, within a few pcms range, but the voiding effect on reactivity is not impacted at the pcm scale.

A final choice of finite elements calculation mesh is made. For the rest of transport calculations, hexagons are subdivided into 6 triangles, leading to regular prismatic elements with equilateral triangular bases (fig. 4.2) and a height of 2.5 cm. In order to obtain this regular radial mesh, the characteristic size of the elements was increased from 8.0 cm to 12.0. The total domain is then composed of 60 slices of 2.5 cm high prismatic elements. This amounts to a total of 546 840 spatial unknowns. The radial FEM order is kept to 2, and the axial FEM order to 1. This choice might need to be reconsidered in order to further optimize the calculation mesh.

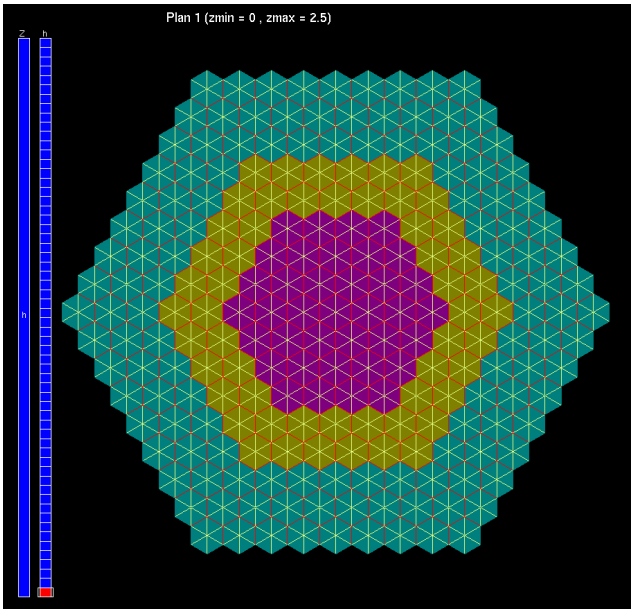

Figure 4.2 Optimized calculation mesh used in MINARET S_N calculations.

4.2.1 Calculations with cross sections from MOC2DHet

In order to assess the performances of the MOC2DHet scheme, MINARET calculations are performed on the new mesh. Eigenvalues of NOM and VOID configurations, the void's effect on reactivity and fission rates are compared to the reference TRIPOLI-4 MC calculations in table 4.4. The error associated with the void effect on reactivity is also shown. Time and RAM resources presented are now those required using the "optimized" mesh.

Fission rates from NOM and VOID configurations are extracted from binary files and post-treated. As described in the previous Chapter 3, the 3D fission rates are normalized to the

sum of fissile sub-assemblies, using equation 3.1. Figures 4.3(a) and (b) show the relative error between MOC2DHet+MINARET and T4 results on axially integrated fission rates for NOM and VOID configurations. Figures 4.4(a) and (b) provide a more detailed view of the relative error in each 10 cm fuel slice, along the radial described in figure A.1 of Appendix A. The relative errors for fission rates on axial traverses in the Central C1, outer C1, inner C2 and outer C2 sub-assemblies are shown in figure 4.5. These provide a better idea of the biases introduced from the axial reflector model.

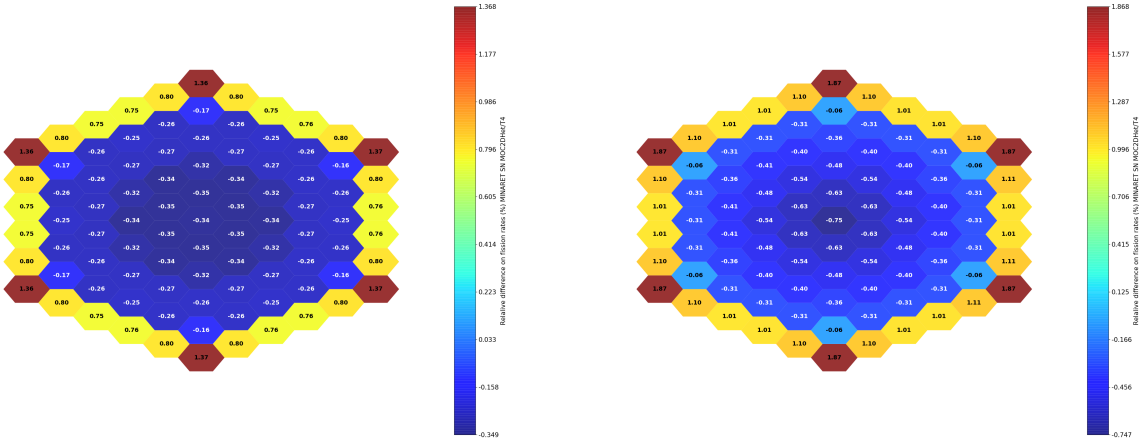

(a) *Relative error (%) on axially integrated fission rates, NOM configuration.*

(b) *Relative error (%) on axially integrated fission rates, VOID configuration.*

Figure 4.3 2D Map of relative errors on axially integrated fission rates, MINARET with XS from MOC2DHet - TRIPOLI4 reference scores, NOM (a) and VOID (b) configurations.

The MOC2DHet results appear to be satisfying in both NOM and VOID configurations. Looking at figure 4.3 (a), it can be seen that the relative error on axially integrated fission rates are around $\sim -0.30\%$ for the inner part of the fuel, even giving good results on the inner C2 fuel. Errors are maximized on the outer C2 ring, with a maximum reached for C2 sub-assemblies at the hexagonal core's vertices, showing a 1.37% overestimation of rates. This

Config.	K_{eff} MINARET	error K_{eff} MOC2DHet-T4 (pcm)	Time (s)	RAM (GiB)	Void effect (pcm)	Error on void effect (pcm)
NOM	1.01739	213	4048	4.052	-603	146
VOID	1.01118	359	4975	4.051		

Table 4.4 Full core MINARET results from MOC2DHet cross sections. K_{eff} for NOM and VOID configurations, void effect on reactivity and associated errors with respect to T4 reference.

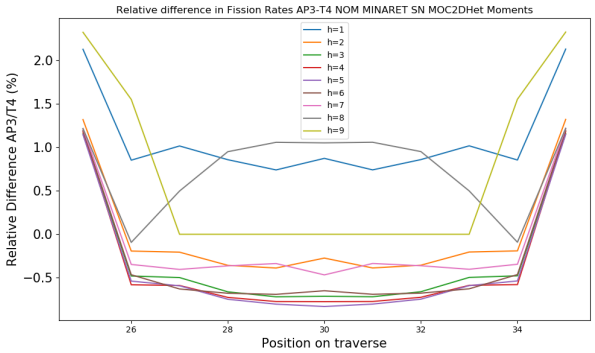

(a) *Relative error (%) on fission rates, radial traverse, NOM configuration.*

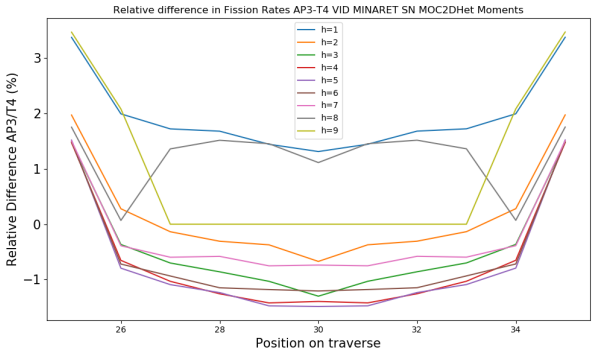

(b) *Relative error (%) on fission rates, radial traverse, VOID configuration.*

Figure 4.4 Relative error on fission rates on radial traverse, rates integrated over 10cm fuel slices, MINARET with XS from MOC2DHet - T4. Radial position expressed in ERANOS hexagons numbering.

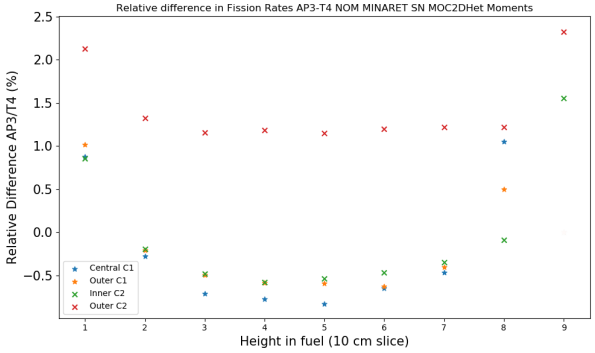

(a) *Relative error (%) on fission rates, axial traverse, NOM configuration.*

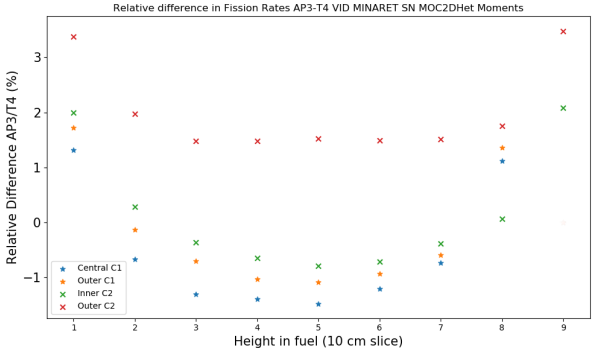

(b) *Relative error (%) on fission rates, axial traverse, VOID configuration.*

Figure 4.5 Relative error on fission rates on axial traverse, rates integrated over 10 cm fuel slices, MINARET with XS from MOC2DHet - T4. Axial traverse on central and outer C1, inner and outer C2.

is hypothesized to be due to the radial reflector's effect, which becomes even more important for sub-assemblies sharing three sides with the radial steel reflectors. The NOM case has an associated RMS error of $RMS_{NOM} = 0.58\%$. In the VOID configuration (fig. 4.3 (b)), the bias on fission rates seems to display a similar behavior, although in this case, the error's amplitude is more important as the error on central C1 sub-assembly's integrated fission rate is almost doubled, to -0.75%. The bias on C2 sub-assemblies neighboring the radial reflector now goes up to 1.87%. The RMS error associated is calculated to be $RMS_{VOID} = 0.80\%$. These biases can further be decomposed by looking at figure 4.4, providing a more detailed

description of radial and axial effects, along the reference traverse. It can be seen that in both cases, rates in outer C2 are over-estimated at all heights, which goes to reinforce the idea that this bias is introduced by the radial reflector model used. In the inner part of the fissile zone, rates are consistently underestimated $\sim -0.5\%$ for NOM and $\sim -1\%$ for VOID, except at heights $h = 1$ (blue), $h = 8$ (gray) and $h = 9$ (yellow). Indeed in the fuel slices at interfaces with axial reflectors ($h = 1$) and plenums ($h = 8, 9$), fission rates tend to be over estimated by $\sim 1 - 2\%$ for NOM and $\sim 2 - 3\%$ for VOID. This hints at the introduction of biases originating from the axial reflector model, which is accentuated by the presence of voided regions. The combination of radial and axial effects highlights the chosen reflectors model's limitations.

These effects can further be seen in figure 4.5. A clear consistent over estimation of fission rates at all heights in the outer C2 is shown, related once again to the radial reflector effect. It is worth noting that the other three (central/outer C1 and inner C2) follow similar patterns in the biases evolution. The variation of relative errors between slices 1 and 2 reveals a consistent underestimation in the flux's axial gradient and overestimation in fission rates at the interface with the lower refelctor. Similarly for slices 8 and 9, the evolution of the relative differences along the axial dimension reveals a consistent overestimation of the gradient of the flux and an overestimation of the fission rates on slices neighboring the sodium plenum.

The MOC2DHet scheme is satisfying in the sense that errors on axially integrated fission rates remain small, in the order of $\pm \sim 1\%$ in both NOM and VOID cases. Its most notable performance appears to be that the heterogeneous leakage model's introduction allows for a better treatment of axial effects in the central fuel zone. The scheme's performance on predicting the sodium void effect on reactivity is acceptable as it definitely gives a better estimate than SCRAP although the precision obtained is not totally satisfying with a smaller but persistent bias of $\Delta\Delta\rho_V = 146\ pcm$. This error still represents a 19.5% offset with respect to the target reference T4 value of $\Delta\rho_V = -749\ pcm$. Since reactivity in both VOID and NOM is over-estimated, and that in both cases :

1. Fission rates in the higher flux (central) zone are under-estimated,
2. Fission rates at the axial reflector's interfaces are consistently over estimated,

the relative over estimation of the VOID configuration's reactivity is hypothesized to be due to the axial reflector's treatment, which doesn't allow for a fully precise representation of the axial leakage effects. This would mean that in both cases, too many neutron are reflected towards the fissile part of the core so that the observed local over-estimation of fission rates is introduced. The neutron leakage would then be underestimated, leading to the consistently

witnessed overestimation of reactivity. The study of the MOC2DHet scheme reveals that it provides reliable results as description of the sodium void effect is significantly better than in the previous schemes studied. However, it must be noted that both the axial and the radial reflector models could gain from being improved. This could potentially be done through the use of a radial traverse to calculate the cross sections of the radial reflector.

It is hoped that the 2D1D variants introduce a better representation of the lower axial reflector and upper plenum. The full and hybrid 2D1D results will now be presented and confronted to those obtained using the MOC2DHet scheme.

4.2.2 Calculations with cross sections from full 2D1D

In the exploratory full 2D1D fusion approach presented, the radial reflectors' cross sections are taken to be the ones calculated from the MOC2Dhet scheme. It is thus expected for the bias introduced by the radial reflector model to remain. On the other hand, a better treatment of axial reflectors is expected.

Config.	K_{eff} MINARET	error K_{eff} full 2D1D-T4 (pcm)	Time (s)	RAM (GiB)	Void effect (pcm)	Error on void effect (pcm)
NOM	0.98771	-2740	4416	4.075	+574	1323
VOID	0.99335	-1416	4853	4.058		

Table 4.5 Full core MINARET results from full 2D1D cross sections. K_{eff} for NOM and VOID configurations, void effect on reactivity and associated errors with respect to T4 reference. Applying a Flux-Moments condensation.

Flux-Moments Condensation, Negative Sources fix up A simple look at table 4.5 reveals important biases introduced by this method. Both NOM and VOID configurations are extremely under estimated in terms of reactivity, which shows in the fission rates, presented in figure 4.6 (a)(b). It appears that in both cases, the distribution of fission rates is flatter than that of the reference T4 calculations. This leads to an underestimation in the central higher flux area, and to an overestimation in the outer radial regions, after normalization. This could explain the important underestimation of both eigenvalues computed. This kind of bias could reveal important issues in the lattice full 2D1D step as cross sections used for MINARET full core calculations presented seem to be unable to reflect the system's main physical properties. Aside from important biases on the eigenvalues themselves, table 4.5 shows that the sodium void coefficient's sign is wrongly predicted.

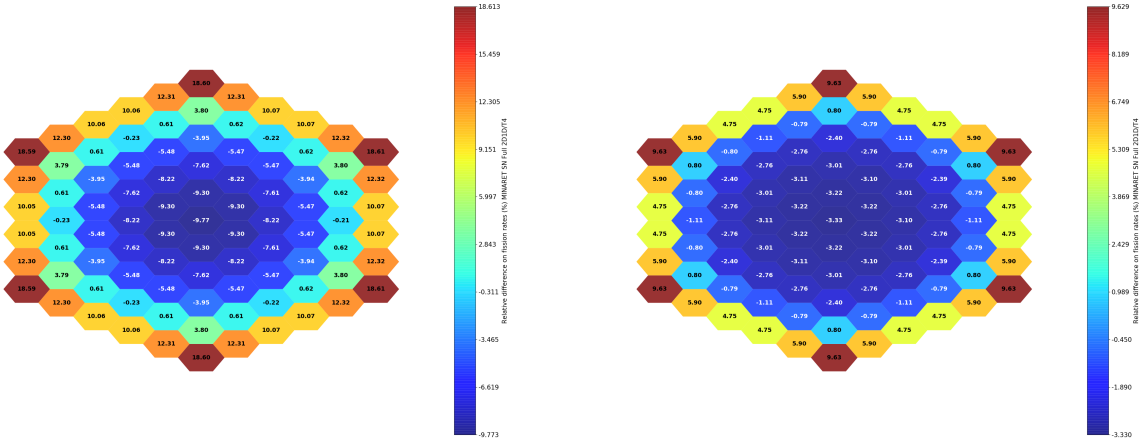

(a) *Relative error (%) on axially integrated fission rates, NOM configuration.*

(b) *Relative error (%) on axially integrated fission rates, VOID configuration.*

Figure 4.6 2D Map of relative errors on axially integrated fission rates, MINARET with XS from full 2D1D - TRIPOLI4 reference scores, NOM (a) and VOID (b) configurations. Flux-Moments condensation used.

Multiple sources of errors could be identified as it is possible that some mistakes were made in the user implementation. Impact of some specific parameters in the TDT/MOC source calculations still require some investigation as there is only a limited experience from this type of calculations in 2D1D methods.

However, it is probable that these unsatisfactory results could be due to a bug in the implementation of the full 2D1D method. Indeed, the 2D1D module not being part of APOLLO3's regression tests, it is assumed that the method could have indirectly suffered from changes in APOLLO3 since B. Faure's work (2019). In order to test this hypothesis, it could be relevant to retrieve and recompile the anterior APOLLO3 version in which the 2D1D module produced satisfying results. This was not attempted during the course of this work due to the time constraints associated with the internship at CEA.

4.2.3 Calculations with cross sections from hybrid 2D1D

Table 4.6 shows the results and performances for MINARET calculations using hybrid 2D1D generated cross sections. The scheme's performances are primarily assessed by comparing the deterministic void effect calculation with the value obtained from T4. Figure 4.7 shows the relative errors (%) on axially integrated fission rates obtained from hybrid 2D1D in MINARET. The RMS error associated with each of the configurations are $RMS_{NOM} = 0.74\%$ and $RMS_{VOID} = 0.99\%$. In order to visualize radial and axial effects, errors along the

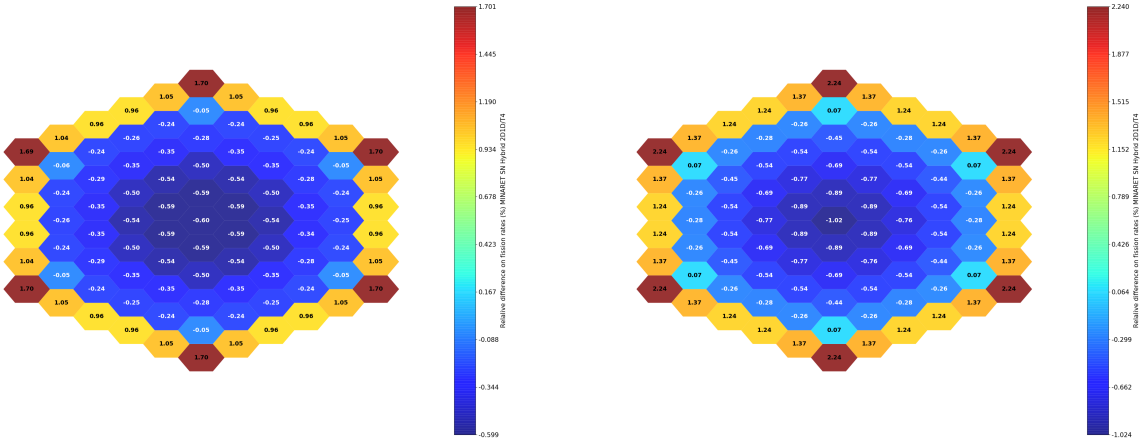

(a) *Relative error (%) on axially integrated fission rates, NOM configuration.*

(b) *Relative error (%) on axially integrated fission rates, VOID configuration.*

Figure 4.7 2D Map of relative errors on axially integrated fission rates, MINARET with XS from hybrid 2D1D - TRIPOLI4 reference scores, NOM (a) and VOID (b) configurations.

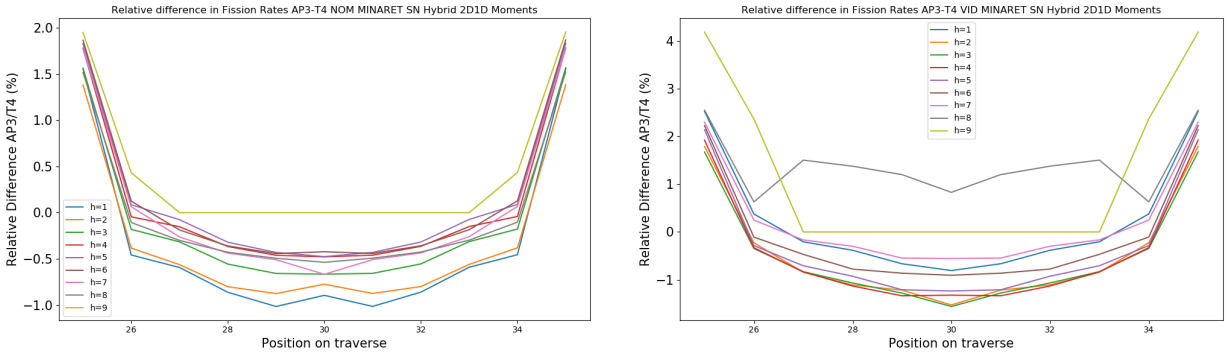

(a) *Relative error (%) on fission rates, radial traverse, NOM configuration.*

(b) *Relative error (%) on fission rates, radial traverse, VOID configuration.*

Figure 4.8 Relative error on fission rates on radial traverse, rates integrated over 10cm fuel slices, MINARET with XS from hybrid 2D1D - T4.

Config.	K_{eff} MINARET	error K_{eff} hybrid 2D1D-T4 (pcm)	Time (s)	RAM (GiB)	Void effect (pcm)	Error on void effect (pcm)
NOM	1.01573	53	4088	4.054	-549	200
VOID	1.01009	253	4390	4.056		

Table 4.6 Full core MINARET results from hybrid 2D1D cross sections. K_{eff} for NOM and VOID configurations, void effect on reactivity and associated errors with respect to T4 reference.

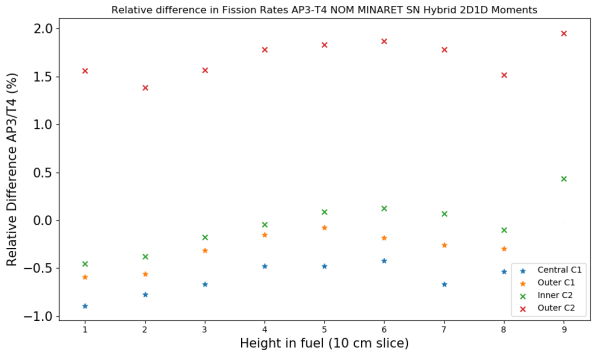

(a) *Relative error (%) on fission rates, axial traverse, NOM configuration.*

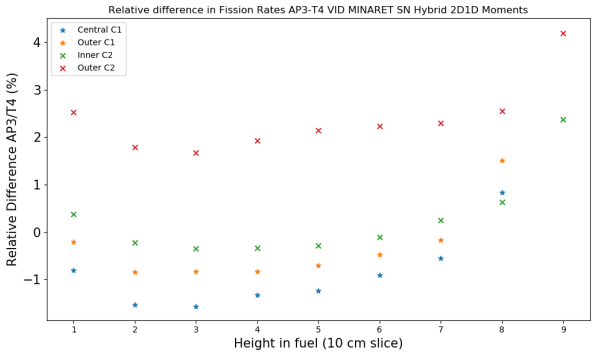

(b) *Relative error (%) on fission rates, axial traverse, VOID configuration.*

Figure 4.9 Relative error on fission rates on axial traverse, rates integrated over 10cm fuel slices, MINARET with XS from hybrid 2D1D - T4. Axial traverse on central and outer C1 assemblies, inner and outer C2 assemblies.

traverses are once again plotted in figures 4.8 and 4.9. In each of these NOM (left) and VOID (right) configurations are compared. The error on sodium void effect $\Delta\Delta\rho_V = 200$ *pcm* is not entirely satisfying as it is slightly worse than that of the MOC2DHet scheme presented earlier. Relative errors on fission rates are satisfying, displaying similar behavior as the ones obtained from the MOC2DHet scheme (fig. 4.3), with a slightly greater amplitude. The overestimation of the fission rates in the vicinity of the radial reflector ranges from 0.96% to 1.70% for NOM and from 1.24% to 2.24% for VOID. Comparing to results from the MOC2DHet scheme, similar underestimation in the inner part of the core is observed, this time with a more pronounced variation in the relative errors, reaching -0.60% and -1.02% in the central sub-assembly for NOM and VOID respectively. This tendency is confirmed by the results along the radial traverse shown in figure 4.8. A closer inspection of these shows that in the NOM configuration, all heights seem to be slightly underestimated $\sim -1.0\%$ to $\sim -0.5\%$ in the inner part of the core, which hints at a more consistent description of the axial reflectors by the hybrid 2D1D scheme, as opposed to MOC2DHet which introduced a systematic overestimation of fission rates in fuel volumes sharing interfaces with axial reflectors. In the VOID case, fission rates at $h = 8$ and $h = 9$ are again over estimated, while the other heights display similar behavior in the core's inner part ($\sim -1.5\%$ to $\sim -0.5\%$ underestimation). This could be due to the bias introduced by the voiding of sodium plenums, which introduces a more important void fraction, while the voided lower reflectors are better modeled than with the MOC2DHet scheme.

The axial model's impacts on the biases presented can further be analyzed from figure 4.9 (a) which shows that the residual's structure along the axial dimension is smoother, compared to

which obtained from MOC2DHet calculations. Indeed, the variations in relative errors close to the lower reflector's interface is almost negligible for C1 assemblies (in blue and orange), as well as for the inner C2 (in green). The outer C2 sub-assembly shows a slight decrease in the fission rates over estimation between slices 1 and 2, however, this effect represents a variation of around -0.25% which is significantly better than in the MOC2DHet case, for which this variation represented around -1%. Furthermore, looking at heights 7, 8 and 9, it can be seen that hybrid 2D1D performs better than MOC2DHet at the fuel/plenum interface. Indeed, there are no particular over-estimations of fission rates at $h = 8$ for C1 assemblies, as opposed to almost $+2\%$ with MOC2DHet (fig. 4.5 (a)). In the case of C2 assemblies, the variation in errors on fission rates introduced is around $+0.5\%$, leading to an over-estimation of fission rates on $h = 9$. This variations is assumed to be introduced by the plenum's model. Once again this is significantly better than in the case of the MOC2DHet scheme, where the variations in fission rates leading to their consistent overestimation at the fuel/plenum interface was $\sim +1.5\%$ in the nominal configuration.

In the VOID configuration (fig. 4.9 (b)), biases are made more prominent as the variation of errors on rates at the lower reflector/fuel interface is now about -0.5%. At the fuel/plenum interface, the over-estimations introduced by the plenum model are of the order of 1.5%, which is still better than in the MOC2DHet case for which they were closer to 2%. It should however be noted that radial effects on the error are accentuated in the hybrid 2D1D calculations, with the biases on outer C2 rates at $h = 9$ going up to above 4% in the more penalizing voided configuration.

Additionally, the radial effect on the over-estimation of fission rates at the reflector's interface can further be seen comparing figures 4.8 and 4.4, which show that in hybrid 2D1D, fission rates in the outer C2 ring are consistently more over-estimated than with MOC2DHet. This is assumed to be due to the fact that cross sections used for the radial reflectors are the same in both cases : the one generated from MOC2Dhet through a source calculation using the leakage term associated to C2. This analysis combined with previous MOC2DHet conclusions reveals the persistent errors introduced by the MOC2DHet reflector model. A traverse to model the radial steel reflectors should be considered, in order to generate its 33 groups cross sections with better precision.

Comparing figure 4.8 with 4.4, the impact of the voided configuration can be assessed. It can be seen that the influence of voided regions is not as important in hybrid 2D1D, as errors in fission rates in the inner part of the core do not vary as much as when using the MOC2DHet scheme. This confirms the previous analysis made on the biases along the axial traverse, suggesting a better representation of axial effects in the hybrid 2D1D method.

Overall, the hybrid 2D1D scheme brings a lot of interesting things to the table, most notably a consequently better description of the axial effects on fission rates than the MOC2DHet. These performances are obtained from the more complex axial reflector models introduced from the 2D↔1D iterative method. On the other hand, the greater biases on axially integrated fission rates as well as on the sodium void effect are hard to interpret. These could be partly introduced by the radial reflectors' model which had already been observed to introduce consequent biases in the MOC2DHet case. The more important biases on axially integrated fission rates observed in the hybrid 2D1D case could be due to the combined effects of radial and axial biases which would not compensate each others as much as in the MOC2DHet case. At best, it should introduce similar biases as the ones seen in MOC2DHet. At worst, it could be partly responsible for the overestimating of the voided configuration's reactivity, leading to a larger error on the sodium void effect. Indeed, a quick comparison of tables 4.6 and 4.4 reveals that the 2D1D does a better job at estimating both configurations' in terms of the biases on reactivity. However, relative to the nominal configuration, the voided configuration's reactivity is more over-estimated, leading to a worse performance on sodium void effect predictions. This overestimation of the voided reactivity could be partly due to the misrepresentation of radial reflectors, which seem to be reflecting too many neutrons towards the fissile zone. This could explain the accentuated bias on fission rates in the outer C2 assemblies. It would be interesting to test additional radial reflector models such as the introduction of a traversing motif through the core, or the treatment of a larger motif at the lattice step which would involve a finely meshed fuel/reflector interface. Further work is required to fully decorrelate the biases associated with the hybrid 2D1D model discussed.

4.2.4 A naive approach to the reflector model : implications for the hybrid 2D1D case.

Throughout the MOC2DHet, full 2D1D and hybrid 2D1D analysis and discussion, the radial reflector model appears as a recurrent topic, introducing biases which are hard to de-correlate from the axial reflectors' effects. One thing is certain : the schemes presented fail at accurately describing radial leakage effects. Indeed, the full 2D1D scheme is limited to considering axial effects. It makes the assumption of an infinite lattice of 2D+1D assemblies, no leakage model is used : each fuel sub-assembly in the lattice is not impacted by its neighbors on a more macroscopic scale as in a fundamental mode approximation. On the other hand, the fuel sub-assemblies' treatment through the B1 heterogeneous model both in MOC2DHet and hybrid 2D1D forces the preferred leakage direction to be taken along the z axis, once again no radial component is considered. In a naive approach, one could imagine using the 2D1D lower reflector model as a radial reflector. This was easily implemented in the ANTOINID study,

and the choice was made to study the impact of using MPOs initially generated for the lower reflector below C2 assemblies as radial reflectors. In an attempt to unify the formalism, the radial reflectors for both NOM and VOID configurations were set to be the one obtained from the hybrid 2D1D C2 assembly calculations (SREFLLOW2). This introduces different assumptions as for the MOC2DHet radial reflector calculations :

1. Leakage from C2 fuel is the only neutron source for radial reflectors.
2. At the lattice stage, axial leakage from C2 fuel to SREFLLOW2 is equivalent to radial leakage from C2 to SREFLRAD.
3. Nominal SREFLLOW2's use as a radial reflector remains valid in the VOID configuration.

This approach was implemented to test the impact of a "traverse-like" radial reflector calculation. Results shown in table 4.7 reveal a better estimation of the voiding effect on reactivity than in the original hybrid 2D1D study. Indeed, error on this effects calculation went down from 200 pcm (table 4.6) to 173 pcm here. Although the use of SREFLLOW2 as a radial reflector is probably not ideal, it goes to show that a more consistent description of the material's cross sections should be considered when using 2D1D generated MPOs at the core calculation step. This highlights the need for a more suitable radial reflector model to be studied in future work as it appears necessary in the description of relatively small cores like the ANTOINID's for which radial leakage terms are significant.

Config.	K_{eff}	Error K_{eff} Radial reflector test	Void effect (pcm)	Error void effect (pcm)
NOM	1.01404	-111	-576	173
VOID	1.00815	62		

Table 4.7 Hybrid 2D1D results for NOM and VOID calculations, errors on reactivity and void effect with a different radial reflector model.

Overall, conclusions about the hybrid 2D1D approach are harder to draw than for the two previously presented schemes. On one hand, it can be safely assumed that the treatment of the fissile zone provides a reliable description, similar to that of the MOC2DHet scheme. However, the fact that the validation of "column by column" calculations was not performed thoroughly makes it hard to conclude about the scheme's validity. Nevertheless, the method appears promising and it would be relevant to extend the tests of a new radial reflector to this scheme. This could shine some light on the scheme's performances in terms of evaluat-

ing leakage effects since a more accurate radial reflector model would help isolating biases associated with the description of axial reflector.

4.3 Comparison of the performances of the lattice schemes in MINARET

Judging by tables 4.4, 4.5 and 4.6 it appears that the lattice scheme giving a best estimate on the sodium void effect is MOC2DHet, which displays an error on the estimated void effect of $\Delta\Delta\rho_V = 146\ pcm$. This reduces the error associated with the sodium void effect on the core's reactivity by a factor of 2, comparing to SCRAP scheme results.

The 2D1D study leads to the observation that the full 2D1D scheme with Flux-Moments condensation doesn't give satisfying results. This is largely due to the fact that fission rates in both NOM and VOID are highly underestimated, by up to almost $\sim -10\%$, in the central fuel area. This could explain the important underestimation of both nominal and voided reactivities, hinting at a systematic misrepresentation of the cross sections of the fissile sub-assemblies. This is assumed to be due to source MOC calculations used in the full 2D1D scheme. This interpretation would be supported by comparison with hybrid 2D1D results, which does not display the same type of biases.

The differences between both variants of the 2D1D approach might be explained by the insufficient hindsight on the convergence of source calculations of critical configurations, with a fixed eigenvalue and potentially negative sources, in the full 2D1D approach. Indeed, this type of source calculations could require particular attention from a debugging perspective as the significant biases observed could hint at a potential instability in the method's implementation.

It is worth noting that for both full 2D1D and hybrid 2D1D full core calculations, the cross sections used for the radial reflector are issued from the MOC2DHet scheme. Since 2D1D schemes only consider leakage in the axial direction, radial reflector calculations are not easily done in this context. A more accurate representation of the core/radial reflector interface appears to be necessary. An extension of the 2D1D scheme could be considered in order to treat the radial reflectors. However, due to time constraints, it was not implemented as part of this internship.

Further work would be required to fully understand biases associated with both 2D1D variants. Validation of the latter through comparison with a Monte-Carlo reference calculation would be required. The approach followed in the rest of this work was to test if biases observed in MINARET were reproducible in other full core solvers. NYMO's P_N method along with MINOS's diffusion and SP_N are now introduced to the MOC2DHet, hybrid and full

2D1D schemes.

4.4 Extension to the NYMO P_N solver

The full core model is extended to use the P_N solver NYMO. It's introduction in AP3 during the latter stages of this internship made it possible to test spherical harmonics methods in full core calculations. For each of the lattice schemes presented, NYMO will be compared to the MINARET and MINOS solvers. The full core model's adaptation was made rather simple since NYMO can use calculation meshes built for MINARET. It was thus possible to use the mesh shown in figure 4.2 in the NYMO solver. In order to perform rapid calculations and assess the different lattice schemes performances, the order in spherical harmonics expansion is set to 3, the tolerance on the eigenvalue is set to 10^{-5} and the precision on outer iterations to 10^{-5}. Additionally, it was observed that a better convergence on rates was reached when setting the tolerance for the FEM linear system solver to 10^{-5}, instead of 10^{-4}. This choice of parameters was suggested by L. Bourhara after noticing that fission rates were not symmetrically distributed around the core's center. It can safely be concluded that this asymmetry of the fission rates was simply due to this precision criteria.

4.5 Extension to the MINOS solver

The MINOS solver is used for both diffusion and SP3 calculations. The type of finite elements used is once again Raviart-Thomas Nedelec [15]. Radial elements of order two have been tested to check if the SCRAP mesh was properly converged, it appears that there is no differences beyond the pcm precision between radial elements of order 2 and those of order one previously presented. In a logic of resource optimization it thus appears relevant to limit both axial and radial elements orders to 1. The axial discretization is equivalent to the one used in the SCRAP scheme, with a total of sixty nodes, each spaced by 2.5 cm. The axial hexagonal mesh is once again split into a sub-mesh composed of trapezes. The mesh used for the subsequent MINOS calculations is the exact same as the one presented in the SCRAP context. It is shown in figure 3.7. Full core calculations are performed in the NOM and VOID configurations in both diffusion and SP3 approximations. For each of the lattice schemes presented, MINOS performances will be compared to those of MINARET and NYMO solvers.

4.6 Comparison of Lattice/Solver combinations

Throughout this work a total of five lattice schemes have been presented. The initial SCRAP approach was discussed in Chapter 3, along with its extended version, the MOC2DHom scheme. An upgraded version, the MOC2DHet scheme based on the same architecture was then presented earlier in this chapter. The 2D1D based schemes were also introduced, their performances and biases have been discussed. As of now, the MOC2DHet and 2D1D lattice schemes' performances have been assessed through analysis of MINARET transport calculations. The NYMO full core solver is introduced as an additional example of a reference transport solver. SCRAP and MOC2DHom cross sections are also used in MINARET and NYMO solvers. Additionally, the performances of the MOC2DHet, full and hybrid 2D1D schemes in MINOS (diffusion and SP_3) are compared to those of exact transport solvers. In doing so, every possible combination of lattice scheme and full core solver presented was tested.

A summary of the performances for each of the lattice schemes introduced is presented. The SCRAP, MOC2DHom, MOC2DHet, hybrid and full 2D1D schemes are confronted in tables 4.8, 4.9, 4.10, 4.11 and 4.12 respectively. For each of these, the time to treat the seven sub-assemblies (C1, C2, SREFLRAD, SREFLLOW1, SREFLLOW2, SPLN1 and SPLN2) and RAM (GiB) usage for the lattice step are shown. The errors on eigenvalues for the NOM and VOID configurations are presented as well as the associated void effect (pcm). The error (pcm) on the sodium void effect with respect to the T4 reference value is also shown. The performances of the full core solvers are also introduced through the time spent in the full core step and the RAM required. Times and memory usage presented correspond to the most penalizing configuration (generally VOID).

SCRAP $t_{lattice} = 330$ s $RAM_{lattice} \sim 4.1$ GiB	TRIPOLI-4 K_{eff}±8 pcm	$\Delta\rho$ (pcm) MINOS Diffusion	$\Delta\rho$ (pcm) MINOS SP_3	$\Delta\rho$ (pcm) MINARET S_N	$\Delta\rho$ (pcm) NYMO P_3
NOM VOID	1.01518 1.00752	-118 122	63 377	100 511	87 493
$\Delta\rho_V$ (pcm)	-749	-509	-436	-337	-343
Error on $\Delta\rho_V$ (pcm)	0	240	313	412	406
t_{core} (s)	403 670	174	580	3510	1206
RAM_{core} GiB	Not recorded	3.80	14.88	2.020	4.106

Table 4.8 Comparative results for SCRAP : MINOS, MINARET and NYMO performances at estimating sodium void effect.

MOC2DHom $t_{lattice} = 450$ s $RAM_{lattice} \sim 5.70$ GiB	TRIPOLI-4 K_{eff}±8 pcm	$\Delta\rho$ (pcm) MINOS Diffusion	$\Delta\rho$ (pcm) MINOS SP_3	$\Delta\rho$ (pcm) MINARET S_N	$\Delta\rho$ (pcm) NYMO P_3
NOM VOID	1.01518 1.00752	244 478	528 875	571 1017	556 886
$\Delta\rho_V$ (pcm)	-749	-514	-403	-303	-309
Error on $\Delta\rho_V$ (pcm)	0	235	346	446	440
t_{core} (s)	403 670	252	1319	4648	2419
RAM_{core} GiB	Not recorded	3.80	21.58	4.05	4.20

Table 4.9 Comparative results for MOC2DHom : MINOS, MINARET and NYMO performances at estimating sodium void effect.

MOC2DHet $t_{lattice} = 2230$ s $RAM_{lattice} \sim 10$ GiB	TRIPOLI-4 K_{eff}±8 pcm	$\Delta\rho$ (pcm) MINOS Diffusion	$\Delta\rho$ (pcm) MINOS SP_3	$\Delta\rho$ (pcm) MINARET S_N	$\Delta\rho$ (pcm) NYMO P_3
NOM VOID	1.01518 1.00752	-20 -93	170 211	213 360	198 338
$\Delta\rho_V$ (pcm)	-749	-821	-708	-603	-609
Error on $\Delta\rho_V$ (pcm)	0	-72	41	146	140
t_{core} (s)	403 670	455.9	1552	4975	2177
RAM_{core} GiB	Not recorded	3.81	21.55	4.05	4.25

Table 4.10 Comparative results for MOC2DHet : MINOS, MINARET and NYMO performances at estimating sodium void effect.

hybrid 2D1D $t_{lattice} = 2400$ s $RAM_{lattice} \sim 10$ GiB	TRIPOLI-4 K_{eff}±8 pcm	$\Delta\rho$ (pcm) MINOS Diffusion	$\Delta\rho$ (pcm) MINOS SP_3	$\Delta\rho$ (pcm) MINARET S_N	$\Delta\rho$ (pcm) NYMO P_3
NOM VOID	1.01518 1.00752	-282 -211	12 119	53 253	38 232
$\Delta\rho_V$ (pcm)	-749	-771	-642	-549	-555
Error on $\Delta\rho_V$ (pcm)	0	-22	107	200	194
t_{core} (s)	403 670	588	1197	4390	1268
RAM_{core} GiB	Not recorded	8.75	21.92	4.06	4.23

Table 4.11 Comparative results for hybrid 2D1D : MINOS, MINARET and NYMO performances at estimating sodium void effect.

The extension to the MINOS solver revealed that order 2 radial FEM were not necessary as it was observed that adding additional degrees of freedom allowed only for a $\sim 1pcm$ improvement on the voiding effects, to the cost of a significantly longer time. This also allowed for an important reduction the RAM required for the SP_3 technique as all angular

full 2D1D $t_{lattice} = 5700$ s $RAM_{lattice} \sim 10$ GiB	TRIPOLI-4 K_{eff}±8 pcm	$\Delta\rho$ (pcm) MINOS Diffusion	$\Delta\rho$ (pcm) MINOS SP_3	$\Delta\rho$ (pcm) MINARET S_N	$\Delta\rho$ (pcm) NYMO P_3
NOM VOID	1.01518 1.00752	-2852 -1911	-2910 -1636	-2740 -1416	-2747 -1417
$\Delta\rho_V$ (pcm)	-749	193	525	574	568
Error on $\Delta\rho_V$ (pcm)	0	942	1274	1323	1317
t_{core} (s)	403 670	225	1432	4771	2630
RAM_{core} GiB	Not recorded	3.81	15.77	4.05	4.14

Table 4.12 Comparative results for full 2D1D (Flux-Moments condensations) : MINOS, MINARET and NYMO performances at estimating sodium void effect.

fluxes are kept in memory during the computation. It was observed that switching from radial elements of order 2 to 1 reduced the RAM usage from $\sim$ 53 GiB to $\sim$ 22 GiB. This could suggest that a similar convergence study should be undertaken for the MINARET/NYMO radial mesh as calculation time gains could be made in doing so. It can be observed from tables 4.8, 4.9, 4.10, 4.11 that :

1. The biases associated with MINARET and NYMO *exact* transport solvers are similar when using the same XS.

2. The biases associated with MINOS Diffusion and SP_3 are consistently smaller than those from transport solvers.

3. MINARET and NYMO tend to over estimate reactivity for all lattice schemes, particularly in voided configurations.

4. The error on $\Delta\rho_V$ tends to be positive, underestimating the effect's amplitude, except in diffusion calculations with MOC2DHet and hybrid 2D1D schemes.

5. The full 2D1D results are unsatisfying with abnormal underestimations of both configurations : further work is required to validate and stabilize this method. The presence of a bug in the implementation cannot be excluded.

6. MINOS diffusion and SP_3 approximations give surprisingly good results when using the MOC2DHet and hybrid 2D1D schemes.

Some comments can also be made about the differences introduced from one solver to the other. It can be seen that NYMO obtained void effects all show a 6 pcm shift when comparing with MINARET results. Furthermore, the voiding effects from the first four schemes display

similar behaviors when switching from MINARET or NYMO to MINOS Diffusion or SP_3. It can be seen that the difference between exact transport calculations and diffusion calculations is about 200 pcm. Similarly, the offset between MINARET/NYMO and SP_3 void effects is around 90 pcm. This suggests that the two MINOS approximations introduce close to constant, reproducible differences in reactivity when comparing to the transport solvers.

In order to put these performances on macroscopic effects on reactivity into perspective, a smaller scale comparison of the best performing combinations of lattice scheme/solvers is proposed. Results from NYMO and MINOS calculations using MOC2DHet cross sections are presented. The latter are compared to those obtained from hybrid 2D1D cross sections, which give the second best estimate on void effects from exact transport solvers. It can also be noticed that error on $\Delta\rho_V$ from diffusion calculations with hybrid 2D1D cross sections is the best in terms of absolute difference with the reference T4 value.

4.6.1 MOC2DHet results with NYMO and MINOS

NYMO P_3 with MOC2DHet cross sections Figures 4.10 (a) and (b) present the relative errors on fission rates obtained from NYMO calculations. The associated RMS errors are 0.64% and 0.84% for the NOM and VID configurations respectively. These are comparable, yet slightly less satisfying than the ones obtained from MINARET calculations with MOC2DHet cross sections. Such discrepancies could be due to parameters chosen for the NYMO solver. Indeed, comparison with symmetric T4 rates reveals the slightly asymmetric nature of the two dimensional rates field. Restraining NYMO's convergence parameters further was found to improve this asymmetric effect, in particular the FEM linear system tolerance factor. This hints at the fact that NYMO's parameters could probably still further be optimized, making it an interesting competitor to MINARET, since it seems to provide similar results in a consequently smaller amount of time.

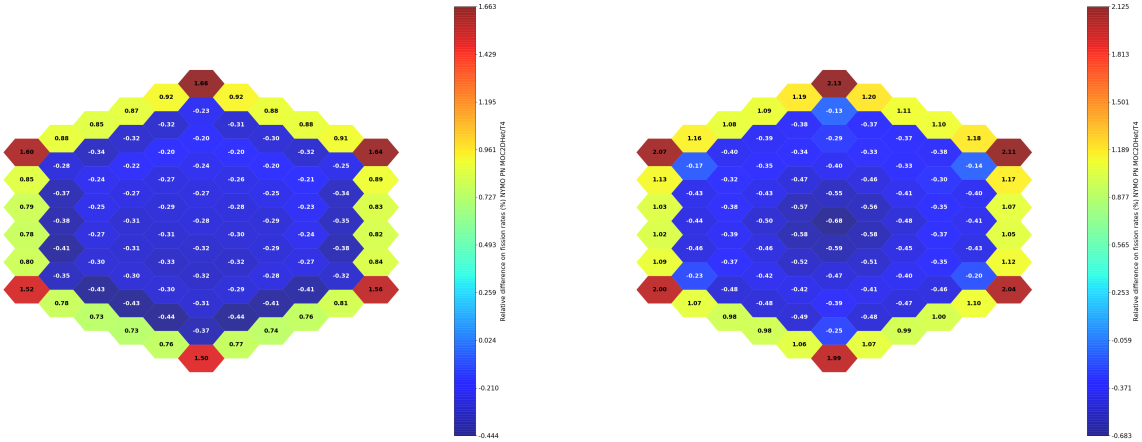

(a) *Relative error (%) on axially integrated fission rates, NOM configuration.*

(b) *Relative error (%) on axially integrated fission rates, VOID configuration.*

Figure 4.10 2D Map of relative errors on axially integrated fission rates, NYMO with XS from MOC2DHet - TRIPOLI4 reference scores, NOM (a) and VOID (b) configurations.

Axial distribution of errors on fission rates in both nominal and voided configurations are presented in figures 4.11 (a) and (b). The latter display a similar behavior as errors obtained from MOC2DHet with MINARET (fig. 4.5). This tends to confirm the interpretation made from the MINARET results analysis : the hypothesis made about the *reflector models* representation induces reproducible trends in the errors. The overestimation of rates at both axial reflector's interfaces with fuel regions is also observed in the NYMO case. Similarly, the outer C2 rates can be seen to be consistently overestimated, confirming a similar impact of the radial reflector at its interface with outermost fuel assemblies. This shows that the

source calculations used to obtain the cross sections for reflector sub-assemblies introduce consistent biases at a finer scale of comparison.

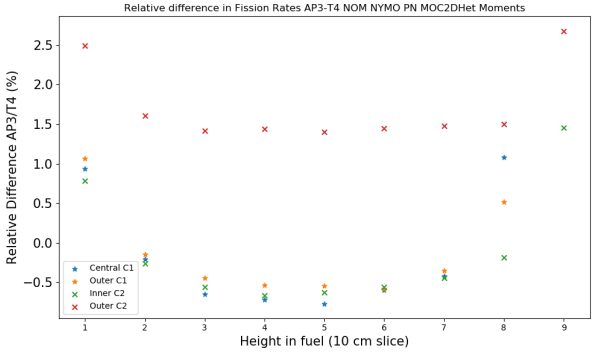

(a) *Relative error (%) on fission rates, axial traverse, NOM configuration.*

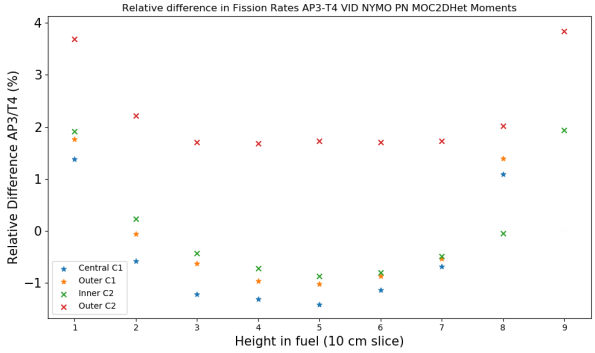

(b) *Relative error (%) on fission rates, axial traverse, VOID configuration.*

Figure 4.11 Relative errors on fission rates along the four axial traverses, NYMO with XS from MOC2DHet - TRIPOLI4 reference scores, NOM (a) and VOID (b) configurations.

MINOS diffusion with MOC2DHet cross sections MINOS calculations results in the Diffusion approximation are presented. Figures 4.12 (a) and (b) show the relative errors on axially integrated fission rates. Both configurations display excellent RMS errors of $RMS_{NOM} = 0.34\%$ and $RMS_{VID} = 0.54\%$ respectively. The errors' structure on the x-y plane reveals a consistent over estimation of rates at the radial reflectors' interface, a feature shared with the previous results presented. However, it appears that rates on the "inner" C2 ring are consistently underestimated in both NOM and VOID configurations. This type of effects could suggest important compensations introduced by the diffusion approximation. The importance of such compensating effects on the flux's calculation could be assessed by analyzing the radial distribution of errors, presented in figures 4.13 (a) and (b). In the nominal configuration, radial effects can be seen, displaying the clear tendency of underestimating rates in the inner C2 assemblies at all heights, apart from $h = 1$ and $h = 9$. It can also be seen that the C1 fuel region is accurately represented for all heights, except for $h = 1$ and $h = 9$ once again. On the other hand, analysis of sub-figure 4.13(b) reveals additional axial compensation effects. These involve relatively important biases of $\sim \pm 1\%$, in the inner axial part of the core, when looking at different heights' contributions. However, as seen in figure 4.12, these effects compensate each others, leading to a seemingly perfect precision in the inner radial part, with biases on integrated rates of the order of $\sim 0.01\%$. This type of compensation is expected in the diffusion approximation and it is worth highlighting the impressive precision of MINOS results. This makes the solver particularly interesting for

fast and rather precise evaluations of macroscopic quantities such as reactivity or integrated fission rates.

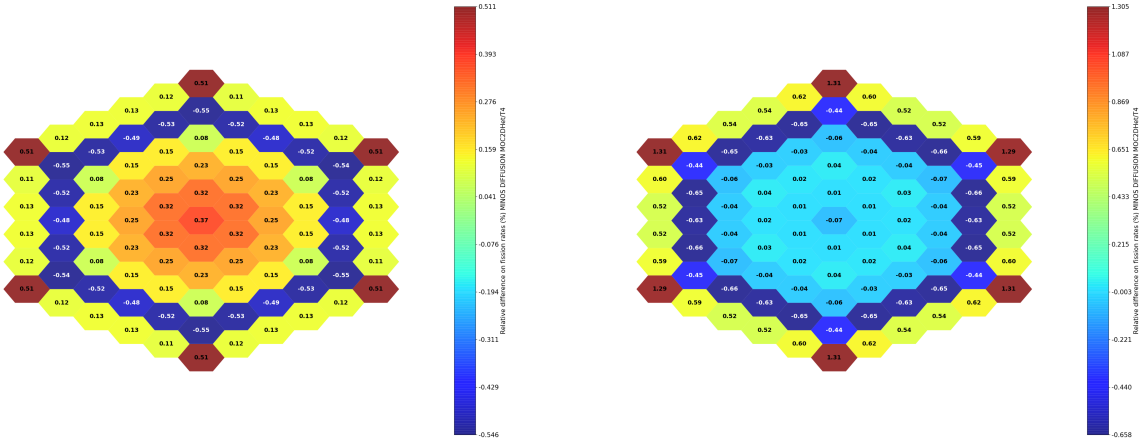

(a) *Relative error (%) on axially integrated fission rates, NOM configuration.*

(b) *Relative error (%) on axially integrated fission rates, VOID configuration.*

Figure 4.12 2D Map of relative errors on axially integrated fission rates, MINOS diffusion with XS from MOC2DHet - TRIPOLI4 reference scores, NOM (a) and VOID (b) configurations.

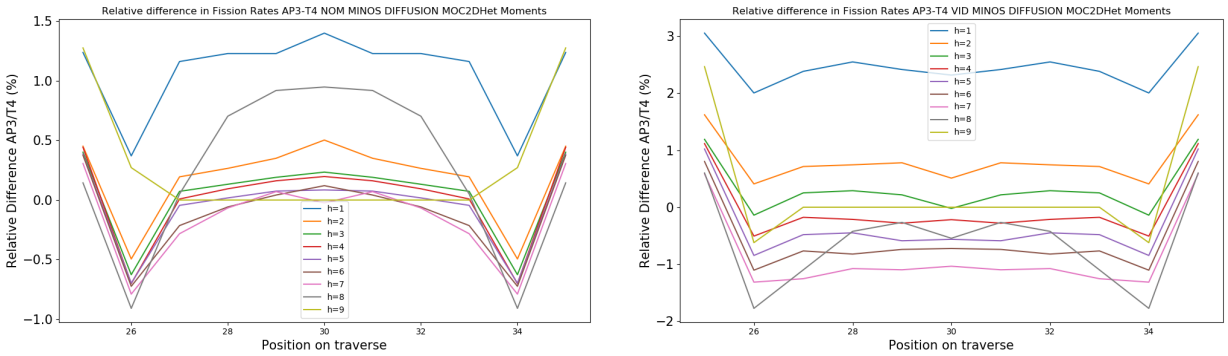

(a) *Relative error (%) on fission rates, radial traverse, NOM configuration.*

(b) *Relative error (%) on fission rates, radial traverse, VOID configuration.*

Figure 4.13 Relative errors on fission rates on radial traverse, MINOS diffusion with XS from MOC2DHet - TRIPOLI4 reference scores, NOM (a) and VOID (b) configurations.

MINOS SP_3 with MOC2DHet cross sections A quick glance at MINOS SP_3 results from MOC2DHet cross sections reveal a similar behavior to that observed using exact transport solvers MINARET and NYMO. The 2D map of relative errors on axially integrated fission rates (fig. 4.14 (a)) displays a similar radial reflector effect as the one observed in S_N and P_N calculations. Furthermore, MINOS SP_3 results for NOM have a root mean squared

error of $RMS_{NOM} = 0.49\%$ on fission rates which outperforms its exact transport counterparts. Despite obtaining a slightly better estimation of fission rates, it can be seen that the biases' axial dependency is similar to the MINARET or NYMO case, once again highlighting the scheme's need for a better axial reflector model.

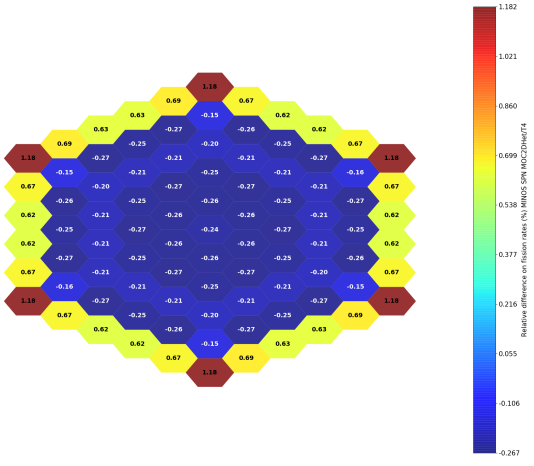

(a) *Relative error (%) on axially integrated fission rates, NOM configuration.*

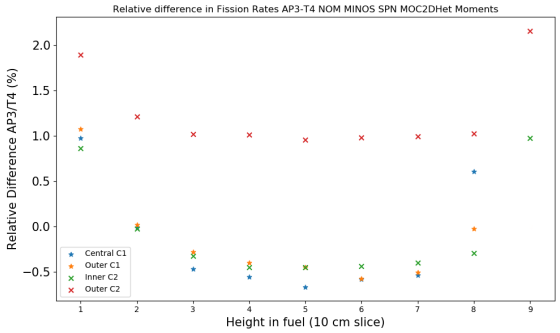

(b) *Relative error (%) on fission rates, axial traverse, NOM configuration.*

Figure 4.14 2D Map of relative errors on axially integrated fission rates (a), Relative errors along the four axial traverses (b), MINOS SP_3 with XS from MOC2DHet - TRIPOLI4 reference scores, NOM configuration

In the voided configuration, RMS error on fission rates goes up to $RMS_{VOID} = 0.86\%$, the corresponding 2D errors map and their dependence along the axial traverses can be seen in figures 4.15(a) and (b). Once again, the behavior of the error is really close to the one observed in MOC2DHet MINARET results. Indeed, it can be seen that the biases on both axial and radial reflector effects see their amplitudes increase in the presence of voided regions.

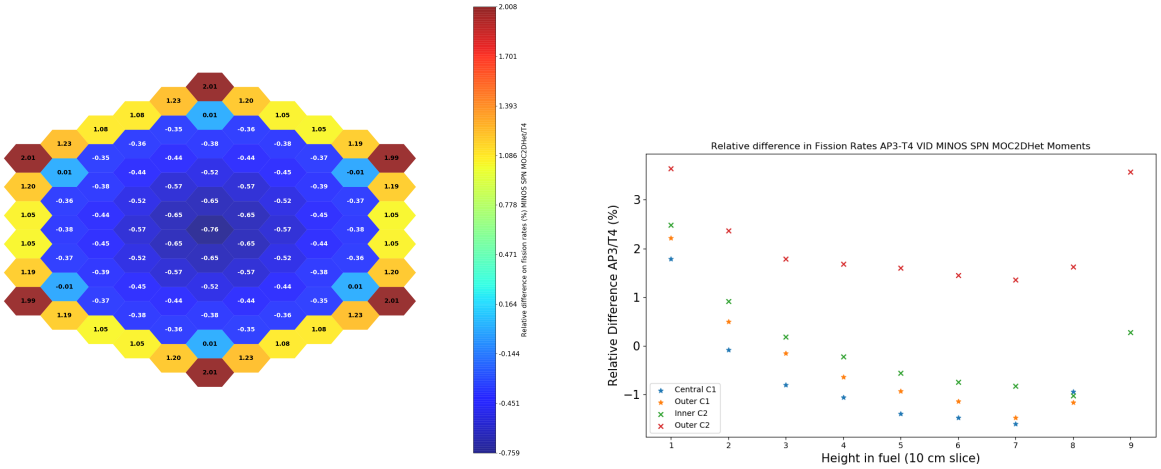

(a) *Relative error (%) on axially integrated fission rates, VOID configuration.*

(b) *Relative error (%) on fission rates, axial traverse, VOID configuration.*

Figure 4.15 2D Map of relative errors on axially integrated fission rates (a), Relative errors along the four axial traverses (b), MINOS SP_3 with XS from MOC2DHet - TRIPOLI4 reference scores, VOID configuration

4.6.2 Hybrid 2D1D results in NYMO and MINOS

NYMO P_3 with hybrid 2D1D cross sections NYMO calculations in the P_3 approximation are ran using hybrid 2D1D cross sections. For the nominal configuration, the resulting error distribution maps are shown in figure 4.16(a) and the relative errors along the axial traverses are plotted in figure 4.16(b). In the voided case, the corresponding relative errors are shown in figure 4.17 (a) and (b).

The Root Mean Squared errors associated with hybrid 2D1D NYMO fission rates are 0.80% for the nominal case and 1.03% for the voided one. These appear similar to RMS errors obtained from hybrid 2D1D in MINARET, and slightly worse than ones obtained in NYMO using the MOC2DHet cross sections. In both configurations, the error distribution display similar behavior as in the MINARET case. Indeed, radial reflector effects leading to comparable over estimations are witnessed in figures 4.16 (a) and 4.17 (a). The axial distribution of errors shown in figures 4.16(b) and 4.17(b) is also similar to the ones obtained from the same cross sections in MINARET. Taking into account NYMO and MINARET computation times and RAM usage, the similar errors consistently obtained with both MOC2DHet and hybrid 2D1D schemes tend to show NYMO's strengths, placing it as an interesting competitor to MINARET for reference transport calculations.

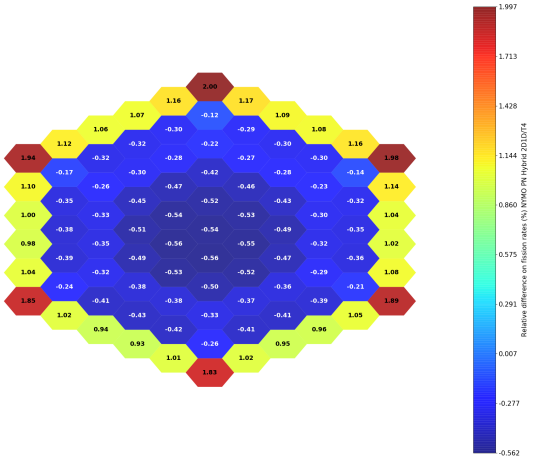

(a) *Relative error (%) on axially integrated fission rates, NOM configuration.*

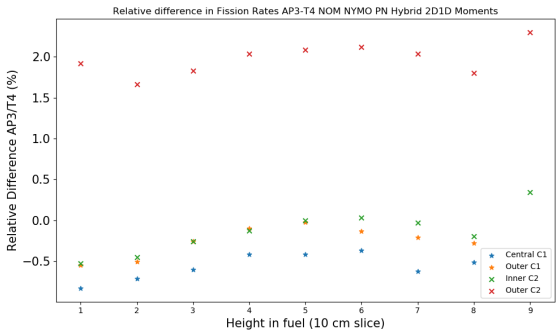

(b) *Relative error (%) on fission rates, axial traverse, NOM configuration.*

Figure 4.16 2D Map of relative errors on axially integrated fission rates (a), Relative errors along the four axial traverses (b), NYMO P_3 with XS from hybrid 2D1D - TRIPOLI4 reference scores, NOM configuration

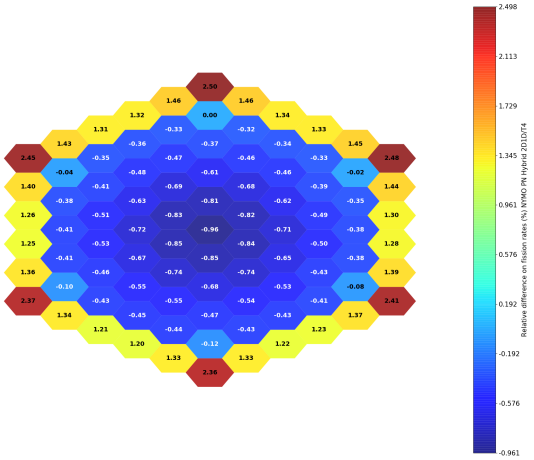

(a) *Relative error (%) on axially integrated fission rates, VOID configuration.*

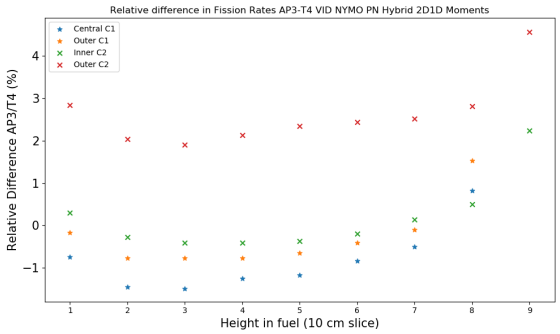

(b) *Relative error (%) on fission rates, axial traverse, VOID configuration.*

Figure 4.17 2D Map of relative errors on axially integrated fission rates (a), Relative errors along the four axial traverses (b), NYMO P_3 with XS from hybrid 2D1D - TRIPOLI4 reference scores, VOID configuration

MINOS diffusion with hybrid 2D1D cross sections In order to get a better understanding of how hybrid 2D1D cross sections behave in different full core approximations, their treatment is extended to MINOS in the diffusion approach. Relative error maps for NOM and VOID configurations shown in figures 4.18 (a) and 4.19 (a) display high performances in terms of the RMS errors calculated. Indeed, the error maps display a nominal RMS_{NOM} of

0.38% and a voided RMS_{VOID} of 0.67% respectively.

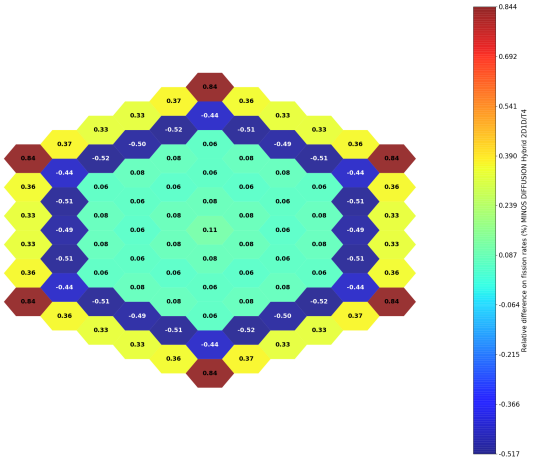

(a) *Relative error (%) on axially integrated fission rates, NOM configuration.*

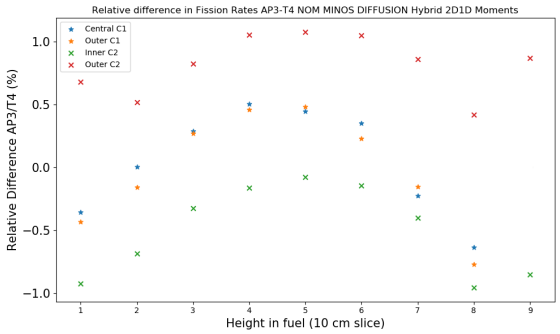

(b) *Relative error (%) on fission rates, axial traverse, NOM configuration.*

Figure 4.18 (a) 2D Map of relative errors on axially integrated fission rates, (b) Relative errors along the four axial traverses. MINOS diffusion calculation with XS from hybrid 2D1D, NOM configuration

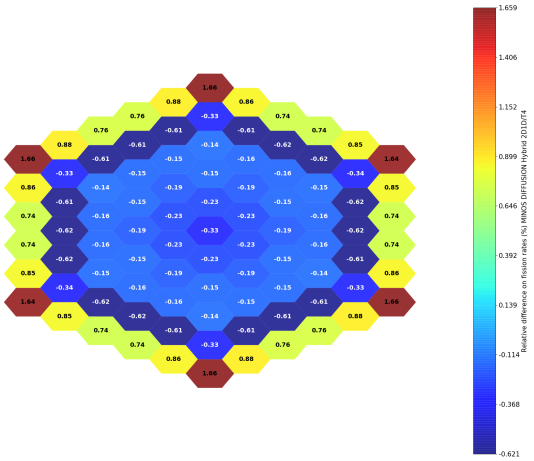

(a) *Relative error (%) on axially integrated fission rates, VOID configuration.*

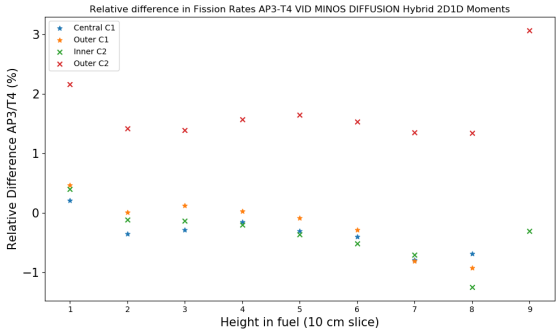

(b) *Relative error (%) on fission rates, axial traverse, VOID configuration.*

Figure 4.19 (a) 2D Map of relative errors on axially integrated fission rates, (b) Relative errors along the four axial traverses, MINOS diffusion calculations with XS from hybrid 2D1D, VOID configuration

Once again, the apparent "macroscopic" precision associated with the hybrid 2D1D/diffusion combination must be analysed. Indeed, the low error on voiding effect ($\Delta\Delta\rho_V = -22pcm$) and the impressive RMS errors displayed in both configurations seem to indicate that this

lattice/full core solver combination would be ideal. However, it appears particularly apparent from figures 4.18 (a) and 4.19 (a) that radial compensation effects come into play. Indeed, in a similar fashion as for the MOC2DHet/diffusion combination, the overestimation of outer C2 fission rates seems to be correlated with a systematic underestimation of fission rates in inner C2 assemblies. Axial compensation effects can similarly be seen, especially from figure 4.18 (b), which shows that rates close to axial reflectors' interfaces tend to be underestimated while those in the central axial area tend to be overestimated. In particular, this effect of compensation is what leads to the impressive precision on axially integrated rates in the C1 fuel area.

MINOS SP_3 with hybrid 2D1D cross sections Results obtained with MINOS SP_3 from hybrid 2D1D cross sections are shown in figures 4.20 and 4.21. In the nominal configuration, a RMS error of 0.64% on fission rates is obtained. The latter are displayed in figure 4.20 (a). In the voided case, relative errors on fission rates amount for a RMS error of 1.02%, as displayed in figure 4.21 (a).

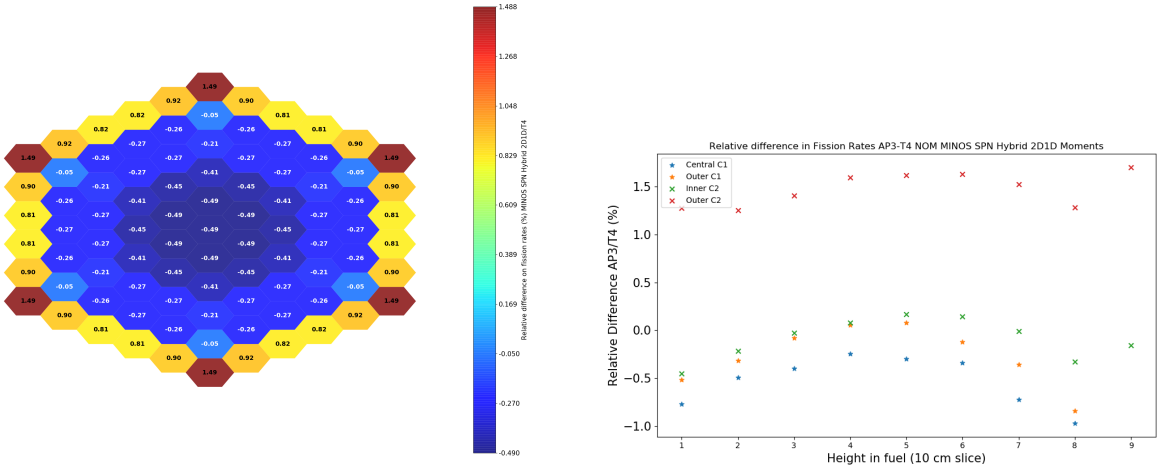

(a) *Relative error (%) on axially integrated fission rates, NOM configuration.*

(b) *Relative error (%) on fission rates, axial traverse, NOM configuration.*

Figure 4.20 (a) 2D Map of relative errors on axially integrated fission rates, (b) Relative errors along the four axial traverses. MINOS SP_3 calculation with XS from hybrid 2D1D, NOM configuration

The evolution of the relative errors in the axial direction are displayed in figures 4.20 (b) and 4.21 (b). The latter clearly show a similar over estimation of outer C2 rates, consistent with biases introduced from the radial reflector model used. Furthermore, the evolution of biases in the nominal configuration seems to indicate adequate treatment of the lower reflector. This hints at potential advantages of the 2D1D methods compared to the more traditional schemes

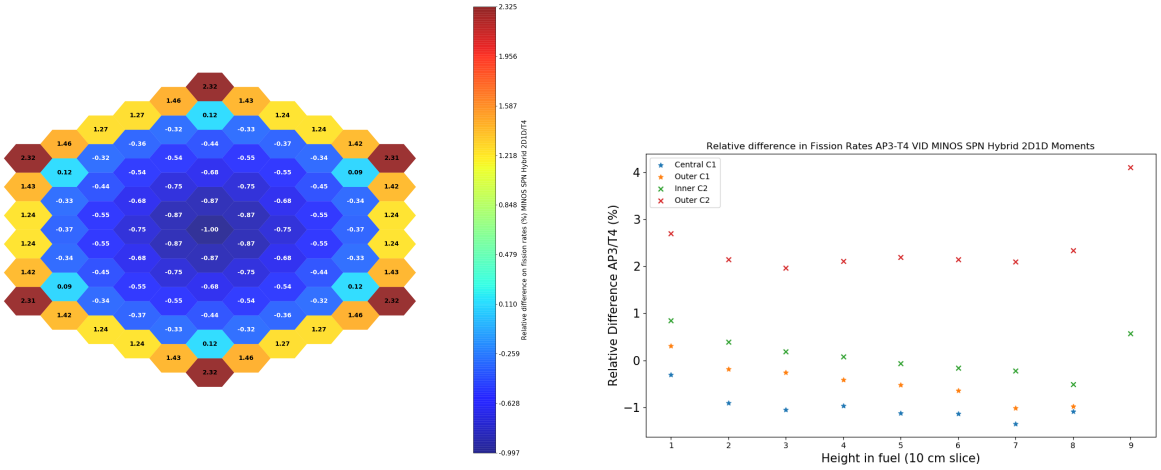

(a) *Relative error (%) on axially integrated fission rates, VOID configuration.*

(b) *Relative error (%) on fission rates, axial traverse, VOID configuration.*

Figure 4.21 (a) 2D Map of relative errors on axially integrated fission rates, (b) Relative errors along the four axial traverses. MINOS SP_3 calculations with XS from hybrid 2D1D, VOID configuration

based on 2D MOC. However, this is not entirely convincing in the voided case, in which the over estimation of fission rates in slice $h = 9$ would seem to indicate an underestimation of leakage through the voided plenum. This interpretation is supported by the overestimation of the configuration's reactivity, as well as the possible misrepresentation of voiding effects at the hybrid 2D1D lattice stage, hinted by the positive void effects shown in table 4.2.

4.7 Comparison with results from the Takeda benchmark

In 2013, capabilities of MINOS and MINARET at evaluating voiding effects on reactivity had been studied by C. Bay [43]. Since all of Bay's calculations have been performed using the same 4 groups cross sections presented in Takeda's paper [44], it will be assumed that the bias associated with these cross sections can be neglected. The main conclusions drawn from Bay's work are that full core solvers based on the S_N method, such as MINARET, offer the best precision when evaluating both K_{eff} and $\Delta\rho_V$. Indeed, MINARET results, obtained with no control rods, presented in [43] display errors down to a few *pcm* in the nominal configuration and only ~ 20 *pcm* in the voided plenum configuration. This leads to a total error of 25 *pcm* on the plenum voiding effect for MINARET S_8 calculations. On the other hand, conclusions drawn from this 2013 study revealed that the MINOS SP_3 and SP_5 techniques did not provide satisfying results with biases on K_{eff} values of -483 *pcm* and -1151 *pcm* for the nominal and voided configurations respectively, in the SP_3 approximation. This amounted to a total

bias of -668 *pcm* compared to their TRIPOLI4 reference calculation.

This greatly differs from results presented earlier in section 4.6, for which it can be seen that the MINOS SP_3 treatment seems to display consistently smaller biases than those associated with MINARET calculations. This could be due to the fact that the SP_3 approximation is more suited to treat the ANTOINID core than Bay's modified Takeda-4 benchmark. This could be due to the ANTOINID design being bigger and more "homogeneous" compared to the previously studied Takeda-4 benchmark. This could make the ANTOINID core more suited for SP_N calculations as it appeared that even the diffusion approximation was not so penalizing. Indeed, as seen from comparing tables 4.8, 4.9, 4.10 and 4.11, the origin of cross sections is one of the dominant factors when considering precision of full core calculations. This can be particularly seen with the introduction of the B-heterogeneous leakage model, along with a Flux-Moments homogenization technique which seem to greatly improve performances at the full core step for all solvers, as seen in both MOC2DHet and hybrid 2D1D schemes. It is possible that these methods involved in obtaining cross sections up to order 3 in anisotropy are more suited for SP_3 calculations than those from the modified Takeda benchmark used in Bay's study. Indeed, the latter considered isotropic 4 groups cross sections with the aim of comparing full core solver's capabilities. This could potentially lead to a consistent misrepresentation in the SP_3 and SP_5 treatments. Alternatively, it could potentially be explained by work done in MINOS since this anterior survey of capabilities of full core solver.

CHAPTER 5 CONCLUSION

5.1 Summary of Works

The present research has allowed to reveal the strengths and drawbacks of five APOLLO3 lattice calculation schemes applied to Sodium Fast Reactors. It has been shown that for a relatively small core with a high void effect on reactivity, the main limitation in a two-step scheme is the generation of the cross sections at the lattice step. In Chapter 3, the SCRAP scheme, originally developed for design studies, was introduced and tested. The latter was based on three primary hypotheses to perform lattice calculations. The first hypothesis was about the radial homogeneity of SFR fuel sub-assemblies and that judging by their fast spectrum, it was possible to perform the main flux calculation directly on the homogenized geometry, provided that the self-shielding treatment had been carried out beforehand on the exact heterogeneous geometry. The second was that neutron leakage from fuel sub-assemblies was correctly represented by the homogeneous B1 model, even in the case of voided configurations. Lastly, it was assumed that the 33 group cross sections for the reflectors could be obtained from an independent source calculation performed on the homogenized reflector geometry. As the sodium void effects on reactivity calculated by MINOS were not satisfying using SCRAP cross sections, a total of four additional lattice schemes were presented, in order to test the original hypotheses associated with the SCRAP scheme. First, the homogeneous radial geometry hypothesis was tested by introducing a more precise, 1760 groups MOC flux calculation, performed on the exact fuel sub-assembly geometries. This lead to a better precision on the estimation of fission rates. However, a lingering misrepresentation of axial effects resulted once again into an incorrect prediction of the sodium void effect on reactivity. It was thus concluded at the end of Chapter 3, that the *homogeneity* hypothesis introduced for SCRAP flux calculations was not a limiting factor to the representation of voiding effects at the lattice stage. It was then hypothesized that the B1-homogeneous leakage model involved in SCRAP and MOC2DHom calculations was the cause for the misrepresentation of the sodium void effect. A more complex method for representing the important axial effects present in voided configurations thus appeared necessary.

In an attempt to find a solution, three advanced schemes were presented in Chapter 4. First, the MOC2DHet scheme based on a B-heterogeneous method implemented in the 2D TDT-MOC solver was introduced. Then, the full 2D1D and hybrid 2D1D schemes were applied, making use of the 2D1D iterative scheme implemented in APOLLO3. The performances of

the three advanced schemes were confronted on 3D full core calculations using the reference transport solver MINARET. The analysis of the biases introduced by MINARET calculations reveal that the use of the heterogeneous leakage model combined with a Flux-Moments condensation technique provides a better description of axial leakage effects, showing that the *homogeneous* leakage hypothesis used in SCRAP was not suited to treat voided configurations of the ANTOINID core. Further analysis of the results from MOC2DHet reveal that an independent source calculation treatment of reflectors induces systematic biases on fission rates at the interfaces with reflectors. The axial *reflector model* hypothesis was then tested through 2D1D calculations. Although the full 2D1D version did not give satisfying results, the hybrid version hinted at the fact that a better treatment of axial reflectors was possible, reducing the biases at interfaces with the axial reflectors. These biases appeared to be rather important when using the MOC2DHet scheme.

At the end of Chapter 4, the test cases were extended to the NYMO P_N solver, as well as to the MINOS solver, including both the diffusion and the SP_N approximations. The performances of the MOC2DHet and hybrid 2D1D schemes in MINOS and NYMO were briefly analyzed, showcasing the advantageous computational and RAM usage of these solvers.

This work provides an overview of APOLLO3 capabilities in the treatment of voided accidental configurations on the open ANTOINID core. Hopefully, it gives a rough idea for expected performances of the numerical methods implemented, considering a cost/precision approach. As often, complex computational methods lead to more important calculation times, as seen with MOC2DHet and 2D1D schemes presented in Chapter 4.

The primary conclusions about SFR lattice schemes that can be drawn from this work can be summarized as the following :

1. The MOC2DHet scheme appeared optimal when calculating sodium void effects on reactivity for S_N, P_N and SP_N full core calculations. Its use of a B-heterogeneous leakage model and a flux-moments homogenization technique are understood to be the responsible for the scheme's performances.

2. The B1-homogeneous model, used in SCRAP and MOC2DHom schemes can be concluded to be unsuited for the calculation of voided configurations.

3. The hybrid 2D1D scheme displayed interesting improvements in the representation of the axial reflectors. However, further validation through a TRIPOLI-4 comparison would be necessary to be fully confident in the method's robustness.

4. All schemes suffered from a misrepresentation of the radial reflectors.

5. The full 2D1D scheme did not provide satisfactory results, it is assumed that this could be due to potential errors in the method's implementation or to the lack of robustness in the method used to perform fixed eigenvalue source calculations.

The main conclusions emerging from the survey of full core solvers are :

1. MINARET (S_N) and NYMO (P_N) exact transport solvers give equivalent "reference" results.

2. Performances of the NYMO solver are particularly interesting in terms of computational time, while displaying a precision similar to MINARET.

3. MINOS SP_3 and diffusion results are in a surprisingly good agreement with reference TRIPOLI-4 calculations. However it was shown that the diffusion approximation introduced important radially and axially compensating effects, as unveiled by the analysis of fission rates.

4. A consistent difference of about 200 *pcm* on the calculated sodium voiding effect can be observed between diffusion and exact transport calculations. This could give a rough idea of the type of biases introduced by the diffusion approximation.

5. Similarly, a difference of about 90 *pcm* on the sodium void effect is recorded between simplified and exact transport calculations.

6. Comparisons with Bay's 2013 work on the modified Takeda benchmark revealed some important differences when comparing MINOS SP_3 results.

Additional work, presented in Appendix B, was done on the implementation of an interface to convert multi-parameter cross-sections libraries from the APOLLO3 format to the PARIS input format used in the SEASON platform. This was presented at LMAG (*Laboratoire de Modélisation des Accidents Graves*) to demonstrate the possibility to link APOLLO3 lattice calculation outputs to full core calculations with the SNATCH [18] or IDT solver. Although the implementation is not optimized in terms of time and memory access, it serves as a proof of concept that the replacement of the ECCO module by APOLLO3 for SEASON lattice calculations is possible.

5.2 Limitations

The approach presented in this work was based on an original set of three hypotheses. From this set of initial assumptions, the first two about fuel assembly *homogeneity* and *leakage*

models were thoroughly tested. However, the third hypothesis made on *reflector models* was only tested for axial reflectors in the 2D1D formalism. The analysis of hybrid 2D1D results presented in Chapter 4, reveals that the more advanced 2D1D methods can provide better description of axial reflectors thanks to the 2D1D formalism.

However, 2D1D assembly calculations and full core full 2D1D results show that more works needs to be done in order to master and validate the 2D1D method. Once again, the 2D1D fusion approach is still exploratory, and subject to inconsistencies in implementation and maintenance since B. Faure's work [11]. This could explain the rather incoherent results obtained from the full 2D1D variant. Despite the hybrid 2D1D results indicating a certain improvement in the axial reflectors' description, it also highlights the need for a better radial reflector model. In this sense, the results presented are hard to interpret as both axial and radial effects are difficult to de-correlate. Indeed, for a relatively small core of the scale of the ANTOINID, the radial leakage effects can become dominant due to the fast neutron spectrum. This questions one of the hypothesis made, which was that the error on voiding effect came from the axial reflector's misrepresentation. Indeed, as the fuel regions are voided, the neutrons tend to have a higher energy, which potentially implies more leakage through the radial reflectors. This leads to conclude that one of the main drawbacks of this approach is that only axial effects were considered and that radial effects have been neglected introducing a common bias in all of the presented schemes, due to the radial reflector model. Lastly, it is worth pointing out that simply comparing reactivity values and fission rates doesn't give the full picture and is not sufficient to fully characterize the two steps scheme's performances. Alternatively, it could have been relevant to directly compare the neutron flux distribution in the 3D core model. This additional point of comparison could help get a better understanding of the effects of reflectors and thus provide specific insights on potential effects of compensations for example.

The simple fact that all lattice schemes and full core solvers presented were only tested on the ANTOINID core represents in itself another limitation. Indeed, as hinted by the comparison of the present full core results with those of C. Bay on their modified Takeda-4 benchmark, it is possible that the relatively simple ANTOINID geometry makes it easier to model than other designs. This introduces an additional difficulty when trying to extrapolate results from the present study to other applications. This comparison of present and past results at the full core scale hints for the need of a benchmarking strategy which would allow for a more in-depth comparison of the available methods. It must however be noted that the Takeda benchmarks would not be suited for comparing lattice calculations as their exact assembly geometries and compositions are not specified in Takeda and Ikeda's original paper [44].

From a accidental transient analysis perspective, the main drawback of the solutions presented in Chapter 4 is their consequent computational times. In the aim of setting up an iterative coupled scheme in the SEASON platform for example, it would appear necessary to reduce lattice scheme calculation times if cross sections are to be computed "on the fly". Another limitation would be that all of these results assume a prior knowledge of the assemblies' geometries. However, in the event of structural damages to the assemblies, their geometry would change consequently and the local materials densities would be altered. This represents an important challenge for the neutronic calculation and was not considered during the course of this work.

The main limitations that were identified in the course of this project can be summarized as the following points :

1. Both full and hybrid 2D1D lattice calculations were not properly compared and validated to a Monte Carlo reference result.
2. The 1D (SCRAP) or 2D (MOC) source calculations used to model the reflectors introduce consistent biases. In particular, this highlighted the errors introduced by the radial reflector which appears not to have been properly treated in this work.
3. The conclusions drawn from this specific study based on the ANTOINID design are not necessarily easily generalized to more complex core designs.

5.3 Future Research

5.3.1 Suggestions to treat the limitations identified in this work

Investigation of the 2D1D fusion approach : As the full 2D1D results are not satisfying, it appears that additional work is required to investigate the cause of these biases. It is hypothesized that the description of the fissile sub-assemblies through 2D MOC source calculations does not give valid results, as unveiled by the full core calculations presented in this work. This issue could be investigated by studying a reference TRIPOLI-4 model in order to identify where the 2D1D calculations fail. Some work towards the T4 model simulation has already been done and it would be relevant to continue from where it was left. Full and hybrid 2D1D calculations could then be confronted to reference Monte Carlo simulations on a single fuel assembly, in order to obtain a more detailed estimation of their performances. It is hoped that this could help explaining the surprising sodium void effect values calculated from IDT-1D eigenvalues. As it stands, it is still unsure if these issues can be tackled by modifying the existing script used to call the 2D1D solver, or whether there are inherent

issues with the APOLLO3 implementation. In order to check this, it could be relevant to attempt the same 2D1D treatment of the ANTOINID assemblies using an anterior version of APOLLO3, ideally the version in which B. Faure developed the original 2D1D module.

Radial reflector models : Further investigation of possible reflector models would be relevant. A particular attention to the radial reflector model would be necessary as it has been omitted in the present study. In order to assess the biases associated with the model used in this work, alternative types of reflector models should be considered. One could imagine calculating the flux in the reflector from a traversing motif which would include enough fuel assemblies such that a critical ($K_{eff} = 1$) domain is obtained.

Furthermore, a two dimensional core model could also be imagined in order to treat radial effects independently of the axial distribution. This approach would allow for the validation of a radial reflector model through a reference two-dimensional full core calculation using MINARET or NYMO.

Introduction of 3DMOC assembly calculations : It would also be relevant to perform assembly calculations in a 3D MOC approach as the recent developments in accelerating three dimensional calculations made by Santandrea et al. [16] could provide a competitive alternative to 2D MOC or 2D1D fusion methods. It was intended for a 3D MOC scheme to be tested as part of this work, however it was not possible given the time constraints.

Validation of the MPOtoXML interface : Further work using the MPOtoXML interface presented in Appendix B, could also be imagined. First of all, it would be necessary to "validate" the interface itself in order to make sure that no bias could simply come from its implementation. As seen in the results presented in Appendix B, more work would be required to validate the ANTOINID study using the SNATCH solver. Developments made in this direction would open new possibilities for using APOLLO3 generated cross sections in the PARIS platform, including in SEASON full core simulations. This action could be carried out along with the development of a neutronic scheme to be used in SEASON, for which a hybrid architecture could be envisioned. This would allow for the pre-calculation of multi-parameter cross section libraries which could be used in the first accidental phase, during which the main geometric features of the assemblies are preserved. In the second accidental phase when the geometries would have degraded, a fast infinite medium calculation could be performed "on the fly", in order to take into account the relocation of materials, such as fuel assemblies melting for example. This would contribute to more precise coupled accidental transients calculations.

5.3.2 A more general benchmarking strategy

This work has allowed to show that the accurate representation of voided configurations in SFRs still represent a challenge to this day. A deeper analysis of the different methods and their associated biases should be approached through their extension to more benchmark test cases. These could include designs such as the ANTOINID, Bay's modified Takeda-4 benchmark [43] [44] (only for full core calculations) and the JPN (JF-36) core [30]. Alternatively, an adapted "CFV-like" benchmark such as the FBR, referred to by A. Calloo [46] could be used. However, it must be noted that its specific design has not been published yet. This approach would help removing dependencies to specific designs and give a better idea of the domain of applicability of each lattice/solver combination. To start with, the 2D MOC lattice scheme based on the B-heterogeneous leakage model (MOC2DHet) could be extended to the JF-36 benchmark. It would also be relevant to test it for the ASTRID case, as suggested by B. Faure et al. in [47]. It should be kept in mind that in this 2D MOC approach, a more advanced radial reflector model should be considered as pointed out earlier in this work. Additionally, treatment of a variety of other assembly geometries could also help fixing and validating the 2D1D fusion approach. Similarly, it would be worth comparing these results with the 3D MOC approach to assembly calculations. Moreover, comparisons with the DRAGON5 lattice code could be relevant as it is also capable of producing condensed and homogenized cross sections in the MPO format.

Regarding the treatment of full core calculations, it would be ambitious but relevant to run a series of tests on all of the available benchmarks in order to compare the full core solvers at our disposal. This would require the clear definition of a series of benchmark tests that would reflect the capabilities of each solver to simulate voided configurations. Provided for the MPOtoXML interface to be validated, the possibilities of full core solvers could be extended to those available in the PARIS platform.

This academic approach would allow for a more complete survey of DRAGON5 and APOLLO3 lattice calculation capabilities on a wider variety of SFR assembly designs. The cross sections generated by these calculations would all be available in the MPO format which opens up for the possibilities of comparing full core calculations from APOLLO3, DONJON5 and even the PARIS platform. However, it must be kept in mind that these suggestions would be ambitious and would not necessarily comply with CEA's interests and obligations towards its industrial partners. Nonetheless, future academic collaborations between CEA and Ecole Polytechnique de Montréal, similar to this project, could be imagined.

REFERENCES

[1] A. Hebert, *Applied Reactor Physics*. Presses internationales Polytechnique, 2009. [Online]. Available: https://books.google.fr/books?id=sibA5ECQ8LoC

[2] P. Mosca, L. Bourhrara, A. Calloo, A. Gammicchia, F. Goubioud, L. Mao, F. Madiot, F. Malouch, E. Masiello, F. Moreau, S. Santandrea, D. Sciannandrone, I. Zmijarevic, E. Y. Garcias-Cervantes, G. Valocchi, J. Vidal, F. Damian, P. Laurent, A. Willien, A. Brighenti, L. Graziano, and B. Vezzoni, "APOLLO3®: Overview of the new Code Capabilities for Reactor Physics Analysis," in *M&C 2023 - The International Conference on Mathematics and Computational Methods Applied to Nuclear Science and Engineering*, Niagara Falls, Ontario, Canada, August 2023, APOLLO3® is a registered trademark of CEA.

[3] E. Brun, F. Damian, C. Diop, E. Dumonteil, F. Hugot, C. Jouanne, Y. Lee, F. Malvagi, A. Mazzolo, O. Petit, J. Trama, T. Visonneau, and A. Zoia, "TRIPOLI-4®, CEA, EDF and AREVA reference Monte Carlo code," *Annals of Nuclear Energy*, vol. 82, pp. 151–160, 2015, joint International Conference on Supercomputing in Nuclear Applications and Monte Carlo 2013, SNA + MC 2013. Pluri- and Trans-disciplinarity, Towards New Modeling and Numerical Simulation Paradigms. [Online]. Available: https://www.sciencedirect.com/science/article/pii/S0306454914003843

[4] J. E. Kelly, "Generation IV international forum: A decade of progress through international cooperation," *Progress in Nuclear Energy*, vol. 77, pp. 240–246, 2014. [Online]. Available: https://www.sciencedirect.com/science/article/pii/S0149197014000419

[5] G. H. Golden and J. V. Tokar, "Thermophysical properties of sodium." 1 1967. [Online]. Available: https://www.osti.gov/biblio/4511962

[6] F. Petiot and J. M. Seiler, "Physical properties of sodium: a contribution to the estimation of critical coordinates," *High Temperatures - High Pressures*, vol. 16:3, pp. 289–293, Jan 1984.

[7] J. Guidez, *Phenix: le retour d'experience*. EDP Sciences, 2013. [Online]. Available: https://books.google.fr/books?id=YsxAnwEACAAJ

[8] G. Gaillard-Groleas, J.-C. Garnier, J.-M. Hamy, E. Girardi, M. Hirata, J.-P. Grouiller, L. Martin, F. Serre, M. Phelip, C. Doderlein, B. Michel, M. Lainet, B. Fontaine,

C. Suteau, A. Gerschenfeld, and J. Cardolaccia, "Improvements in simulation tools to be developed within the framework of the ASTRID project," in *ICAPP 2016 - International Congress on Advances in Nuclear Power Plants*, San Francisco, United States, Apr. 2016. [Online]. Available: https://cea.hal.science/cea-02509775

[9] W. Maschek, A. Rineiski, M. Flad, P. Liu, X.-N. Chen, Y. Tobita, H. Yamano, T. Suzuki, S. Fujita, K. Kamiyama, S. Pigny, t. Cadiou, K. Morita, and G. Bandini, "The simmer safety code system and its validation efforts for fast reactor application," *International Conference on the Physics of Reactors 2008, PHYSOR 08*, vol. 3, pp. 2370–2378, 01 2008.

[10] G. Rimpault, D. Plisson, J. Tommasi, R. Jacqmin, J.-M. Rieunier, D. Verrier, and D. Biron, "The ERANOS code and data system for fast reactor neutronic analyses," in *PHYSOR 2002 - International Conference on the New Frontiers of Nuclear Technology: Reactor Physics, Safety and High-Performance Computing*, Seoul, South Korea, Oct. 2002. [Online]. Available: https://cea.hal.science/cea-02906396

[11] B. Faure, "Development of neutronic calculation schemes for heterogeneous sodium-cooled nuclear cores in the APOLLO3 code : application to the ASTRID prototype," Ph.D. dissertation, 2019, thèse de doctorat dirigée par Buiron Laurent; Energie, Rayonnement, Plasma Aix-Marseille 2019. [Online]. Available: http://www.theses.fr/2019AIXM0289

[12] J. Tommasi, "Heterogeneous Bn equations and symmetries," *Annals of Nuclear Energy*, vol. 85, pp. 145–158, 2015. [Online]. Available: https://www.sciencedirect.com/science/article/pii/S0306454915002479

[13] J.-J. Lautard and J.-Y. Moller, "MINARET, a deterministic neutron transport solver for nuclear core calculations," May 2011, international Conference on Mathematics and Computational Methods Applied to Nuclear Science and Engineering (MC 2011). [Online]. Available: https://cea.hal.science/cea-00545919

[14] K. Assogba, L. Bourhrara, I. Zmijarevic, G. Allaire, and A. Galia, "Spherical harmonics and discontinuous galerkin finite element methods for the three-dimensional neutron transport equation: Application to core and lattice calculation," *Nuclear Science and Engineering*, vol. 197, no. 8, pp. 1584–1599, 2023. [Online]. Available: https://doi.org/10.1080/00295639.2022.2154546

[15] A.-M. Baudron and J.-J. Lautard, "Minos: A simplified Pn solver for core calculation," *Nuclear Science and Engineering*, vol. 155, no. 2, pp. 250–263, 2007. [Online]. Available: https://doi.org/10.13182/NSE07-A2660

[16] S. Santandrea, L. Graziano, and D. Sciannandrone, "Accelerated polynomial axial expansions for full 3D neutron transport MOC in the APOLLO3® code system as applied to the ASTRID fast breeder reactor," *Annals of Nuclear Energy*, vol. 113, pp. 194–236, 2018. [Online]. Available: https://www.sciencedirect.com/science/article/pii/S0306454917302402

[17] R. Le Tellier, "Developpement de la méthode des caracteristiques pour ´le calcul de réseau," Ph.D. dissertation, École Polytechnique de Montréal, 2006, PhD thesis, Département de génie physique, available at http://merlin.polymtl.ca/downloads/these_letellier.pdf.

[18] D. Fournier, R. Le Tellier, S. Christophe, and J. Ruggieri, "High-order discrete ordinate transport in hexagonal geometry : A new capability in eranos," *Nuovo Cimento della Societa Italiana di Fisica C*, vol. 33, 07 2009.

[19] F. Févotte, S. Santandrea, and R. Sanchez, "Tracking on periodic lattices for the method of characteristics," *International Conference on the Physics of Reactors 2008, PHYSOR 08*, vol. 1, pp. 420–426, 09 2008.

[20] E. M. Gelbard, "Application of spherical harmonics method to reactor problems," *Bettis Atomic Power Laboratory, West Mifflin, PA, Technical Report No. WAPD-BT-20*, 1960.

[21] P. Archier, J.-M. Palau, J.-F. Vidal, V. Pascal, G. Rimpault, B. Roque, and S. Santandrea, "New Reference APOLLO3 Calculation Scheme for Sodium Cooled Fast Reactors from Sub-Assembly to Full-Core Calculations," *PHYSOR2016 - Unifying Theory and Experiments in the 21st Century*, May 2016. [Online]. Available: https://cea.hal.science/hal-02442247

[22] T. Tone, "A numerical study of heterogeneity effects in fast reactor critical assemblies," *Journal of Nuclear Science and Technology*, vol. 12, no. 8, pp. 467–481, 1975. [Online]. Available: https://www.tandfonline.com/doi/abs/10.1080/18811248.1975.9733139

[23] J. Vidal and D. Raynaud, "Combining the Tone's and subgroup models for reference LWR self-shielding calculations in APOLLO3," in *4th International Conference on Physics and Technology of Reactors and Applications (PHYTRA - 2018)*, Marrakech, Morocco, Sep. 2018. [Online]. Available: https://cea.hal.science/cea-02338608

[24] L. Mao and I. Zmijarevic, "A new Tone's method in APOLLO3 and its application to fast and thermal reactor calculations," *Nuclear Engineering and Technology*, vol. 49, no. 6, pp. 1269–1286, 2017, special Issue on International Conference on Mathematics and Computational Methods Applied to Nuclear Science and Engineering 2017 (M&C 2017). [Online]. Available: https://www.sciencedirect.com/science/article/pii/S1738573317303698

[25] A. Kavenoky, "The SPH homogeneization method," CEA Centre d'Etudes Nucleaires de Cadarache, Tech. Rep., 1978.

[26] A. Hébert and G. Mathonnière, "Development of a third-generation superhomogénéisation method for the homogenization of a pressurized water reactor assembly," *Nuclear Science and Engineering*, vol. 115, pp. 129–141, 1993. [Online]. Available: https://api.semanticscholar.org/CorpusID:118236306

[27] P. Jacquet, "Nouvelles méthodes de modélisation neutronique des réacteurs rapides de quatrième génération," Theses, Université de Grenoble, May 2011. [Online]. Available: https://theses.hal.science/tel-00680530

[28] J.-F. Vidal, P. Archier, B. Faure, V. Jouault, J.-M. Palau, V. Pascal, G. Rimpault, F. Auffret, L. Graziano, E. Masiello, and S. Santandrea, "APOLLO3 homogenization techniques for transport core calculations—application to the ASTRID CFV core," *Nuclear Engineering and Technology*, vol. 49, no. 7, pp. 1379–1387, 2017. [Online]. Available: https://www.sciencedirect.com/science/article/pii/S173857331730267X

[29] J.-F. Vidal, P. Archier, A. Calloo, P. Jacquet, J. Tommasi, and R. Le Tellier, "An improved energy-collapsing method for core-reflector modelization in SFR core calculations using the paris platform," *International Conference on the Physics of Reactors 2012, PHYSOR 2012: Advances in Reactor Physics*, vol. 5, pp. 4136–4149, 01 2012.

[30] H. Kamide, H. Ohshima, S. Kubo, and Y. Chikazawa, "Chapter 12 - Generation-IV Sodium-cooled Fast Reactor (SFR) concepts in Japan," in *Handbook of Generation IV Nuclear Reactors (Second Edition)*, 2nd ed., ser. Woodhead Publishing Series in Energy, I. L. Pioro, Ed. Woodhead Publishing, 2023, pp. 395–418. [Online]. Available: https://www.sciencedirect.com/science/article/pii/B9780128205884000086

[31] J.-F. Vidal, "Contributions à l'amélioration des méthodes déterministes et des schémas de calcul neutronique des réacteurs nucléaires," 2018, mémoire d'Habilitation à Diriger des Recherches, Université-Grenoble Alpes.

[32] I. Zmijarevic, "IDT solution to the 3D transport benchmark over a range in parameter space," *PHYSOR'08: International Conference on the Physics of Reactors 'Nuclear Power: A Sustainable Resource'; Interlaken (Switzerland); 14-19 Sep 2008*, pp. 2914–2921, 01 2008.

[33] W. van Rooijen and G. Chiba, "Diffusion coefficients for LMFBR cells calculated with MOC and Monte Carlo methods," *Annals of Nuclear Energy*, vol. 38, no. 1, pp. 133–144, 2011. [Online]. Available: https://www.sciencedirect.com/science/article/pii/S0306454910002756

[34] F. Varaine, P. Marsault, M.-S. Chenaud, B. Bernardin, A. Conti, P. Sciora, C. Venard, B. Fontaine, N. Devictor, L. Martin, A.-C. Scholer, and D. Verrier, "Pre-conceptual design study of ASTRID core," *International Congress on Advances in Nuclear Power Plants 2012, ICAPP 2012*, vol. 1, 06 2012.

[35] A. Calloo, R. Le Tellier, and D. Labeurthre, "High-order finite elements for the neutron transport equation on honeycomb meshes," in *PHYSOR 2020*, ser. PHYSOR 2020: Transition to a Scalable Nuclear Future, Cambridge, United Kingdom, Mar. 2019. [Online]. Available: https://cea.hal.science/cea-03033109

[36] L. Gastaldo, R. L. Tellier, C.Suteau, D. Fournier, and J. Ruggieri, "High-order discrete ordinate transport in non-conforming 2D Cartesian meshes," in *International Conference on Mathematics, Computational Methods & Reactor Physics (M&C 2009)*, May 2009.

[37] L. Bourhrara, "A new numerical method for solving the boltzmann transport equation using the Pn method and the discontinuous finite elements on unstructured and curved meshes," *Journal of Computational Physics*, vol. 397, p. 108801, 2019. [Online]. Available: https://www.sciencedirect.com/science/article/pii/S0021999119304851

[38] Bourhrara, "New variational formulations for the neutron transport equation," *Transport Theory and Statistical Physics*, vol. 33, no. 2, pp. 93–124, 2004. [Online]. Available: https://doi.org/10.1081/TT-120037803

[39] P. A. Raviart and J. M. Thomas, "A mixed finite element method for 2-nd order elliptic problems," in *Mathematical Aspects of Finite Element Methods*, I. Galligani and E. Magenes, Eds. Berlin, Heidelberg: Springer Berlin Heidelberg, 1977, pp. 292–315.

[40] J. Nedelec, "Mixed finite elements in IR3 ." *Numerische Mathematik*, vol. 35, pp. 315–342, 1980. [Online]. Available: http://eudml.org/doc/186293

[41] K. Sun, J. Krepel, K. Mikityuk, S. Pelloni, and R. Chawla, "Void reactivity decomposition for the sodium-cooled fast reactor in equilibrium fuel cycle," *Annals of Nuclear Energy*, vol. 38, no. 7, pp. 1645–1657, 2011. [Online]. Available: https://www.sciencedirect.com/science/article/pii/S0306454911000910

[42] P. Sciora, D. Blanchet, L. Buiron, B. Fontaine, M. Vanier, F. Varaine, C. Venard, A.-C. Scholer, and D. Verrier, "Low void effect core design applied on 2400 MWth SFR reactor," *Conference: International Congress on Advances in Nuclear Power Plants (ICAPP'11)*, 05 2011.

[43] C. Bay, "Étude des performances de solveurs déterminisites sur un coeur rapide à caloporteur sodium," Ph.D. dissertation, École Polytechnique de Montréal, 2013, m.A.Sc dissertation, Département de génie physique, available at http://merlin.polymtl.ca/downloads/2013_CharlotteBay.pdf.

[44] T. Takeda and H. Ikeda, "3-D neutron transport benchmarks," *Journal of Nuclear Science and Technology*, vol. 28, no. 7, pp. 656–669, 1991. [Online]. Available: https://doi.org/10.1080/18811248.1991.9731408

[45] M. Chenaud, N. Devictor, G. Mignot, F. Varaine, C. Vénard, L. Martin, M. Phelip, D. Lorenzo, F. Serre, F. Bertrand, N. Alpy, M. L. Flem, P. Gavoille, R. Lavastre, P. Richard, D. Verrier, and D. Schmitt, "Status of the ASTRID core at the end of the pre-conceptual design phase 1," *Nuclear Engineering and Technology*, vol. 45, no. 6, pp. 721–730, 2013. [Online]. Available: https://www.sciencedirect.com/science/article/pii/S1738573315301741

[46] A. A. Calloo, "Parallel Discontinuous Finite Element SN Solver in Cartesian and Hexagonal Geometries for the Boltzmann Transport Equation in DRAGON5," Ph.D. dissertation, École Polytechnique de Montréal, 2022, PhD thesis, Département de génie physique, available at http://merlin.polymtl.ca/downloads/2022_Atyab_Ahmad_Calloo-thesis.pdf.

[47] B. Faure, P. Archier, J.-F. Vidal, J. M. Palau, and L. Buiron, "Neutronic calculation of an axially heterogeneous ASTRID fuel assembly with APOLLO3®: Analysis of biases and foreseen improvements," *Annals of Nuclear Energy*, vol. 115, pp. 88–104, 2018. [Online]. Available: https://www.sciencedirect.com/science/article/pii/S0306454917304863

[48] G. Valocchi, "Modélisation neutronique de coeurs complexes en cinétique multidimensionnelle : application au coeur astrid faible vidange et à la préparation d'expériences

de validation," Ph.D. dissertation, 2020, thèse de doctorat dirigée par Tommasi Jean et Ravetto Piero; Energie, Rayonnement, Plasma Aix-Marseille 2020. [Online]. Available: http://www.theses.fr/2020AIXM0101

APPENDIX A ERANOS NUMBERING AND TRAVERSES PLOTTED

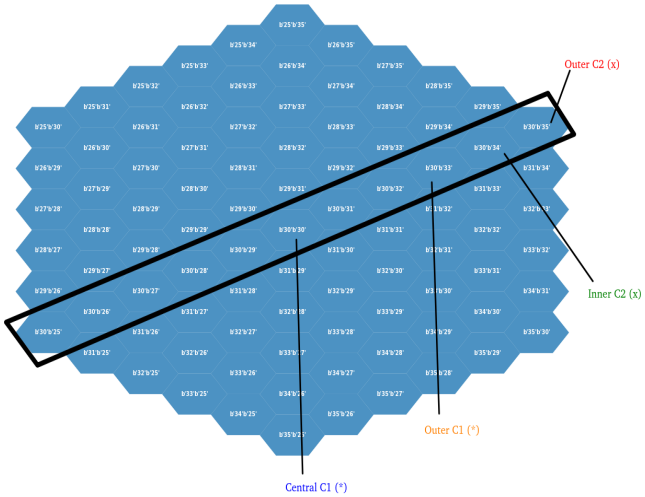

Figure A.1 Representation of the ERANOS numbering used to label the hexagons. The radial traverse is shown in the black rectangle. The assemblies selected for the axial traverses are labeled according to color and marker plotted.

Figure A.1 shows the ERANOS hexagonal numbering as well as the radial traverse used to produce figures showing relative errors at each height along the traverse. Additionally, the labeled fuel assemblies are the ones referred to as "Central C1", "Outer C1", "Inner C2" and "Outer C2" in the text. Axial traverses are performed at these radial positions.

APPENDIX B MPO TO XML INTERFACE

The standard output of AP3 lattice schemes is the MPO file. It is based on the hdf5 file format, and corresponds to a sequence of concatenated dictionaries. Each key represents a node and the tree structure leads to saved data, such as calculated assembly cross sections or energy mesh. On the other hand, the PARIS formalism is based on the XML format. With the SEASON platform being based on the PARIS platform, the development of a python class "MPOtoXML" serving as an interface between both formats was prototyped. Thanks to previous work done by Giorgio Vallochi as part of his Ph.D thesis [48], the interface's development started from his "MPOParser" python class. The class' functions were extended to retrieve the group to group scattering matrices from the MPO format, in a class called "MPOParserv2". The latter are stored in a sparse matrix format in order to avoid the large number of transfer cross sections which are simply 0. This is not the case in the PARIS XML format which stores the full matrices representing scattering cross sections. The "MPOtoXML" class developed allows to treat a list of MPOs to be converted to XML format compatible with the PARIS architecture. All of the necessary 33g cross sections are thus parsed from MPOs in the input list using "MPOParserv2", in turn, these are converted to the required XML format by the "MPOtoXML" class. It was thus possible to use cross sections generated from a AP3 lattice step in full core solvers using the PARIS convention. This conversion of cross section format was implemented in order to test full core solver from the SEASON platform. Due to time constraints, it was decided not to work in the SEASON platform itself, but on standalone version of PARIS and its SNTACH solver were installed with the help of Laurent Buiron. The graphic interface MACCAO was used to re-create the ANTOINID's core model and a "dummy" diffusion calculation was launched from MACCAO. This allowed for the creation of xml files describing the ANTOINID geometry and physical media. The latter were then used in the SNATCH solver which was then able to perform 3D S_N calculations with a 403 hexagonal product angular quadrature. The ANTOINID's description was completed through the use of XML cross section files generated with the MPOtoXML interface. This demonstrates the feasibility of using AP3 generated cross sections in full core simulations performed in the PARIS platform. The XML data format and java architectures being similar between PARIS and SEASON, it is hoped that this work represents a first step towards the possible use of AP3 generated cross sections in the SEASON platform. It must be noted that the current state of the MPOtoXML python interface is not optimized and would definitely necessitate consequent optimization.

SNATCH was tested with cross sections from the SCRAP and MOC2DHet lattice schemes for NOM and VOID configurations, yielding results presented in tables B.1 and B.2.

Config.	K_{eff} SNATCH	error K_{eff} SCRAP-T4 (pcm)	Time (s)	RAM (GiB)	Void effect (pcm)	Error on void effect (pcm)
NOM	1.01673	150	9091	~ 40	-464	285
VOID	1.01196	436	10479	~ 40		

Table B.1 Full core SNATCH results from SCRAP cross sections. K_{eff} for NOM and VOID configurations, void effect on reactivity and associated errors with respect to T4 reference.

Config.	K_{eff} SNATCH	error K_{eff} MOC2DHet-T4 (pcm)	Time (s)	RAM (GiB)	Void effect (pcm)	Error on void effect (pcm)
NOM	1.02042	505	unrecorded	~ 40	-1001	-252
VOID	1.01010	254	unrecorded	~ 40		

Table B.2 Full core SNATCH results from MOC2DHet cross sections. K_{eff} for NOM and VOID configurations, void effect on reactivity and associated errors with respect to T4 reference.

It can be seen that SNATCH results using cross sections from SCRAP have associated biases that are similar to those obtained through the MINARET solver presented in Chapter 4, with a misrepresentation of the voiding effect by $285pcm$. On the other hand, calculations from the MOC2DHet cross sections (table B.2) are not consistent with the MINARET S_N representation. Since both solvers use the same transport operator, this is rather unexpected and would require some investigation. It is possible that the SNATCH solver was not parameterized properly. The biases recorded could also be due to possible errors in the "MPOtoXML" interface. Additional work would be required to investigate these discrepancies